

**ONE DIMENSIONAL PHOTONIC CRYSTALS AND
PLANAR WAVEGUIDES: FABRICATION BY RF
SPUTTERING AND THEIR CHARACTERIZATION**

A Thesis Submitted for the Degree of

DOCTOR OF PHILOSOPHY

Tesi di

DOTTORATO DI RICERCA IN FISICA

By

**VALLIGATLA SREERAMULU
(08PHPH14)**



Supervisors:

Prof. D. Narayana Rao.....University of Hyderabad

Dr. Maurizio Ferrari.....CNR-IFN, Trento

Dr. Alessandro Chiasera.....CNR-IFN, Trento

MARCH 2013

TO
MY FAMILY
AND
SUPERVISORS

DECLARATION

I hereby declare that the matter embodied in this thesis entitled “**One Dimensional Photonic Crystals and Planar Waveguides: Fabrication by RF Sputtering and their Characterization**” is the result of investigations carried out by me under internationally co-tutored PhD programme at school of Physics, University of Hyderabad, Hyderabad, India and at the Department of Physics, University of Trento, Trento, Italy, under the supervision of Prof. D. Narayana Rao (University of Hyderabad), Dr. Maurizio Ferrari (CNR-IFN) and Dr. Alessandro Chiasera (CNR-IFN).

Place: Hyderabad

Date:

(V.Sreeramulu)



CERTIFICATE

This is to certify that the work described in this thesis entitled “*One Dimensional Photonic Crystals and Planar Waveguides: Fabrication by RF Sputtering and their Characterization*” has been carried out by Mr. **Valligatla Sreeramulu** under our collaborative supervision at the University of Hyderabad, Hyderabad, India and at the Institute for Photonics and Nanotechnologies of the National Research Council (IFN - CNR), CSMFO Lab., Trento, Italy, in the frame work of ITPAR Phase II action and this has not been submitted for any degree or diploma at this or any other University.

Place: Hyderabad

Date:

(Prof. D. Narayana Rao)

Place: Trento

Date:

(Dr. Maurizio Ferrari)

Place: Trento

Date:

(Dr. Alessandro Chiasera)

**Dean
School of Physics
University of Hyderabad**

A word of gratitude

During the past five years at the university of Hyderabad and Trento University I had the chance to meet lots of new and interesting people. Through discussions with people in my surroundings I was able to gain new insights and ideas or overcome problems I had encountered in the course of my work. All of them helped me in a certain way. Therefore it is impossible to thank every single one personally. Nevertheless a few people deserve a personal thank you.

This is indeed a privilege and great pleasure to express my gratitude and deep regard to my supervisor Prof. D. Narayana Rao, who given me the opportunity to work in his group. I am grateful to Dr. Maurizio Ferrari who has given me an opportunity to work at CSMFO group. He introduced me to the field of various materials for photonics. I am also indebted to Dr. Alessandro Chiasera for his suggestions to obtain a better understanding of subject and fabrication of materials for photonic applications. It will be always less than whatever I say and however I express myself to honour their invaluable guidance, keen interest, encouragement, deep involvement, and utmost care on a day to day basis throughout my research work.

I take this opportunity to thank Prof. Ashok Chatterjee, Prof. K. P. N. Murthy and Prof. A. P. Pathak for the theoretical course work at the beginning of my research career. I would like to thank Dr. V. Nirmal Kumar, Dr. V. S. Ashoka, Dr. Suneel Singh, Dr. P. Anantha Lakshmi and Prof. S. Dutta Gupta for their valuable suggestions at Doctoral committee meetings. I thank former Deans Prof. Vipin Srivastava and Prof. C. Bansal and present Dean Prof. Surya P. Tewari for providing needful facilities and all the other faculty members of school of Physics for their enlightening suggestions.

I wish to thank my lab seniors, Shivkiran and Manoj for their encouragement. Thanks to my present lab members Dr. Satyavati, Dr. Jyothi, Dr. Deepak, Shekar, Sriram, Kuladeep, Anjaneyulu, Ramya and S. Shekar for creating friendly and pleasant lab atmosphere. Special thanks to Dr. Alee and Bala Murali Krishna for their helpful discussions and various experiments. I would like to thank M.Sc. Project students Robins, Sahoo, Hari and Vikram for having nice time and discussions. I would like to thank technical assistants Deepti and Laxmi Narayana for their cooperation in using micro-Raman and FESEM instruments.

I am thankful to CSMFO group members Dr. Chiappini, Dr Alombert, Dr. D. Ristic, E. Moser, C. Armelli, S. Varas and A. Carpentiro for their help at various situations. I thank Maurizio Mazzola for CO₂ irradiation experiment and Lorenzo Lunelli (FBK) for AFM measurements and also thankful to Nicola Bazzanella for SEM measurements at Trento.

My time at Trento was made memorable in large part due to the many friends I have made along the way and that became a part of my life. I like to thank all my friends with whom I had a nice time. My thanks to Dr. Nainesh, Dr. Rupali, Dr. Archana, Dr. Ahmed, Dr. Vajir, Lakshun, Raj Kumar and Abdul for their love and taking care about me. I thank to Indian volleyball team for having lot of fun during the holiday and all other friends at Trento who made my life enjoyable and comfortable.

Many thanks to my friends G. Chinna Rao (UK), V. Praveen Kumar, M. M. Rao (IITK), P. Anusha, and B. Uday Kumar for their helpful subject discussions. I would like thank my batch mates (08) Monisha, Saikiran, Shankar, I.V, Aalu, Soorat, Ahmed, Sanjeev and R.V for wonderful time in the campus. At this juncture, I should extend my sincere thanks and deep appreciation to my friends Ramesh Babu, Anjaneyulu, Tirupathi, Pavan, Yougandhar, Bheem Lingam, Satya, Suman, S. Chari, Gangi Reddy, V. V. G. Krishan, Geo, Vijay, Raju for their constant encouragement and support throughout the duration of this period. I thank my friend Chaitanya and his father Venugopal for their incredible help at the time of admission.

Special thanks to my friends during Badminton where I used to forget surroundings.

I express my deep gratitude to my seniors, well wishers and friends.

I thank Abraham and other nonteaching staff for their help and support.

Financial support provided by University of Hyderabad, ITPAR project and CSIR is gratefully acknowledged.

Last but the MOST, I would like to express my deep sense of gratitude to my parents and siblings, for their unconditional love and encouragement throughout.

I express my deepest gratitude to the Almighty for being with me all the time.

Finally I thank all those who have, directly or indirectly, helped me all along.

Sreeramulu

Table of Contents

Declaration	ii
Certificate	iii
A word of gratitude	iv
List of abbreviations	x
Chapter 1: Motivation and Introduction	1-30
1.1. Motivation	3
1.2. Photonic bandgap (PBG) materials	5
1.3. Applications of photonic crystals	8
1.4. PBG Theory	10
1.5. One dimensional photonic crystals	11
1.5.1. Band diagrams	12
1.5.2. Study of the DBR parameters	13
1.5.2.1. Refractive index ratio n_H/n_L	16
1.5.2.2. Number of periods	16
1.5.3. Microcavity	17
1.5.4. Study of the Microcavity parameters	19
1.5.4.1. Thickness of the defect layer	19
1.5.4.2. Refractive index of the defect layer	19
1.5.4.3. Number of periods of the DBR	19
1.6. Choice of materials	20
1.7. Planar waveguides	21
1.8. Fabrication processes	22
1.8.1. RF Sputtering technique	23
1.9. Organization of the thesis	23
1.10. References	25
Chapter 2: Experimental techniques and details	31-46
2.1. Introduction	33
2.2. Optical and spectroscopic techniques	33
2.2.1. Absorption spectrophotometer	33
2.2.2. M-Line spectroscopy	36
2.2.2.1. Refractive index and thickness measurement	36
2.2.2.2. Loss measurement	38
2.2.3. Room temperature photoluminescence measurement	39
2.2.4. Micro-Raman spectrometer	41

2.3.	Nonlinear optical properties measurement	43
2.3.1.	Z-scan technique	43
2.3.2.	Open-aperture Z-scan for absorptive nonlinearity	44
2.3.3.	Closed-aperture Z-scan for sign and refractive scan for absorptive	44
2.4.	Surface morphology and compositional analysis	45
2.4.1.	Field emission-scanning electron microscopy (FESEM)	45
2.4.2.	Atomic Force Microscopy	45
2.5.	References	46

Chapter 3: Fabrication by rf sputtering and optical characterization of one dimensional photonic crystals 47-80

3.1.	Introduction	49
3.2.	Fabrication of one dimensional photonic crystals	50
3.2.1.	Sol – gel technique	50
3.2.2.	Electron beam evaporation	51
3.2.3.	Radio Frequency Magnetron Sputtering Technique (RFMS)	52
3.3.	Dispersion relations	56
3.4.	Optical properties	57
3.4.1.	Transmission and reflection measurements	58
3.4.2.	Effect of number of layers on stop band	62
3.4.3.	Variable angle reflection measurements	64
3.4.4.	Thickness measurement	67
3.4.5.	Transfer Matrix Method (TMM) for 1D photonic crystals	69
3.4.5.1.	Reflectance and Transmittance of the periodic structures	72
3.4.6.	Polarization dependence of spectral characteristics	74
3.5.	Conclusions	78
3.6.	Reference	78

Chapter 4: High Quality factor Er³⁺- activated dielectric Microcavity 81-106

4.1.	Introduction	83
4.2.	Experimental	85

4.3. Results and Discussions	89
4.3.1. Structural and Optical properties of first Bragg Mirror	89
4.3.2. Structural and Optical properties of microcavity	93
4.3.3. Spectroscopic properties of microcavity	98
4.4. Conclusions	101
4.5. References	102

Chapter 5: Enhanced nonlinear optical response in one dimensional photonic crystal with ZnO defect layer 107-138

5.1. Introduction	109
5.1.1. Nonlinear Optics	111
5.1.1.1. Nonlinear absorption	112
5.1.1.2. Multiphoton absorption	112
5.1.1.3. Nonlinear refraction	116
5.2. Experimental	117
5.3. Results and discussions	118
5.3.1. Refractive index profile	118
5.3.2. Structural and optical properties of first Bragg Mirror	119
5.3.3. Structural and optical properties of microcavity	121
5.3.4. Variable angle reflectance characteristics of microcavity	124
5.3.5. Optical absorption of ZnO	126
5.3.6. Nonlinear optical properties	127
5.3.6.1. Nonlinear absorption and refraction	128
5.3.6.2. Optical limiting	132
5.4. Conclusions	135
5.5. References	135

Chapter 6: CO₂ laser and positron irradiation effect on pure GeO₂ planar waveguides 139-162

6.1. Introduction	141
6.2. Experimental	143
6.2.1. Planar waveguide fabrication	143
6.2.2. CO ₂ Laser irradiation	143
6.2.3. Optical and structural properties	144
6.2.4. Positron irradiation	145

6.3. Results and discussions	145
6.3.1. Optical properties	145
6.3.2. Structural properties	146
6.3.2.1. EDS and Raman analysis	146
6.3.2.2. AFM analysis	148
6.3.3. Effect of positron irradiation	151
6.4. Conclusions	157
6.5. References	158
Chapter 7: Conclusions and future perspectives	163-170
7.1. Conclusions	164
7.2. Future perspectives	167
7.3. References	168
Curriculum vitae	169-172

List of abbreviations

AFM	: Atomic Force Microscopy
BR	: Bragg Mirror
DBR	: Distributed Bragg Mirror
DBS	: Doppler Broadening Spectroscopy
EM	: Electromagnetic
fcc	: Face centred cubic
GeO ₂	: Germania
FESEM	: Field Emission scanning Electron Microscope
FWHM	: Full width half maximum
LED	: Light Emitting Device
NIR	: Near Infrared Region
NLO	: Nonlinear Optical
OL	: Optical Limiting
PAS	: Positron Annihilation Spectroscopy
PBG	: Photonic Band Gap
PC	: Photonic Crystal
PCF	: Photonic Crystal Fibre
PL	: Photoluminescence
RIC	: Refractive Index Contrast
RI	: Refractive Index
RFMS	: Radio Frequency Magnetron Sputtering
SEM	: Scanning Electron Microscope
SiO ₂	: Silica
TiO ₂	: Titania
TPA	: Two photon absorption
TMM	: Transfer Matrix Method

The activities presented in this thesis are performed in the frame work of DST sponsored Joint Research Program 2008 – 2011, India – Trento Program for Advanced Research “ Fabrication and Characterization of novel photonic structures (polystyrene and polystyrene - silica) and Si/Ge quantum dots for photonics applications” at School of Physics, University of Hyderabad and the C.S.M.F.O (Caratterizzazione e Sviluppo Materiali per la Fotonica e l’Optoelettronica) group (CNR – IFN and Physics Department, University of Trento).

Chapter 1

Motivation and Introduction

Abstract:

This chapter describes the motivation of the thesis and basic concepts about the photonic crystal. Mainly focussed on one dimensional photonic crystals and the related band diagrams, various parameters that effect on stop band are briefly explained.

1.1 Motivation

The twentieth century has witnessed most of the revolutionary discoveries among them, one is electronic devices in the history of mankind. They have given a new dimension to the scientific world that has been racing to build electrical components that are smaller in size and that can transfer more information with high speed. In order to do this, higher frequencies must be used, which means abandoning traditional electronic circuits. We are just starting to realize the immense capabilities that can be harnessed at these higher frequencies, especially in the optical range. As optical fibers are not capable of guiding light around small radius turns, which strongly limits their capabilities in some areas and the optical computer is not even close to being developed. In order to make the advancements that are necessary in this field, an understanding of how one would control and manipulate these optical frequencies must be sought and Photonic band gap materials (PBG) are expected to play an important role in this direction.

Photonic crystals are periodically structured electromagnetic media, generally possessing photonic band gaps, which are ranges of frequency for which light cannot propagate through the structure [1]. Photonic crystals offer unique ways to tailor light and the propagation of electromagnetic waves. Analogy to electrons in atomic crystals, electromagnetic waves propagating in a structure with a periodically modulated dielectric constant are organised into allowed photonic bands which are separated by gaps in the frequency spectrum where propagation is forbidden. For example, in an emission material, spontaneous emission is suppressed for photons of frequency lying in the photonic band gap, offering novel approaches for manipulating the electromagnetic field and creating high efficiency light-emitting structures [2 - 4].

Erbium-doped materials are of great interest in optoelectronics due to the Er^{3+} emission at 1.535 μm , a standard telecommunications wavelength. One

technique for increasing the luminescence yield of erbium is to produce resonating structures such as Fabry–Perot microcavities that incorporates an active layer. The main goal is to develop appropriate material systems and devices to exploit at the best the luminescence properties of erbium. Er^{3+} - activated confined structures at different scales thus offer interesting solutions. It has seen a remarkable increase in the experimental efforts to control and enhance emission properties of emitters by tailoring the dielectric surrounding of the source. Strong confinement produced by high-Q cavities can modify both the spectral line width and luminescence life time of the erbium emission as well as enhance emission intensity and directivity [5]. These structures are of tremendous interest and are being widely studied for their applications in integrated optics.

Combining photonic crystals and nonlinear optics, leads to enhancement in the nonlinear optical response and thus towards the new applications in nonlinear optical devices. This can be achieved when a defect layer includes nonlinear optical materials, it is expected that strong enhancement of optical nonlinearity by several orders of magnitude can be obtained in the defect layer. The nonlinear optical effects are usually limited to the high optical intensity regime due to the weak nonlinear optical response of most naturally occurring materials. The possibility of PBG materials with optical tunability afforded by the intensity-dependent properties of nonlinear materials, would offer unprecedented control over the flow of light, and therefore is of great interest for PBG device applications.

Planar waveguides are key platform on which to construct integrated optical (IO) circuits, with multiple functions such as optical switches, amplifiers, interferometers, detectors etc. Along with SiO_2 , other glass material which is suitable for IO is GeO_2 . In particular GeO_2 based glasses are interesting due to lower T_g (glass transition temperature) and phonon energy than SiO_2 . Germania allows fabrication of highly photorefractive planar waveguides [6] and drawing fiber with smaller absorption losses in the middle IR range as compared to silica glass [7]. For these reasons it is of technological and scientific importance to

develop a particular fabrication protocol to obtain optical waveguides based on GeO₂ system that exhibits low attenuation coefficients and simultaneously embed GeO₂ nanocrystals with a particular phase. In order to produce active rare earth nanocrystals in a glass matrix, heat treatment using a furnace has been commonly used, but a potential candidate for reaching future technology nodes is the laser annealing (LA) process. LA allows one to modify the structural features of the films and consequently the optical and spectroscopic properties such as luminescence and optical losses in the planar waveguides.

1.2 Photonic bandgap (PBG) materials

Photonic crystals are periodically arranged dielectric structures which can control the flow of photons like semiconductor crystals [1]. PBG materials, also called photonic crystals (PCs) have allowed and forbidden frequency bands. Electromagnetic (EM) waves of frequencies within the allowed bands can propagate through the PCs, but propagation of EM waves with frequencies within the forbidden band cannot occur. Depending on the periodicity arrangement, PCs may be broadly classified as one-dimensional (1D), two-dimensional (2D) and three-dimensional (3D) which are shown in Figure 1.1. 1D PBG structures usually consist of a stack of layers with alternating high and low refractive indices. 2D PBGs can either be planar structures, with a periodic pattern in two directions, or PBG fibers (often called PC fibers [8]), such as the hollow core, or ‘holey’ fibers, or the depressed index solid core PBG fibers, where there is a PBG in the cladding. 3D PBGs have a refractive index which is periodic in three dimensions and are generally of the opal, or inverse opal type. If a structural defect is introduced in the PC, the defect states will appear in the PBG [9].

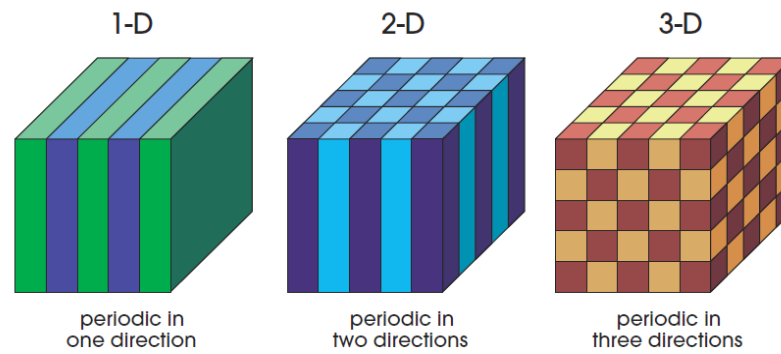


Figure 1.1: Simple examples of one-, two- and three-dimensional photonic crystals. The different colors represent materials with different dielectric constants. The defining feature of a photonic crystal is the periodicity of dielectric material along one or more axes.

In 1887, Lord Rayleigh was the first who studied the propagation of electromagnetic waves in connection with the peculiar reflective properties of a crystalline mineral with periodic “twinning” planes [10]. These correspond to one-dimensional photonic crystals and identified the fact that they have a narrow band gap prohibiting light propagation through the planes. This band gap is angle-dependent, due to the differing periodicities experienced by light propagating at non-normal incidences, producing a reflected color that varies sharply with incident angle. A similar effect is responsible for many other iridescent colors in nature, such as butterfly wings, the sea mouse and precious opals.

During 1970's, EM wave propagation in 1D periodic structures have been thoroughly explored by Yeh, Yariv and Hong [11]. Later, the study of spontaneous emission suppression in periodic structures by V. P. Bykov [12] in 1972 and extension of this work through complete photonic band gap structures by E. Yablonovitch [13] who tried to suppress the spontaneous emission in lasers, by embedding active medium in 3D periodic medium and S. John [14], the research objective was localization of light; which led to increasing interest in photonic crystals (PC). They first proposed the idea of photonic band structure:

the idea is that an extended medium with a periodically modulated permittivity would exhibit structure in the photon energy-momentum dispersion relation, analogous to the energy gaps observed in electronic dispersion in crystalline solids owing to the periodically modulated atomic potential and predicted the existence of full band gap for the first time, and thus marked the birth of “3D photonic crystals”. After the pioneering work of Yablonovitch and John, since many researchers have tried to realize PBGs both experimentally and theoretically, with different type of structures such as fcc [15 - 17], diamond [17], yablonovite [18, 19], woodpile [20], in the optical frequency regions [21].

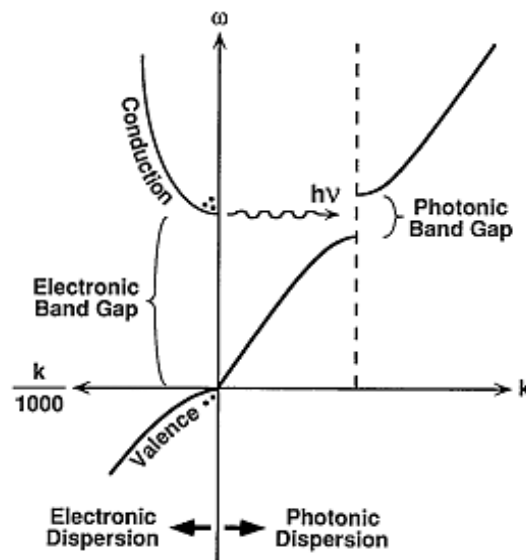


Figure1.2: Schematic illustration of inhibited electron-hole recombination by PBG crystal. The left side depicts a band gap in the electronic dispersion, while the right depicts the photonic dispersion relation for a PBG crystal designed to suppress spontaneous emission from electron-hole recombination [22].

PCs have the dielectric periodicity, whose length scale is proportional to the wavelength of light in the band gap, is the electromagnetic analogue of a crystalline atomic lattice. The term “photonic band gap” is analogous to a semiconductor band gap (between the valence and conduction bands); in which electrons of certain energies may not propagate in any direction as shown in

Figure 1.2 [22]. The periodicity of the potential of an atomic lattice prevents electrons having energies falling within a certain band from propagating [23]. In the same way, periodic structures composed of materials with different dielectric constants prevent electromagnetic waves of a certain band of frequencies from propagating; caused by destructive interference of the scattered waves from the interfaces which results in complete or almost complete reflection for photons of few range of frequencies.

As illustrated in Figure 1.2, if a photonic band gap is to occupy the electronic band edge, then the photon produced by electron-hole recombination would have no place to go. The spontaneous radiative recombination of electrons and holes would be inhibited. As can be imagined, this has far-reaching implications for semiconductor photonic devices.

1.3 Applications of photonic crystals

Two of the most prominent applications of the photonic band gap are the localization of light at defects, and the inhibition of radiation. Yablonovitch [13] describes how the photonic band gap can control spontaneous emission by examining Fermi's golden rule. The density of the final states in spontaneous emission is the density of modes available to the photon emitted. If the photonic bandgap does not provide a mode to the photon, there will be no spontaneous emission [13].

The designed defect in photonic crystals is a very important issue. Most applications of photonic crystals are based on how to introduce the defects in the photonic crystals engineering, one can control, trap, or change the wave propagation. Basic photonic crystals defects are of two types, point defect and line defect. The material property variation at one point or several points in the periodic structures forms the point defect. For example, in 1D photonic crystals, the usual methods to create defects include changing the size of the layers. The point defect sometimes behaves like a cavity that has a very high Q factor which results in narrow emission from PC that act as a microcavity laser. The line

defects are sometimes treated as photonic crystal waveguide. The wave modes within the photonic bandgap are confined in the photonic crystal waveguide. The bends made by photonic crystal waveguide have proved to be valuable. If the bends and photonic crystals are designed properly, certain frequency components can propagate with very low loss, even it has 90 degree bend [24].

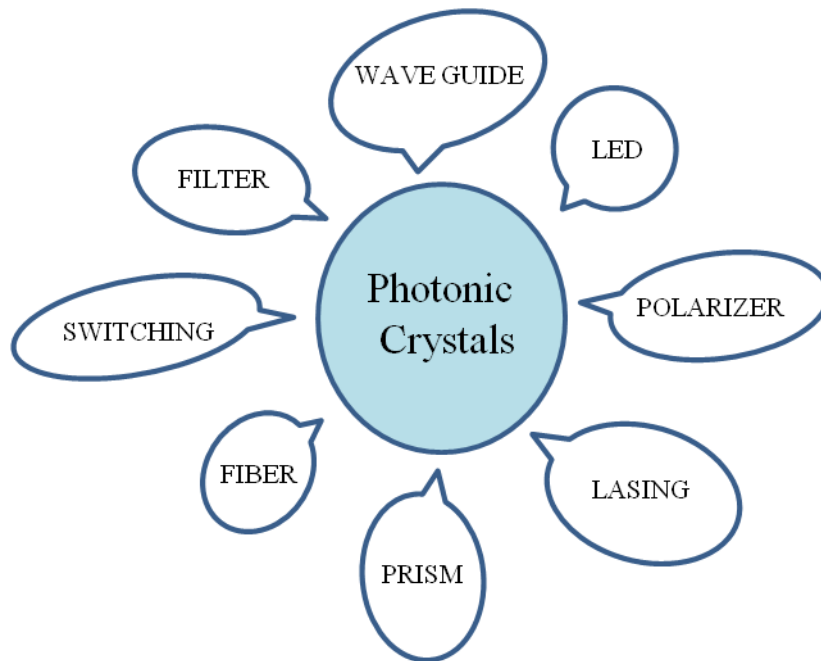


Figure 1.3: Applications of the photonic crystals

One of the main advantages of the photonic crystal technology is the possibility of the full integration of optical devices on all optical chips that can operate at much higher frequency and consume less power than today's electronic silicon chips. The application of these chips together with optical interconnections makes it possible to create novel optical systems such as, for example, optical computers with extremely high speed of digital data processing [25]. Other applications of photonic band gaps include the construction of perfect dielectric mirrors, resonant cavities (lasers), and waveguides that are capable of guiding light through very sharp turns [1].

1.4 PBG Theory

Understanding the relationship between electronic band structure and photonic band structure requires an examination of the basic equation governing the motion of electron and photons: the Schrödinger equation [26, 27] and Maxwell's Equation [28]. When applied to the problems of electrons in crystalline solids and photons in periodic dielectric media, respectively, analogies between the two governing relations become apparent. To make the most of these analogies, it is important to look at both the similarities and the differences. The following discussion has been adapted from reference [29].

The behavior of the electron wave function $\psi(\mathbf{r})$ is described by the Schrödinger equation,

$$\left(-\frac{\hbar^2}{2m_e} \nabla^2 + V(\mathbf{r}) \right) \Psi_E(\mathbf{r}) = E \Psi_E(\mathbf{r}) \quad (1.2)$$

$$\text{This implies to } \hat{H} \Psi_E(\mathbf{r}) = E \Psi_E(\mathbf{r})$$

While Maxwell's curl equation can be combined (in the absence of sources) to yield the following equation for the magnetic field $H(\mathbf{r})$:

$$\left(\nabla \times \frac{1}{\varepsilon(\mathbf{r})} \nabla \times \right) H_\omega(\mathbf{r}) = \frac{\omega^2}{c^2} H_\omega(\mathbf{r}) \quad (1.3)$$

$$\text{This implies to } \hat{\theta} H_\omega(\mathbf{r}) = \frac{\omega^2}{c^2} H_\omega(\mathbf{r})$$

In the case of crystalline solids, the atomic potential is periodic, i.e.

$$V(\mathbf{r} + \mathbf{R}) = V(\mathbf{r}) \quad (1.4)$$

where \mathbf{R} is a vector representing the displacement between any pair of lattice sites. Solutions of both eigen value problems take the form of Bloch waves,

consisting of a wave ($\sim e^{ik \cdot r}$) multiplied by a periodic amplitude $u(\mathbf{r})$ sharing the same periodicity of the lattice,

$$u(\mathbf{r} + \mathbf{R}) = u(\mathbf{r}) \tag{1.5}$$

It should be noted that the choices of formulating the photonic eigen value problem in terms of the magnetic field $H(\mathbf{r})$ instead of electric field $E(\mathbf{r})$ is not made arbitrarily. The Maxwell operator as defined above is Hermitian, guaranteeing that eigen modes are orthogonal and eigen values are real and facilitating techniques for finding solutions in numerous ways. If we eliminate H rather than E between the two Maxwell curl equations, the resulting modified Maxwell operator is not Hermitian. The formal similarities allow us apply to photonic crystals many of the concepts of solid state physics [30]; forbidden energy gaps, the reciprocal space, Brillouin zones, conduction and valance bands, donor and acceptor impurity states, and localization.

1.5 One dimensional photonic crystals

A one dimensional (1D) photonic crystal is a periodically layered structure made up of materials with different dielectric constant. The simplest and most common type of 1D photonic crystal composed of quarter wave stacks of two dielectrics with different refractive indices which is called Bragg mirror (BM) or distributed Bragg reflector (DBR). BM consists of a stack of alternating high and low refractive index dielectric layers and exhibits a frequency region of high reflectivity. The optical thickness of each layer of the BM is $nd = \lambda / 4$, where n and d are the refractive index and thickness of a layer respectively, and λ is the wavelength of maximum reflectivity. This forbidden frequency range is also called a ‘stop band’. Moreover, when the BM structure has a defect, such as a missing layer, this will cause the occurrence of an allowed state (‘pass band’) localized inside the stop band at the resonance wavelength, λ .

1.5.1 Band diagrams

The schematic of a quarter wave stack which consists of alternating layers of different dielectric materials is shown in Figure 1.5. In a quarter wave stack the gap to midgap frequency ratio is related to the refractive indices of its constituent materials as given below [31].

$$\frac{\Delta\omega}{\omega_m} = \frac{4}{\pi} \sin^{-1} \left(\frac{|n_1 - n_2|}{n_1 + n_2} \right) = \frac{4}{\pi} \sin^{-1} \left(\frac{\left| \frac{n_1 - 1}{n_2} \right|}{\frac{n_1}{n_2} + 1} \right) \quad (1.6)$$

Here $\Delta\omega$ and ω_m are width and central frequency of band gap; n_1 and n_2 are the refractive indices of alternating layers with period ‘ a ’. Figures 1.4 (b) - (d) represents the dispersion relations of multilayer films with different RICs (RIC = $n_1:n_2$). These band diagrams were calculated using RSoft’s BandSOLVE commercial software, which implements the plane wave expansion method [32].

In all cases, each layer has the same width of $a/2$. The frequency is expressed in dimensionless units of $\omega a / 2\pi c = a / \lambda$; where λ and c are wavelength and velocity (in free space) of light. In the case of RIC = 3.6:3.5 (Figure 1.4 (b)), a very narrow band gap (shaded region) is opened between the first two bands ($n = 1, 2$) and further increased RIC between the alternating layers has resulted in a wider band gap (figure 1c and 1d) which confirms the band gap width is proportional to RIC.

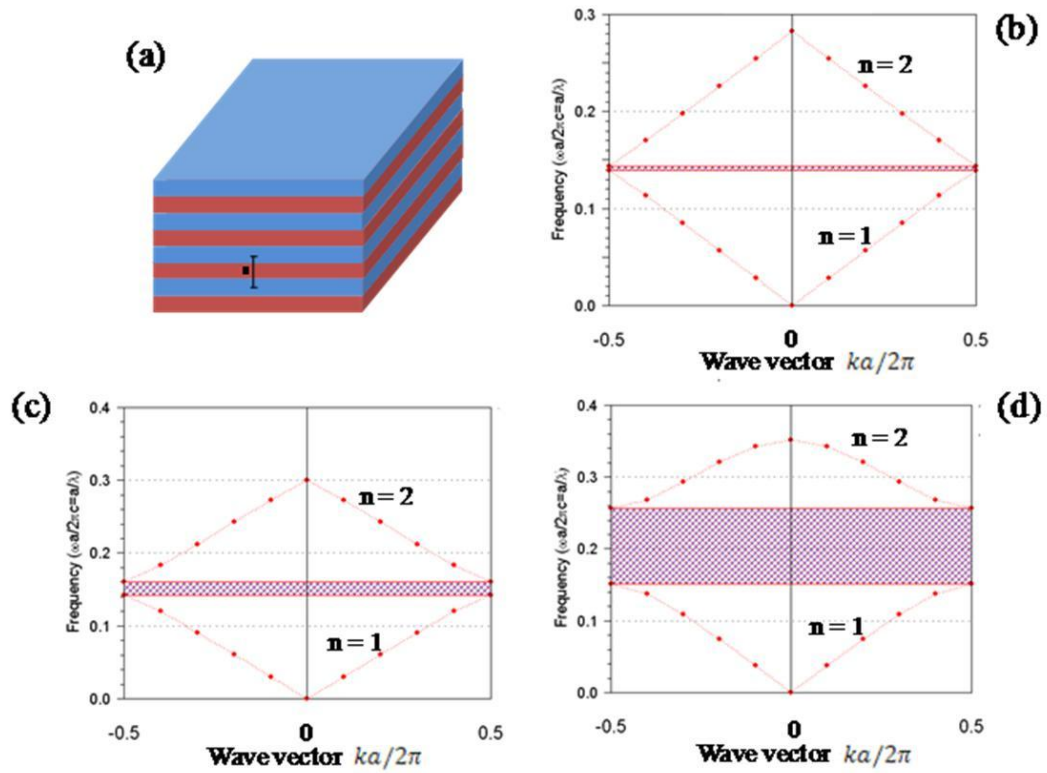


Figure 1.4: a) A multilayer film of 1D PC containing alternating layers with refractive index n_1 and n_2 with period ' a '. The dispersion relations are calculated for different multilayer films with refractive index contrast (RIC) of b) 3.6:3.5, c) 3.6:3 and d) 3.6:1. The ordinate is plotted in dimensionless units: $\omega a / 2\pi c = a / \lambda$; λ and c are wavelength and velocity (in free space) of light. In all the cases each layer has a width of $a / 2$. Shaded region indicate the photonic bandgap.

1.5.2 Study of the DBR parameters

The principle of operation can be understood that each interface between the two materials contributes a Fresnel reflection. For the design wavelength, the optical path length difference between reflections from subsequent interfaces is half the wavelength; in addition, the amplitude reflection coefficients for the interfaces have alternating signs. Therefore all the reflected components from the

interfaces interfere constructively, which results in a strong reflection. The reflectivity achieved is determined by the number of layer pairs and by the refractive index contrast between the layer materials. The reflection bandwidth is determined mainly by the index contrast. The schematic diagram of DBR is shown in Figure 1.5.

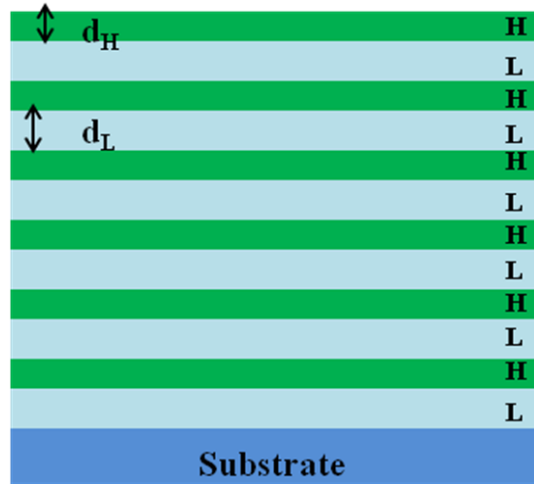


Figure 1.5: Schematic diagram of Bragg mirror.

The reflectivity of the DBR can be calculated using the theoretical formula,

$$R = \left[\frac{1 - \frac{n_s}{n_0} \left[\frac{n_H}{n_L} \right]^{2p}}{1 + \frac{n_s}{n_0} \left[\frac{n_H}{n_L} \right]^{2p}} \right]^2 \quad (1.7)$$

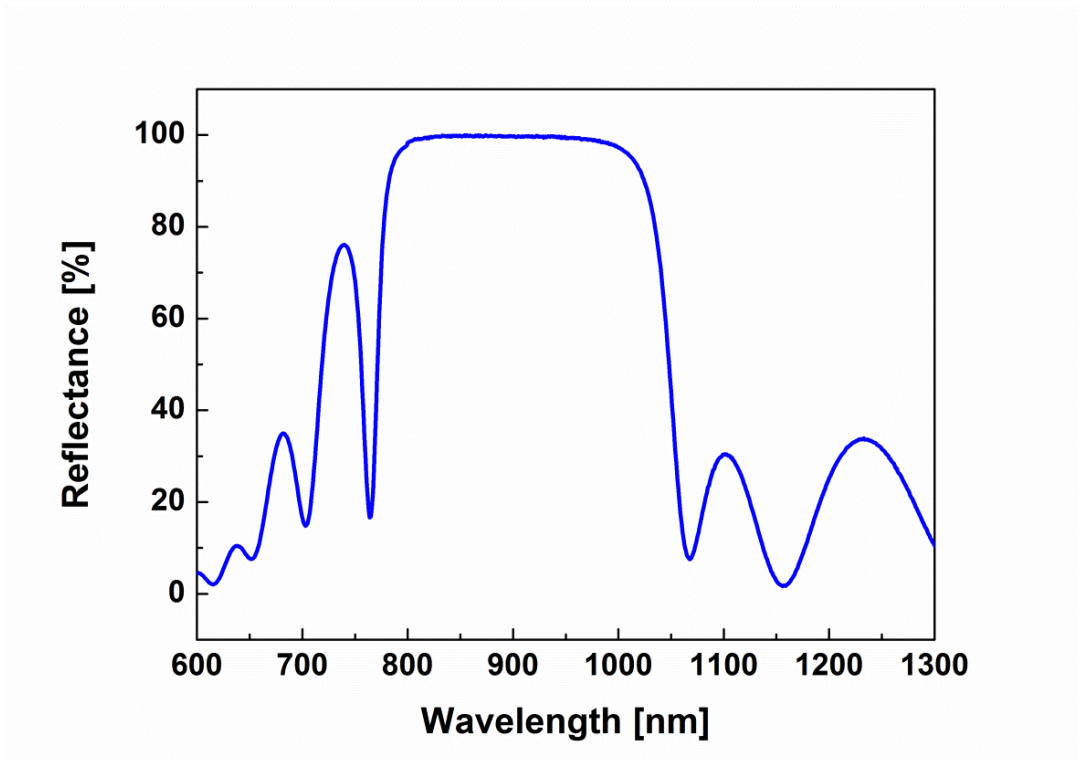


Figure 1.6: experimentally calculated reflectivity spectrum of DBR containing 9 pairs of SiO_2 and TiO_2 layers.

Where n_H is the high refractive index layer, n_L is the low refractive index layer, n_s is the refractive index of the substrate, n_0 is refractive index of the environment, p is the number of $\lambda/4$ layer pairs. The reflectivity spectra shown in the Figure 1.6, is obtained experimentally for DBR containing 9 pairs of SiO_2 and TiO_2 layers in NIR region. From the Figure 1.6, it is observed that 99.80 % is the maximum reflectivity obtained from the DBR. Using the equation 1.7, we have obtained 99.92 % reflectivity, which is a good agreement between theoretical and experimental results.

There are few parameters like number of periods in DBR, thickness of the each layer and refractive index contrast will effect on the parameters reflectivity and full width half maximum (FWHM).

1.5.2.1 Refractive index ratio n_H/n_L

The ratio n_L/n_H is called the refractive index contrast that influences on the width (FWHM) and the sharpness of the DBR bandgap. The increase of the refractive index contrast leads to the widening of the bandgap [33]. This effect can be observed from the Figure 1.7 which is a simulated result, where the reflectivity spectra of three $\lambda/4$ DBRs with different n_H/n_L ratio show a bandgap with different width. We can also observe that the band edges become sharper when the ratio increases.

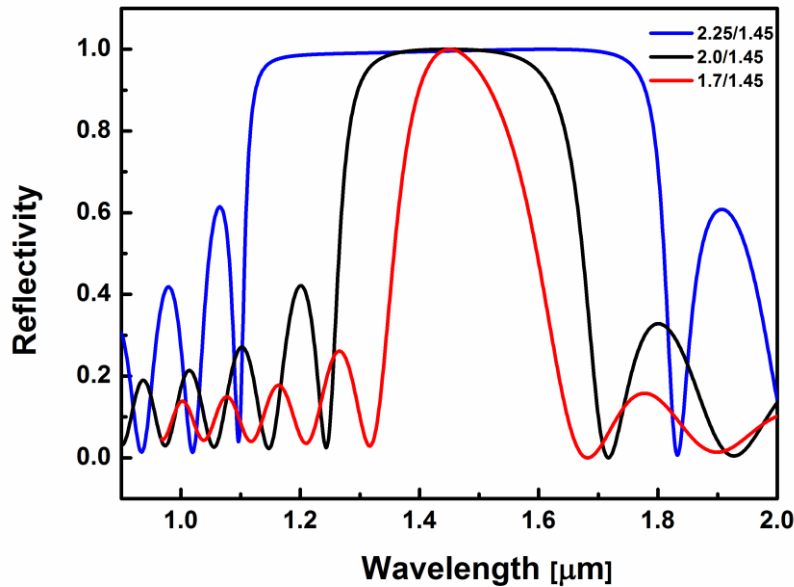


Figure 1.7: Reflectivity spectrum for three different multilayers with three different refractive indices at normal incidence.

1.5.2.2 Number of periods

The number of periods (N) influences on different characteristics of the bandgap. The increase in the number of periods N leads to an increase of the reflectivity within the bandgap, and enlarges its width. The band edges also become sharper. From the Figure 1.8, this effect can be observed and this result is

obtained from the simulations. It shows three $\lambda/4$ DBR with $n_H=2.3$, $n_L=1.46$ for different number of periods N . We can observe that when N increases, the band edges of the filter become sharper and the reflectivity tends to the unity exponentially with N [34].

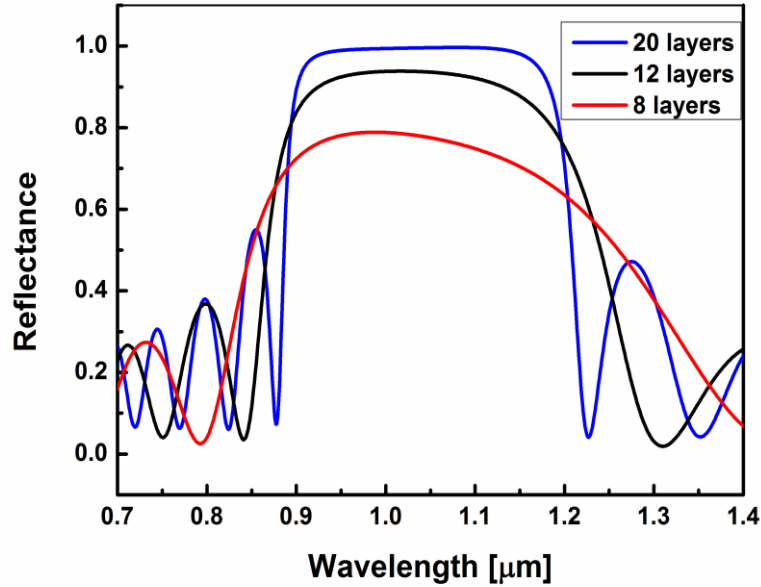


Figure 1.8: Reflection spectrum of a $\lambda/4$ -DBR with $n_H=2.3$, $n_L=1.46$ and number of periods 8, 12 and 20.

1.5.3 Microcavity

It is possible to fabricate a particular class of interferometers, named microcavities, by using two parallel reflectors separated by a spacer layer. Usually the reflectors used are $\lambda/4$ DBR. The reflectivity spectrum of microcavities consists of a wide high reflectivity bandgap with a narrow pass-band in its centre. The wavelength at which this pass band (also called transmission peak) is situated, its width and its reflectivity level depend on different parameters. The schematic diagram of the microcavity is shown in Figure 1.9.

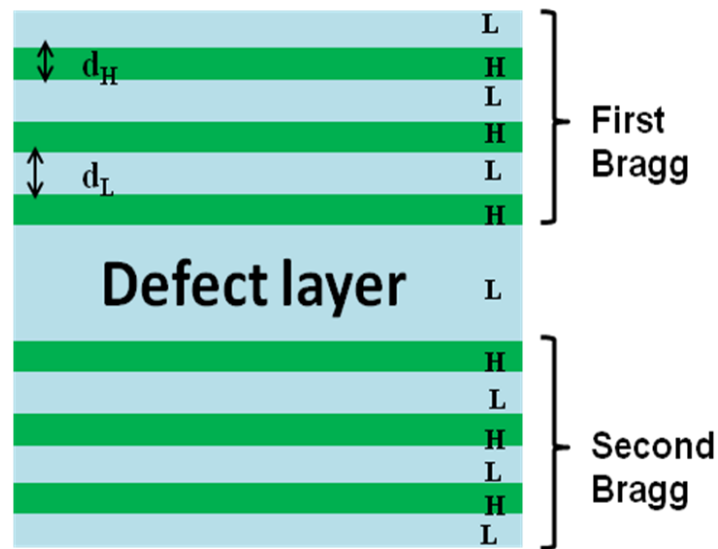


Figure 1.9: Schematic diagram of Microcavity

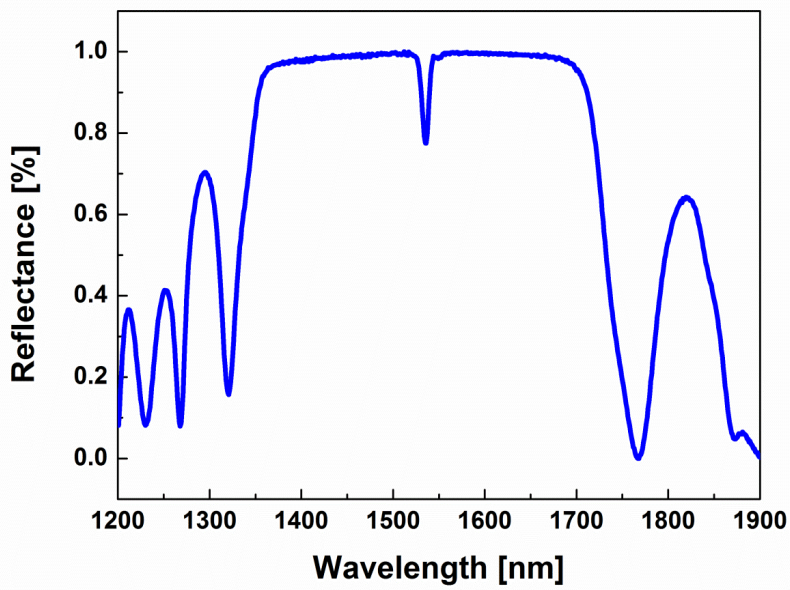


Figure 1.9: The reflection spectra of microcavity with Er^{3+} doped active layer in NIR region. The spectra obtained at 50° incident angle.

1.5.4 Study of the Microcavity parameters

The microcavity consists of two $\lambda/4$ DBR with N periods where $n_H = 2.3$ and $n_L = 1.46$. The optical thickness of the layers are $\lambda/4 = n_H d_H = n_L d_L$ with $\lambda = 1534$ nm. The defect layer thickness is $\lambda/2$ and is SiO₂ doped with Er³⁺, its refractive index is $n_d = 1.46$. Figure 1.9 shows the experimentally obtained reflectivity spectrum for the microcavity in near infrared (NIR) region.

1.5.4.1 Thickness of the defect layer

The optical thicknesses of the DBRs are usually $\lambda/4$, the optical thickness of the defect layer can be either λ or $\lambda/2$. In both cases, the transmission peak is centered at wavelength λ . Also the transmission peak will be centered in the bandgap and the reflectivity is almost zero at particular wavelength. However, the bandgap of the microcavity with the $\lambda/2$ spacer is slightly wider than the one with thickness λ and the side lobes closer to the bandgap show a lower reflectivity.

1.5.4.2 Refractive index of the defect layer

The refractive index of the defect layer can be one of the indices used in the DBRs (n_H, n_L) of the microcavity or a different value.

1.5.4.3 Number of periods of the DBR

The width of the transmission peak depends on the number of periods N of the DBRs of the microcavity. When N increases, the transmission peak becomes narrower, the reflectivity of the bandgap increases and its edges are sharper.

1.6 Choice of the materials

The materials which are prepared with metals do not scale well into optical frequencies. At high frequencies metals become more and more lossy. These dissipative losses allow for virtual modes, even at frequencies that would normally be forbidden. Therefore it makes sense to consider structures made of positive dielectric constant materials, such as glasses and insulators, rather than metals. These materials can have low dissipation, even all the way up to optical frequencies. This property is ultimately exemplified by optical fibers, which permit light propagation over many kilometres with negligible losses. Such positive-dielectric-constant materials can have an almost purely real dielectric response with low resistive losses. If these materials are arrayed into a three-dimensionally periodic dielectric structure, a photonic band gap should be possible, employing a purely real, reactive, dielectric response.

Oxide-based dielectric materials are particularly suitable for fabricating PBG structures because they have wide transparency from the ultraviolet to the near infrared (NIR). Furthermore, oxide-based dielectric materials have good resistance to temperature, corrosion and radiation as well [35 - 37]. There are different materials available which can be suitable for the fabrication of multilayer structures. We have chosen SiO_2 , TiO_2 dielectric materials for the fabrication.

Table 1.1: Materials available and their refractive index at 633nm

Name of the Material	Refractive index
SiO ₂	1.456
TiO ₂	2.24
SnO ₂	1.923
HfO ₂	1.913
InGaAs	3.855
Ta ₂ O ₅	1.796
PMMA	1.489
MgF ₂	1.377
ZnS	2.55

1.7 Planar waveguides

An optical waveguide is a device which can confine light energy and transport from one region of space to another with low power loss. Usually total internal reflection (TIR) phenomenon is utilized to design such an agreement. Optical waveguides are structures with three layers controlling light confinement and propagation in a well defined direction inside the central layer (Figure 1.10).

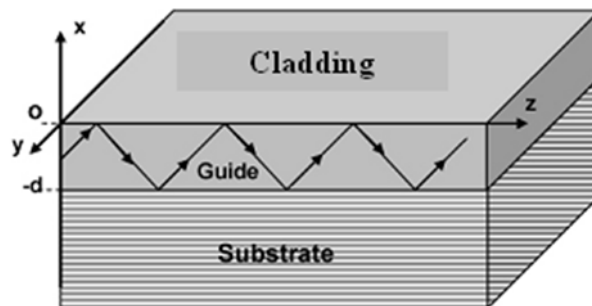


Figure 1.10: Planar optical waveguide

Light confinement is carried out by successive total reflections on the two interface guides - substrate and guide - cladding. Light propagation is

governed by an interference phenomenon which occurs inside the guide between two waves; one of them undergoes two successive total reflections. For a better understanding of the guided wave propagation, we will recall the main principles of these two phenomena, total reflection and interference, inside a transparent plate with parallel faces [38].

The integration of optical waveguides into very high-speed circuit boards holds great promise and is the subject of many development efforts. Where copper reaches its limits at high frequency transmissions due to the signal attenuation, cross-talk, limited bandwidth, and great complexity and design effort to assure signal integrity, optic signal transmission offers significant advantages.

Planar waveguide structures used for the devices such as solid state lasers, solid state amplifiers, and nonlinear wavelength converters provide many attractive features for these devices. High intensity operation, thanks to confinement of light in a thin waveguide makes the device be compact and operate in efficient. In addition, large planar surface for heat reduction leads to a low thermal resistance of the device, and consequently, make it operate in high-power. Moreover, simple structure of planar waveguide device allows usage of wafer-processing for mass production, and consequently, makes the device cost very low. Taking these attractive features into account, we have been developing planar waveguide lasers and amplifiers for a wide variety of applications.

1.8 Fabrication processes

Various technologies have been employed for the fabrication of 1D PCs and planar waveguides, including ion-exchange [39], sol-gel [40 - 42], chemical vapour deposition [43], electron beam evaporation [44], pulsed laser deposition [45] and RFMS [46]. The sputtering technique plays an increasing role in the development of optical materials for application in integrated optics. The materials studied in this thesis have been fabricated by RFMS.

1.8.1 RF Sputtering technique

Sputtering is extensively used in the semiconductor industry to deposit thin films of various materials in integrated circuits processing. Thin anti-reflection coatings on glass, planar waveguides, etc. which are useful for photonic applications are deposited by sputtering. This technique is also used to fabricate thin film sensors, photovoltaic thin films (solar cells), metal cantilevers and interconnects etc. More details about sputtering technique can be found in Chapter 3.

1.9 Organization of the thesis

The thesis is organized into seven chapters. The results obtained in the context of 1D PCs and planar waveguides are briefly described in each of the chapters.

Chapter 1 gives a general introduction to photonic crystals and then mainly on 1D PCs related to basic concepts and planar waveguides. It also describes the motivation behind the research undertaken as a part of this thesis.

Chapter 2 is devoted for the discussion on the details of various experimental techniques that were carried out in this dissertation.

Chapter 3 describes the detailed protocol for the fabrication of one dimensional photonic crystals using rf sputtering. Visible and near infrared wavelength photonic crystals were prepared. The primary results on one dimensional photonic crystals such as transmittance, angle dependant reflection measurements and polarization dependant spectral characteristics were discussed and some of them are compared with theoretical results using simulations.

Chapter 4 involves the study of 1-D Er^{3+} doped dielectric microcavity. The cavity is constituted by an Er^{3+} doped SiO_2 active layer inserted between two Bragg reflectors consisting of ten pairs of $\text{SiO}_2/\text{TiO}_2$ layers. SEM microscopy is employed to show the quality of the sample, the homogeneities of the layer

thickness and good adhesion. NIR transmittance and variable angle reflectance spectra confirm that the presence of a stop-band from 1500 nm to 2000 nm with a cavity resonance centered at 1749 nm at 0° with a quality factor Q of about 890. The influence of the cavity on the $^4I_{13/2} \rightarrow ^4I_{15/2}$ emission band of Er^{3+} ion is also demonstrated.

Chapter 5 is devoted for the enhanced nonlinear optical response in one dimensional photonic crystals (1D) with ZnO defect. 1D photonic crystal containing ZnO defect layer was fabricated by rf sputtering technique. SEM images and the transmission spectra of this photonic crystal revealed a defect mode resonance and a broad photonic band gap. Open aperture z-scan measurements shows that the Z-scan curve of the detuned resonant photonic crystal exhibited a larger transmittance dip as compared to a single layer of ZnO reference. Nearly 21 times increase in the nonlinear absorption was observed for the photonic crystal structure when compared to a single layer of the ZnO reference. The enhancement of the nonlinear absorption in the detuned resonant photonic crystal is due to the strong confinement of the optical field around the defect layer. We have observed good optical limiting behaviour in photonic crystal which is due to the large enhancement of the optical field leading to stronger nonlinear absorption in the photonic crystal structure.

Chapter 6 GeO_2 based planar optical waveguides were characterized using a protocol combining radio frequency sputtering technique and CO_2 laser, positron irradiation effects. The effects of pulsed CO_2 laser irradiation on the optical and structural properties of the waveguides are evaluated by different techniques such as m-line, micro-Raman spectroscopy and atomic force microscopy (AFM). Amorphous GeO_2 planar waveguides were fabricated by radio frequency magnetron sputtering system on v- SiO_2 substrate. After pulsed CO_2 laser annealing, an increase of the refractive index of approximately 0.04 at $1.5 \mu\text{m}$ and a decrease of the attenuation coefficient from 0.9 to 0.5 dB/cm at $1.5 \mu\text{m}$ was observed. Raman spectroscopy and AFM results put in evidence that after an adapted pulsed CO_2 laser annealing, the system showed a crystalline

environment in which the phase of the crystalline GeO₂ varies with varying irradiation time. Moreover, positron annihilation spectroscopy was used to study the depth defect profiling of the as prepared and laser annealed samples. The obtained results allowed us getting information on the structural changes produced inside the waveguides films of approximately 1 μm thickness after the irradiation process. In addition, a higher density value for the amorphous GeO₂ samples was obtained.

Chapter 7 summarizes the results obtained in this dissertation work and future implications and perspectives of the work carried out are discussed in brief.

1.10 References

1. J. D. Joannopoulos, R. D. Meads and J. N. Winn, “*Photonic Crystals: Molding the Flow of Light*” Princeton University, Princeton, N.J. 1995.
2. J. Martorell and N. M. Lawandy, “Observation of inhibited spontaneous emission in a periodic dielectric structure,” *Phy. Rev. Lett.* **65**, 1877-1880 (1990).
3. E. Ozbay, E. Michel, G. Tuttle, R. Biswas, M. Sigalas and K.M. Ho, “Micromachined millimeter-wave photonic band gap crystals,” *Appl. Phy. Lett.* **64**, 2059-2061 (1994).
4. P. Russell, and T. A. Birks, “Bloch Wave Optics in Photonic Crystals: Physics and Applications,” *Photonic Band Gap Materials, NATO ASI Series, Series E: Applied Science* **315**, 71-91 (1995).
5. M. Lipson and L. C. Kimerling, “Er³⁺ in strong light-confining microcavity,” *Appl. Phy. Lett.* **77**, 1150 (2000).
6. S. Sebastiani, G. Nunzi Conti, S. Pelli, G. C. Righini, A. Chiasera, M. Ferrari, and C. Tosello, “Characterization of a highly photorefractive RF-sputtered SiO₂-GeO₂ waveguide,” *Opt. Express* **13**, 1696 (2005).

7. V. P. Prakapenk, G. Shen, L. S. Dubrovinsky, M. L. Rivers and S. R. Sutton, “High pressure induced phase transformation of SiO₂ and GeO₂: difference and similarity,” *J. Phys. Chem. Solids* **65**, 1537 (2004).
8. J. C. Knight, J. Broeng, T. A. Birks and P. S. J. Russell, “Photonic Band Gap Guidance in Optical Fibers,” *Science* **282**, 1476 (1998).
9. T. Hattori, N. Tsurumachi and H. Nakatsuka, “Analysis of optical nonlinearity by defect states in one-dimensional photonic crystals,” *J. Opt. Soc. Am. B* **14**, 348 (1997).
10. L. Rayleigh, XVII. “On the maintenance of vibrations by forces of double frequency, and on the propagation of waves through a medium endowed with a periodic structure,” *Philosophical Magazine Series 5* **24**, 145–159 (1887).
11. P. Yeh, A. Yariv and C. S. Hong, “Electromagnetic propagation in periodic stratified media. II. Birefringence, phase matching, and x-ray lasers,” *J. Opt. Soc. Am.* **67**, 423 (1977).
12. V. P. Bykov, “Spontaneous emission from a medium with a band spectrum,” *Soviet Journal of Quantum Electronics* **4**, 861–871 (1975).
13. E. Yablonovitch, “Inhibited Spontaneous Emission in Solid-State Physics and Electronics” *Phys. Rev. Lett.* **58**, 2059–2062 (1987).
14. S. John, “Strong localization of photons in certain disordered dielectric superlattices,” *Phys. Rev. Lett.* **58**, 2486–2489 (1987).
15. E. Yablonovitch and K. M. Leung, “Hope for Photonic Bandgap,” *Nature* **351**, 278 (1991).
16. E. Yablonovitch, T. J. Gmitter and K. M. Leung, “Photonic Band Structure: The Face-Centered-Cubic Case Employing Nonspherical Atom,” *Phys. Rev. Lett.* **67**, 2295 (1991).
17. K. M. Ho, C. T. Chan and C. M. Soukoulis, “Existence of a Photonic Bandgap in Periodic Dielectric Structures,” *Phys. Rev. Lett.* **65**, 3152 (1990).
18. E. Yablonovitch and T. J. Gmitter, “Photonic Band Structure: The Face-Centered-Cubic Case,” *Phys. Rev. Lett.* **63**, 1950 (1989).

19. E. Yablonovitch, "Photonic bandgap structures," *J. Opt. Soc. Am B* **10**, 283 (1993).
20. S. Noda, N. Yamamoto, H. Kobayashi, M. Okano and K. Tomoda, "Optical properties of three-dimensional photonic crystals based on III–V semiconductors at infrared to near-infrared wavelengths," *Appl. Phys. Lett.* **75**, 905 (1999).
21. G. Subramania, Y. J. Lee, A. J. Fischer and D. D. Koleske, "Log-Pile TiO₂ Photonic Crystal for Light Control at Near-UV and Visible Wavelengths," *Advanced materials* **22** (4), 487 (2010).
22. E. Yablonovitch, "Photonic crystals," *J. Mod. Opt.* **41**, 173 (1994).
23. C. Kittel, "Introduction to Solid State Physics," 7th Ed., John Wiley & Sons, Inc. New York (1996).
24. S. Y. Lin, E. Chow, V. Hietala, P. R. Villeneuve and J. D. Joannopoulos, "Experimental Demonstration of Guiding and Bending of Electromagnetic Waves in a Photonic Crystal," *Science* **282** 274 (1998).
25. K. M. Ho, C. T. Chan and C. M. Soukoulis, "Existence of a photonic gap in periodic dielectric structures," *Phys. Rev. Lett.* **65**, 3152–3155 (1990).
26. R. L. Liboff, "Introductory Quantum Mechanics," 2nd ed., Addison-Wesley, Reading, M.A (1992).
27. E. Merzbacher, "Quantum Mechanics," Wiley, New York (1961).
28. J. D. Jackson, "Classical Electrodynamics," 2nd ed., Wiley, New York (1975).
29. K. W. Shung and Y.C. Tsai, "Surface effects and band measurements in photonic crystals," *Phys. Rev. B* **48**, 11265 (1993).
30. N. W. Ashcroft and N. D. Mermin, "Solid State Physics" Saunders, Philadelphia (1976).
31. A. D. McAulay, "Optical computer architectures: the application of optical concepts to next generation computers" Wiley, New York (1991).
32. P. Yeh, "Optical waves in layered media" Wiley (2005).

33. P. J. Kim, S. Y. Park, M. D. Huang, Y. H. Lu, Y. P. Lee and J. Y. Rhee, “Fabrication of Oxide Materials for One-Dimensional Photonic Crystals,” *J. Korean Phys. Soc.* **49** (3), 869 (2006).
34. J. Lekner, “Omnidirectional reflection by multilayer dielectric mirrors,” *J. Opt. A: Pure Appl. Opt.* **2**, 349 (2000).
35. L. Persano, P. D. Carro, E. Mele, R. Cingolani, D. Pisignano, M. Zavelani-Rossi, S. Longhi and G. Lanzani, “Monolithic polymer microcavity lasers with on-top evaporated dielectric mirrors,” *Appl. Phys. Lett.* **88**(12), 121110 (2006).
36. S. F. Chichibu, T. Ohmori, N. Shibata and T. Koyama, “Dielectric SiO₂/ZrO₂ distributed Bragg reflectors for ZnO microcavities prepared by the reactive helicon-wave-excited-plasma sputtering method,” *Appl. Phys. Lett.* **88**(16), 161914 (2006).
37. Y. Li and R. M. Almeida, “Photoluminescence from a Tb-doped photonic crystal microcavity for white light generation,” *J. Phys. D* **43**(45), 455101 (2010).
38. A. Boudrioua, “*Photonic Waveguides: Theory and applications*” Series Editor Pierre-Noël Favennec, Wiley Publishers (2009).
39. P. M. Peters, D. S. Funk, A. P. Peskin, D. L. Veasey, N. A. Sanford, S. S. Houde-Walter and J. S. Hayden, “Ion-exchanged waveguide lasers in Er³⁺/Yb³⁺ co-doped silicate glass,” *Appl. Opt.* **38**, 6879 (1999).
40. X. Orignac, D. Barbier, X.M. Du, R.M. Almeida, O. McCarthy, and E. Yeatman, “Sol-gel silica/titania-on-silicon Er/Yb-doped waveguides for optical amplification at 1.5 μm,” *Opt. Mater.* **12**, 1 (1999).
41. Y. Li, L. M. Fortes, A. Chiappini, M. Ferrari and R. M. Almeida, “High quality factor Er-doped Fabry-Perot microcavities by sol-gel processing,” *J. Phys. D Appl. Phys.* **42**(20), 205104 (2009).
42. J. Jasieniak, C. Sada, A. Chiasera, M. Ferrari, A. Martucci and P. Mulvaney, “Sol-gel based vertical optical microcavities with quantum dot defect layers,” *Adv. Funct. Mater.* **18**(23), 3772–3779 (2008).

43. G. Grand, J. P. Jadot, H. Denis, S. Valette, A. Fournier and A. M. Grouillet, “Low-loss PECVD silica channel waveguides for optical communication,” *Elect. Lett.* **26**, 2135 (1990).
44. G. Ma, J. Shen, Z. Zhang, Z. Hua and S. H. Tang, “Ultrafast all-optical switching in one-dimensional photonic crystal with two defects,” *Opt. Express* **14(2)**, 858–865 (2006).
45. R. Serna, C. N. Afonso, J. M. Ballesteros and A. Zschocke, “Pulsed laser deposition for optical doping of active waveguide films,” *Appl. Surf. Science* **524**, 109-110 (1997).
46. A. Chiasera, R. Belli, S. N. B. Bhaktha, A. Chiappini, M. Ferrari, Y. Jestin, E. Moser, G. C. Righini and C. Tosello, “High quality factor Er^{3+} -activated dielectric microcavity fabricated by RF sputtering,” *Appl. Phys. Lett.* **89(17)**, 171910 (2006).

Chapter 2

Experimental techniques and details

Abstract:

We have used different experiments for the characterization of photonic crystals and planar waveguides. In this chapter, we briefly describe the experimental techniques, some of them are commercial set up such as spectrophotometer for the preliminary studies of photonic crystals, m-line spectroscopy which is based on prism coupling technique was used for the measurement of optical properties, scanning electron microscopy (SEM) for the surface morphology of multilayer films, and the Raman spectrometer. Some of the techniques which were set up in the lab, such as room temperature photoluminescence measurement and a modified Z-Scan technique were briefly described.

2.1 Introduction

Optical spectroscopic techniques are widely used in the study of optical properties of different materials including multilayer films and planar waveguides. These different techniques are usually based on measuring absorption, emission of light that contains information about properties of the materials. Commonly used techniques include electronic absorption (UV-Vis-NIR), photoluminescence (PL) and Raman scattering techniques. Other more specialized techniques include nonlinear optical techniques such as Z-scan technique for third order nonlinear optical properties measurement. Also, some other techniques, such as field emission scanning electronic microscopy (FESEM) and atomic force microscopy (AFM) techniques will provide the information about surface morphology of materials like multilayer films. In this chapter, several common optical and spectroscopic techniques are explained with emphasis on their principle of operation as well as spectral interpretation. The main objective is to explain how one can get useful physical information about the materials under study from the optical, spectroscopic and nonlinear optical properties that measured experimentally.

2.2 Optical and spectroscopic techniques

2.2.1 Absorption spectrophotometer

UV-visible spectroscopy is one of the simplest and most useful optical techniques for studying optical properties of the materials. The transmission and reflection optical characteristics are carried out using a commercial Ultra Violet-Visible- Near Infrared (UV-Vis-NIR) double-beam spectrophotometer (JASCO V-670). The spectrophotometer uses two light sources, a deuterium (D_2) lamp for ultraviolet region and a halogen lamp for visible and near infrared region. It utilizes a unique, single monochromator design covering a wavelength range from 190 nm to 2700 nm. The monochromator features dual gratings: 1200

grooves/mm for the UV/Vis region; 300 grooves/mm for the NIR region. A PMT detector is provided for the UV/Vis region and a Peltier-cooled lead sulphide (PbS) detector is employed for the NIR region. Both gratings and detector are automatically exchanged within the user selectable 750 nm to 900 nm range.

The light from the source lamp gets reflected from mirror 1 and beam passes through slit 1 (S_1) and hits a diffraction grating. The grating can be rotated allowing for a specific wavelength to be selected. At any specific orientation of the grating, only monochromatic (single wavelength) beam successfully passes through slit 2 (S_2). A filter (F) is used to remove unwanted higher order diffraction beam. The light beam hits a second mirror (M_2) before it gets split by a half mirror (M_3) (half of the light is reflected, the other half gets transmitted). One of the beams is allowed to pass through a reference sample (air in the present case), the other passes through the sample. The intensities of the light beams are then measured at the end as shown in Figure 2.1. The photometer computes the ratio of the sample signal to the reference signal (I/I_0) to obtain the transmittance.

The spectrometer is provided with three different measurement accessories: 1) variable angle transmittance, 2) fixed angle and 3) variable angle reflectance. The schematic of the beam path in the spectrometer is shown in the Figure 2.1. The optical path of the fixed angle (5°) reflectance measurement accessory in the path of the sample beam is presented in Figure 2.1 (b). We have used an aluminium mirror for standard reference.

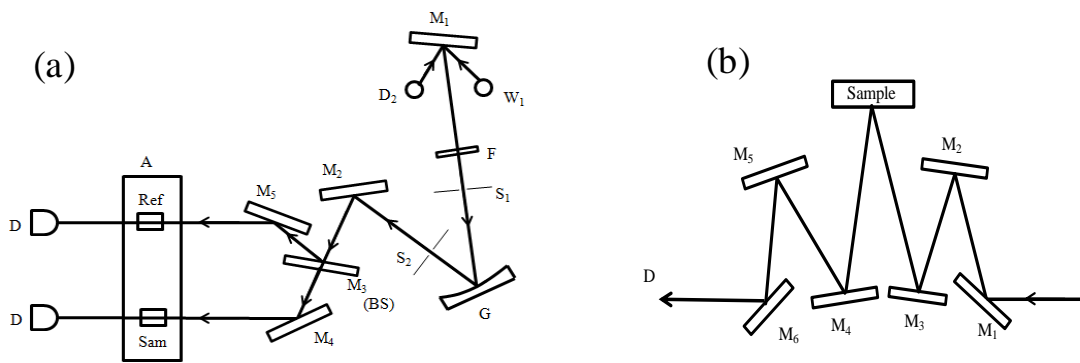


Figure 2.1: a) Schematic of the optical setup of the commercial JASCO spectrometer for a) transmission and b) fixed angle (5°) reflection geometry. W1: Halogen lamp, D₂: Deuterium lamp, S: Slit, F: filter, G: grating, BS: Beam splitter, M: Mirror, A: Accessory, Sam: Sample, Ref: Reference beam, D: Detector.

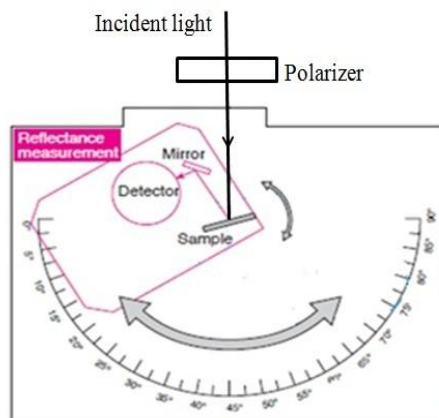


Figure 2.2: Schematic of the beam path of the absolute reflectance measurement accessory for JASCO spectrometer.

The polarization dependent studies are carried out in the reflection geometry and their spectral characteristics are compared with s-, p- and unpolarized light. The schematic of the absolute reflectance measurement accessory is shown in Figure 2.2. The sample, reflecting mirror and detector are mounted on a single rotational stage. Absolute reflectance is measured by rotating this stage to determine the angle of the light incident upon the sample.

The detector is equipped with an integrating sphere and thus it permits measurement of the relative reflectance of a diffusely reflecting sample. The polarization of the beam is selected using Glan-Taylor prism polarizer. This accessory allows recording the reflectance from 5-70° only.

2.2.2 M-Line spectroscopy

M-line spectroscopy is mainly based on the prism coupling technique that analyzes the mode angles of a thin film to determine the thickness and index of refraction of the film and also measurement of optical losses in waveguides [1, 2]. If two or more modes are measured, and they are the first modes ($m = 0, 1, 2\dots$), then a reliable measurement of the index and thickness of the film can be made. The schematic of the m-line technique based on prism technique is shown in Figure 2.3.

2.2.2.1 Refractive index and thickness measurement

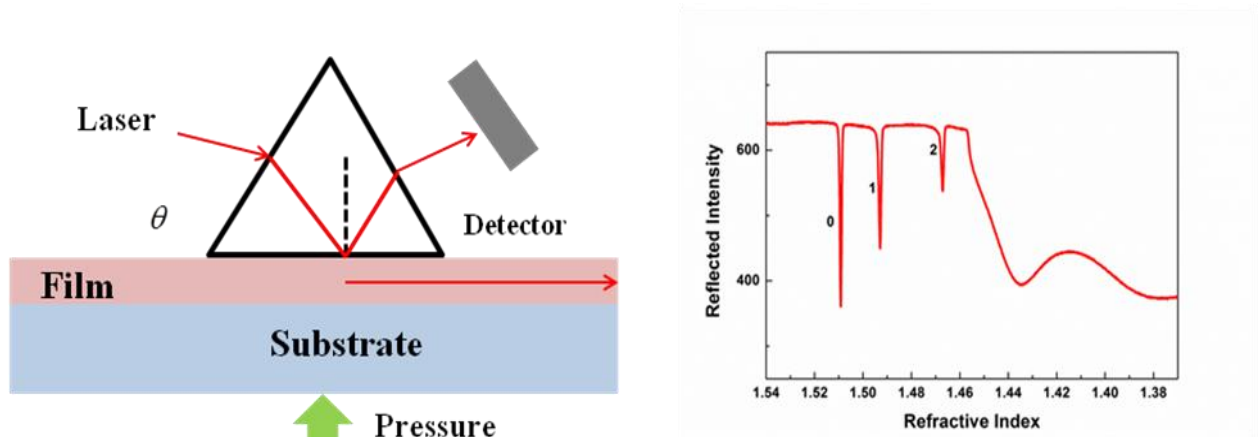


Figure 2.3: Measurement principle for thin film

A conventional Metricon model 2010 apparatus is shown in Figure 2.4. The excitation sources (two He-Ne lasers with 632.8 and 543.5 nm lines plus an external tunable argon laser with emission at 457, 477, 488, 496 and 514 nm) permit to measure the refractive index at several wavelengths. For the optical characterization in the NIR region, a second Metricon apparatus with the 632.8, 1330 and 1540 nm lines and with losses measurement option is used. Both TE

and TM modes can be measured inserting a polarisation rotator ($\lambda/2$) on the beams.

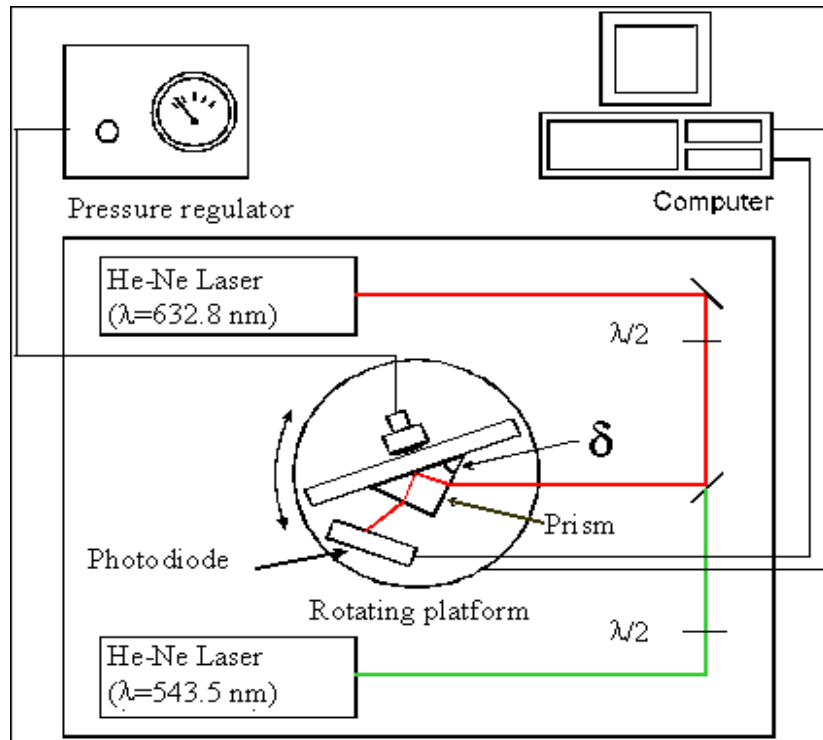


Figure 2.4: Schematic of the *m*-line system.

The sample to be measured (Figure 2.3) is brought into contact with the base of a prism by means of a pneumatically-operated coupling head, creating a small air gap between the film and the prism. A laser beam strikes the base of the prism and is normally totally reflected at the prism base onto a photo detector. At certain discrete values of the incident angle, called mode angles, photons can tunnel across the air gap into the film and enter into a guided optical propagation mode, causing a sharp drop in the intensity of light reaching the detector. To a rough approximation, the angular location of the first mode (dip) determines film index, while the angular difference between the modes determines the thickness and index to be measured completely independently. The number of modes supported by a film of given index increases with film thickness. For most film/substrate combinations, a thickness of 100-200 nm is required to support the first mode, while films in the one micron range can support as many as four or

five modes. If the film is thick enough to support two or more propagation modes (typically 300 nm - 500 nm), the Model 2010 calculates thickness and index for each pair of modes, and displays the average and standard deviation of these multiple estimates.

2.2.2.2 Loss measurement

This option measures loss of optical waveguides by scanning a fiber optic probe and photo detector down the length of a propagating streak to measure the light intensity scattered from the surface of the guide. The assumption is that at every point on the propagating streak the light scattered from the surface and picked up by the fiber is proportional to the light which remains within the guide. The best exponential fit to the resulting intensity vs distance curve yields the loss in dB/cm. This method offers the advantages of quickness (typical measurement time, including the exponential fit, is 2-3 min) and simplicity (absolutely no sample preparation beyond creation of the layers which form the guide is required). The loss measurement set up is shown in Figure 2.5.

Power attenuation coefficients for waveguide can be obtained by an exponential fit of equation

$$I(z) = I_0 10^{-\frac{\alpha}{10}z}$$

where z is the distance in the longitudinal direction (in cm) and $I(z)$ is the intensity along the z direction (averaged with respect to the stripe width).

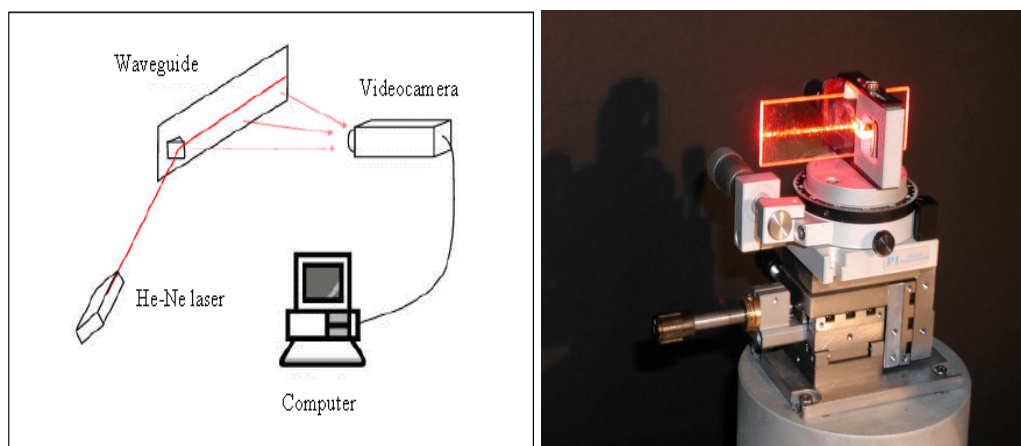


Figure 2.5: *Loss measurement equipment*

2.2.3 Room temperature photoluminescence measurement

At the fundamental level, the principle underlying in photoluminescence (PL) spectroscopy is very similar to that of electronic absorption spectroscopy. They both involve electronic transition of initial and final states coupled by the electric dipole operator. The main difference is that the transition involved in PL is from a higher energy level or state to a lower energy level. A typical PL spectrum is just a plot of the PL intensity as a function of wavelength for a fixed excitation wavelength.

The laser used for this measure is a continuous Argon green laser operating at 514.5 nm. We could use a pumping source with an energy around 7000 cm^{-1} but a laser source set at this energy would not be in the visible domain and it would be obviously very difficult to align the measurement device. Thus, we keep the 514.5 nm laser source. The source is chopped at a define frequency and focused on the sample to excite the rare earth ions inside. The luminescence emitted by the sample is measured perpendicularly to the laser source (in order to avoid measuring it) and focused on the monochromator. The monochromator selects the light transmitted at a defined wavelength, and then the signal is detected by the photo multiplier tube (PMT) which counts the photons and converts the optic signal into an electric signal which is fed to a lock-in amplifier. At the same time, the frequency of the reference triggered signal of the chopper is

transmitted to the lock-in amplifier. The photoluminescence signal is extracted from the PMT by synchronous detection by the lock-in amplifier. The signal is finally transmitted to the computer which can finally reproduce the luminescence spectrum.

Figure 2.6 shows the home made room temperature PL set up for collecting the emission from the materials in NIR region. The Argon laser is used at 514.5 nm (which corresponds to an Er^{3+} Absorption wavelength) with an energy power around 180 mW. The monochromator uses a single diffraction grating of 600 lines/mm optimized to 1.5 μm . The width of the monochromator slits is chosen at 1 mm (corresponding to a resolution of 2 nm) which is the maximum for a measure and adapted for the wide Er spectra. The spectra is recorded between 1400 and 1700 nm in the range on the ${}^4\text{I}_{13/2} \rightarrow {}^4\text{I}_{15/2}$ transition of Er^{3+} with an acquisition step of 0.5 nm and an integration time of 2 sec.

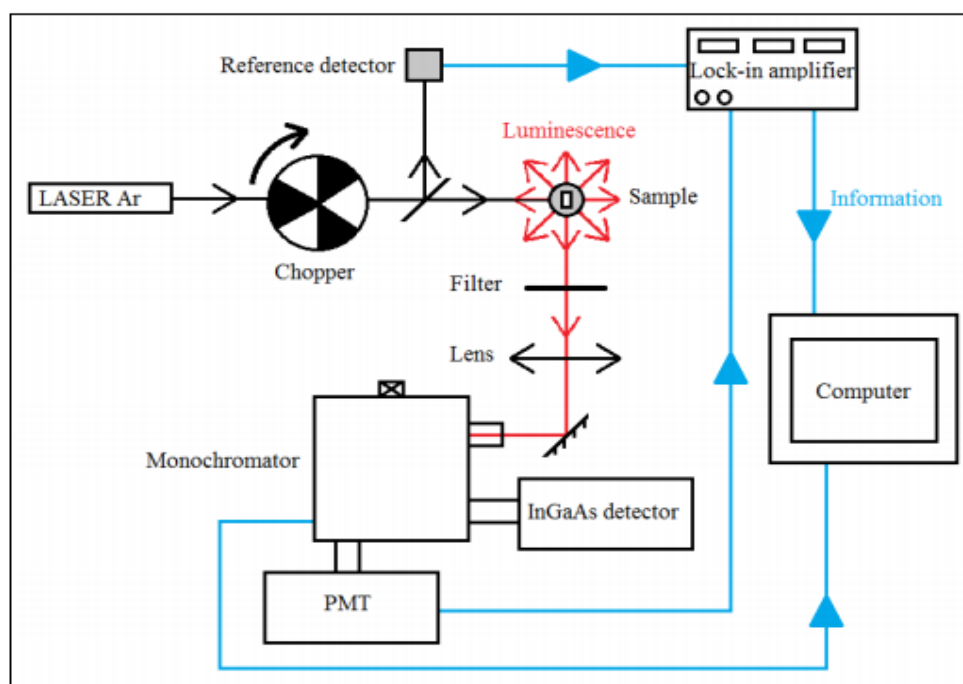


Figure 2.6: Schematic of the NIR region room temperature photoluminescence measurement set up.

The intensity of luminescence with respect to the time is measured with a digital oscilloscope in order to calculate the lifetime of the luminescence into the sample. This measurement indicates if the layer is fully densified or not. The decay measurement is exploited with the software “Origin”. An exponential fit of the curve is realized with the formula: $y = ae^{-\frac{x}{\tau}} + y_0$ with $a=1$ and $y_0=0$, so, the lifetime value τ can be obtained.

2.2.4 Micro-Raman spectrometer

Raman spectroscopy is a light scattering technique, and can be thought of in its simplest form as a process where a photon of light interacts with a molecule in the sample to produce scattered radiation of different frequency. If frequency of scattered photon is less than the incident photon, then it is known as Stokes scattering. If frequency of scattered photon is greater than the incident photon then it is called anti-Stokes scattering. Raman spectroscopy is extremely information rich, for example it is useful for chemical identification, characterization of molecular structures, effects of bonding, environment and stress on a sample.

In Raman experiments, the sample is irradiated with monochromatic light and the scattered light is traditionally observed at right angles to the incident radiation. However, in modern confocal Raman microscopes, the scattered signals are recollected by a microscope objective in 180° geometry. Selection of appropriate light source for micro-Raman spectroscopy is of great importance because the Raman signals are usually much weaker than the excitation intensity. For strong scattering material only one Raman scattered photon can be explored for every 10^7 incident photons. Further a coherent light source (laser) is preferred due to its high power, monochromatic and collimated beam nature. The most commonly used laser sources in Raman applications are

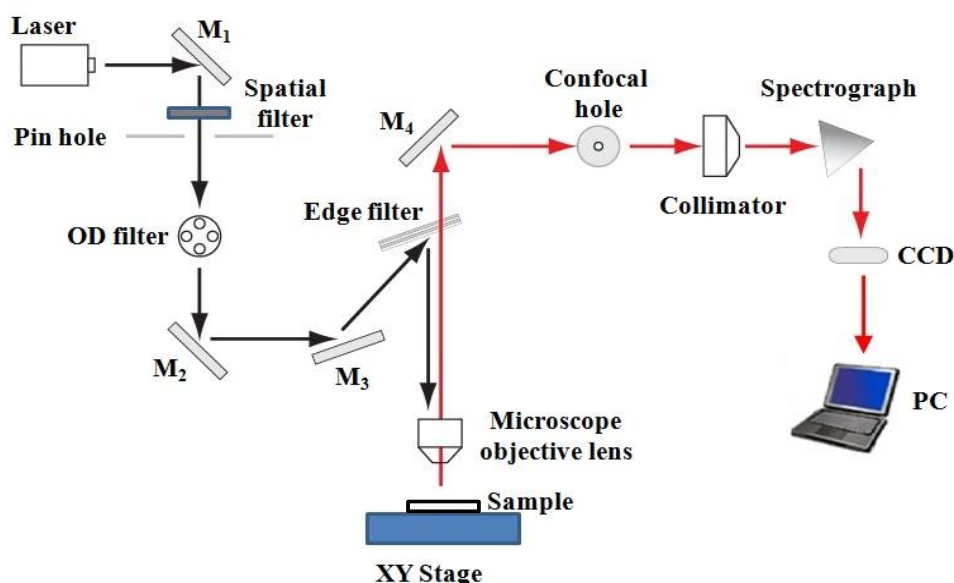


Figure 2.7: Schematic of a micro-Raman spectrometer.

He - Ne, Ar⁺ ion and diode lasers delivering at 632.8 nm, 514.5 nm and 785 nm respectively.

In the present work Raman scattering measurements were performed with a LabRAM HR800 micro-Raman spectrometer manufactured by HORIBA Jobin Yvon. It includes a variety of optical components arranged as illustrated in Figure 2.7. A collimated laser beam is sequentially passed through several optical components including the spatial filter, optical density filters, an edge filter which serves as a dichroic mirror, and the microscope objective lens which focuses the beam on the core sample. An automated x-y motorized stage allows moving the sample to acquire Raman spectra at each position. The scattered radiation emanating from the sample is collected through the same objective lens and is passed through the edge filter for elimination of the excitation line. A controllable slit and a confocal hole are used before the Raman radiation reaches the spectrograph. The spectrograph utilizes two gratings with 600 and 1800 lines/mm. The spectrograph focuses the scattered wavelength spectrum on a CCD camera. All these optical components are controlled through a graphical user interface on a computer attached to the system.

2.3 Nonlinear optical properties measurement:

2.3.1 Z-scan technique

The Z-scan technique is a single beam technique, which allows the determination of the real and imaginary parts of the third order susceptibility [3]. This technique is a simple, sensitive, single beam method that uses the principle of spatial beam distortion to measure both the sign and the magnitude of refractive nonlinearities of optical materials. The experiment uses a Gaussian beam from a laser in tight focus geometry to measure the transmittance of a nonlinear medium through a finite aperture in the far field as a function of the sample position Z , from the focal plane. In addition to this, the sample transmittance without an aperture is also measured to extract complementary information about the absorptive nonlinearities of the sample.

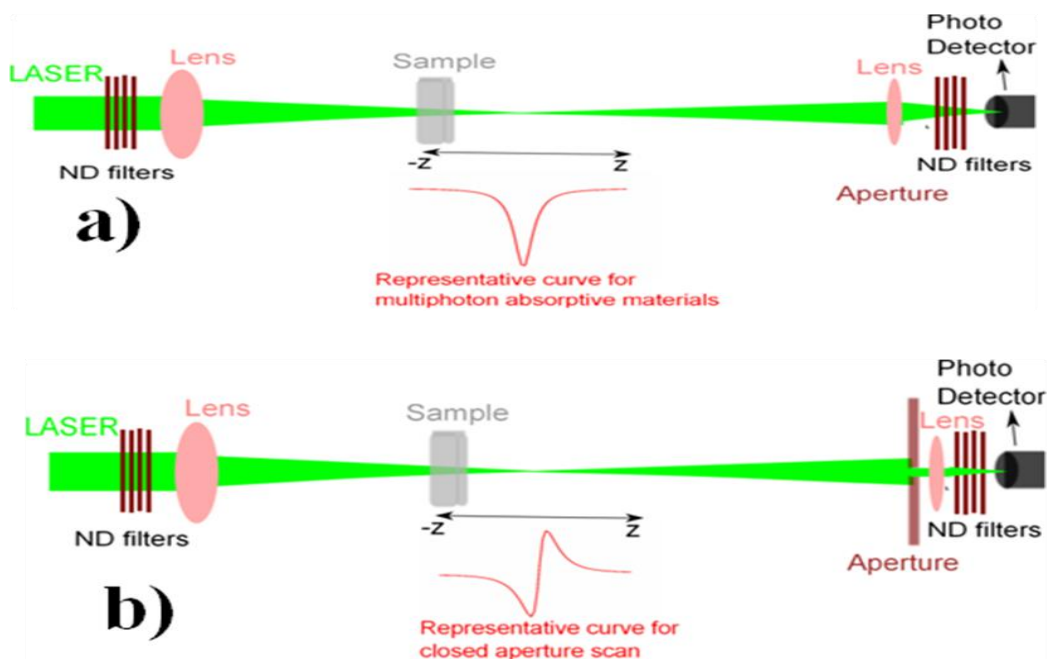


Figure 2.8: Schematic of a Z-scan setup. (a) Open aperture; (b) Closed aperture.

2.3.2 Open-aperture Z-scan for absorptive nonlinearity

In the above discussion a purely refractive nonlinearity was considered assuming that absorptive nonlinearities are absent. The presence of multi-photon (two or more) absorption suppresses the peak and enhances the valley, while saturation of absorption produces the opposite effect. The sensitivity of the experiment to refractive nonlinearities is entirely due to the aperture. The removal of the aperture will make the Z-scan sensitive to absorptive nonlinearities alone. The schematic of an open aperture Z-scan is as shown in Figure 2.8 (a).

2.3.3 Closed-aperture Z-scan for sign and refractive nonlinearity

Consider, for instance, a material with a negative nonlinear refraction and of thickness smaller than the diffraction length $\pi\omega_0^2 / \lambda$ of the focused beam being positioned at various positions along the Z-axis as shown in Figure 2.8 (b). This situation can be regarded as treating the sample as a thin lens of variable focal length due to the change in the refractive index at each position ($n = n_0 + n_2I$). When the sample is far from the focus and closer to the lens, the irradiance is low and the transmittance characteristics are linear. Hence, the transmittance through the aperture is fairly constant in this region. As the sample is moved closer to the focus, the laser irradiance increases, which inducing a negative lensing effect. A negative lens before the focus tends to collimate the beam. This causes the beam narrowing leading to an increase in the measured transmittance at the aperture (assuming a negative nonlinearity). A negative lens after the focus tends to diverge the beam resulting in the decrease of transmittance. As the sample is moved far away from the focus, the transmittance becomes linear in Z as the irradiance becomes low again. Thus the curve for Z versus transmittance has a peak followed by a valley for a negative refractive nonlinearity. The curve for a positive refractive nonlinearity will give rise to the opposite effect, i.e. a valley followed by a peak.

2.4 Surface morphology and compositional analysis

2.4.1 Field emission-scanning electron microscopy (FESEM)

The scanning electron microscopy is a versatile technique, which reveals the detailed information about the surface morphology and composition analysis of natural and manufactured materials. In our study, we have used FESEM for the obtaining cross sectional image of multilayer structures. Compared with conventional scanning electron microscopy (SEM), field emission SEM (FESEM) produces clearer, less electrostatically distorted images with spatial resolution down to several nanometers.

A field-emission cathode in the electron gun of a scanning electron microscope provides narrower probing beams at low as well as high electron energy, resulting in both improved spatial resolution and minimized sample charging and damage. A high energy (typically 10-30 keV) electron beam, emitted from a tungsten tip is focused to a spot size of 1 nm to 5 nm by the condenser magnetic lenses. The focused beam passes through a pair of scanning coils, which raster the beam across the surface. The secondary electrons emitted from the sample are detected by a scintillator-photomultiplier device and the resulting signal is rendered into a two-dimensional intensity distribution that can be viewed and saved as a digital image. The most common imaging mode monitors low energy (<50 eV) secondary electrons which originates within a few nanometers from the surface.

2.4.2 Atomic Force Microscopy

Atomic Force Microscope (AFM) is a high-resolution microscopy technique which produces precise topographic images of a sample by scanning the surface with a nanometer-scale probe. A unique advantage of AFM is that it enables imaging with minimal sample preparation, in air or liquid environment. AFM operates by measuring attractive or repulsive forces between a tip and the sample. In its repulsive "contact" mode, the instrument lightly touches a tip at

the end of a leaf spring or "cantilever" to the sample. As a raster scan drags the tip over the sample, some sort of detection apparatus measures the vertical deflection of the cantilever, which indicates the local sample height. Thus, in contact mode the AFM measures hard-sphere repulsion forces between the tip and sample. In noncontact mode, the AFM derives topographic images from measurements of attractive forces; the tip does not touch the sample.

2.5 References

1. P. K. Tien, "Light Waves in Thin Films and Integrated Optics", *Appl. Opt.* **10**, 2395 (1971).
2. R. Ulrich and R. Torge, "Measurement of Thin Film Parameters with a Prism Coupler," *Appl. Opt.* **12**, 2901 (1973).
3. M. Sheik-Bahae, A. A. Said, T.H. Wei, D.J. Hagan and E.W. Van Stryland, *IEEE J. Quant. Electron.* **QE-26**, 760 (1990).
4. JASCO Inc. Operational manuals for UV-Vis-NIR spectrophotometer.
5. Horiba Jobin Yvon manuals for micro-Raman spectrometer.

Chapter 3

Fabrication by rf sputtering and optical characterization of one dimensional photonic crystals

Abstract:

One dimensional photonic crystals containing stop band in visible and near NIR regions, are prepared using rf sputtering technique. The detailed protocol for the fabrication of one dimensional photonic crystals using rf sputtering is discussed. The optical properties of one dimensional photonic crystals such as transmittance, angle dependant reflection measurements and polarization dependant spectral characteristics are discussed. Some of the results compared with theoretical simulations.

3.1 Introduction

One dimensional (1D) photonic crystals have been produced and used widely for a long time as, for instance, anti reflection coatings, notch filters, microcavity lasers, optical switches, nonlinear optical devices and so on. Due to their many applications, the fabrication of photonic crystals and planar waveguides has become a challenging tool for many researchers. The control of photon modes by using photonic crystals may open up a key technology for future photonic devices [1] that could satisfy the demand for faster computers and optical communications. According to dimensionality, photonic crystals can be classified mainly into three categories: one-dimensional (1D), two-dimensional (2D), and three-dimensional (3D). Since the period of the structure should be comparable to the wavelength of the light, it is difficult to fabricate 3D PCs for use in the visible region in certain materials because of their small lattice constant [2, 3]; which can be easily overcome in the infrared region [4]. Because of the structural simplicity and the ease of fabrication with thin film deposition techniques, 1D photonic crystals are very attractive for practical applications. The position and width of the photonic crystals are mainly determined by refractive index contrast of the constituent materials of photonic crystals. Oxide-based dielectric materials are particularly suitable for fabricating photonic bandgap (PBG) structures because they have wide transparency from the ultraviolet to the near-infrared [5, 6]. Among these oxide base materials, because of the ease of availability of the targets, we have opted SiO_2 and TiO_2 for the fabrication of multilayer structures.

The high reflectivity of one dimensional Bragg mirror is a well known phenomenon that has been studied for a long time. However, it is just recently that the required conditions to obtain omnidirectional reflection for arbitrary polarizations with 1D photonic crystals have been recognized [7]. Winn et al. have shown theoretically [8] and experimentally [7] that a perfect PBG (omni-

PBGs), which was once thought to exist only in 3D PCs, can be obtained for both transverse electric (TE) and transverse magnetic (TM) polarizations even in a 1D photonic crystal. This fact has great scientific and practical importance because it offers a possibility to control the propagation of light (from soft X-rays to microwave) in 1D photonic crystals with a rather simple multilayer structure at an arbitrary angle of incidence. Much interest has been shown and many efforts have been put in to investigate these omni-PBGs in 1D photonic crystals consisting of dielectric multilayers [9 - 14]. This chapter devoted for the fabrication of one dimensional photonic crystals using rf sputtering technique. Optical properties were discussed and some of the results were compared with theoretical results based on transfer matrix method (TMM).

3.2 Fabrication of one dimensional photonic crystals

If two dielectric materials with low (L) and high (H) indices of refraction, n_L and n_H respectively, are alternatively stacked and each layer has an optical thickness of a quarter wavelength ($\lambda/4$, λ is the free space wavelength). This dielectric stack can reflect both polarizations of specific wavelength band for all angles of incidence, i.e., it may form an omni directional reflector. Such a structure is referred to as distributed Bragg reflector (DBR). Since propagation of light in the wavelength band centered at λ is not allowed inside this structure and its refractive index is periodic along the stack normal, this constitutes a 1D PBG structure. Due to their increasing applications in the field of telecommunications, optoelectronics, nonlinear optical devices etc, the fabrication of PBG structures has become challenging tool for the researchers. Though various techniques have been used to fabricate one dimensional photonic crystals and microcavities, few methods are discussed below.

3.2.1 Sol – gel technique

The sol–gel method, which is a wet chemical fabrication technique, is a good technique to fabricate the planar microcavities. The sol–gel process is based on a chemical transformation of liquid alkoxide precursors into solid state

products by hydrolysis and polymerization reactions at room temperature. The advantages of this technique are the high optical quality of the deposited films and the large variety of materials which can be formed as thin layers. This flexibility is related to the incorporation process of the doping materials. These materials are included in liquid phase during the sol fabrication and are physically encapsulated in the layer when it polymerizes, assuring homogeneous repartition of the dopants in the thin film. But there are some disadvantages occurring with sol-gel process such as cracks will be forming in the films due to internal stress, etc. The sol-gel process allows the fabrication of good quality microcavities doped with materials such as semiconductor nanocrystals or organic molecules that are difficult to include with vapour phase methods [15 – 17].

3.2.2 Electron beam evaporation

E-beam evaporation is a process in which a source material is heated above its boiling/sublimation temperature and evaporated to form a film by the evaporated atoms on the substrate surface. This evaporation method is similar to thermal evaporation. A noticeable advantage of e-beam evaporation over thermal evaporation is the possibility to add a larger amount of energy into the source material. This yields a higher density film with an increased adhesion to the substrate. Because the electron beam only heats the source material and not the entire crucible, a lower degree of contamination from the crucible will be present than in the case of thermal evaporation. By using a multiple crucible E-beam gun, several different materials can be deposited without breaking the vacuum.

In e-beam evaporation technique, an electron beam is aimed at the source material causing local heating and evaporation. With the source material placed in the crucible a filament below the crucible is heated. By applying a large voltage, electrons are drawn from the cathode filament and focused as a beam on the source material by several bending magnets. The beam is swept across the surface of the source material to heat all of the material. By using a multiple

crucible E-beam gun, several different materials can be deposited without breaking the vacuum. This technique is also called low temperature electron-beam evaporation and acts a powerful and straightforward fabrication technique for molecular-based fully integrable microcavity resonators. In this way, it is possible to fabricate 1D photonic crystals [18].

3.2.3 Radio Frequency Magnetron Sputtering Technique (RFMS)

Sputtering is extensively used in the semiconductor industry to deposit thin films of various materials in integrated circuits processing. Thin anti reflection coatings on glass, which are useful for optical applications, are normally deposited by sputtering. Because of the low substrate temperatures used, sputtering is an ideal method to deposit contact metals for thin film transistors. This technique is also used to fabricate thin film sensors, photovoltaic thin films (solar cells), metal cantilevers and interconnects, etc. With the use of multi target facility, it is easier to fabricate multilayer structures of different dielectric materials. In the present work, we have demonstrated that radio frequency magnetron sputtering (RFMS) technique is a suitable technique for the fabrication of 1D photonic crystals, dielectric microcavities and that it is a cheap and versatile technique to deposit alternating layers of different materials with controlled refractive index and thickness [5, 6].

Sputter deposition is a physical vapour deposition process for depositing thin films. Sputtering means ejecting material from a target and depositing it on a substrate such as a silicon wafer. The target is the source material. Targets and substrates are placed in a vacuum chamber and is pumped down to a prescribed pressure. Sputtering starts when a negative voltage is applied to the target causing a plasma or glow discharge. Positive charged gas ions generated in the plasma region are attracted to the negatively biased target plate at a very high speed. This collision creates a momentum transfer and ejects atomic size particles from the target. These particles are deposited as a thin film into the surface of the substrate.

Sputtering can be done either in DC or RF modes. DC sputtering is done with conducting materials. If the target is a non conducting material, the positive charge will build up on the material and it will stop sputtering. RF sputtering can be done for both conducting and non conducting materials. This technology uses powerful magnets to confine the “glow discharge” plasma to the region closest to the target plate. That vastly improves the deposition rate by maintaining a higher density of ions, which makes the electron/gas molecule collision process much more efficient.

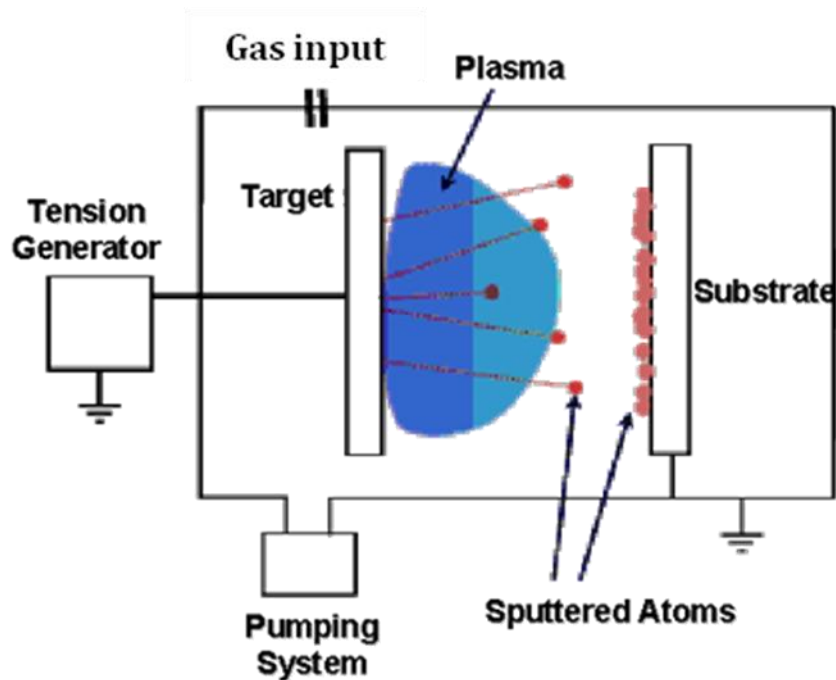


Figure 3.1: Schematic diagram for rf sputtering process.

A Radio Frequency magnetron sputtering (RFMS) system consists of a vacuum chamber, a target (cathode) and a substrate table (anode) as shown in Figure 3.1. A radio frequency oscillating voltage is applied between the target and substrate. During the sputtering process plasma is created in the chamber and ions (Argon ions in the present case) out of plasma are accelerated towards a target consisting of the material to be deposited. Material is detached ('sputtered') from the target and afterwards deposited on a substrate in the

vicinity. The process is realized in a closed chamber, which is pumped down to a vacuum base pressure before deposition starts.

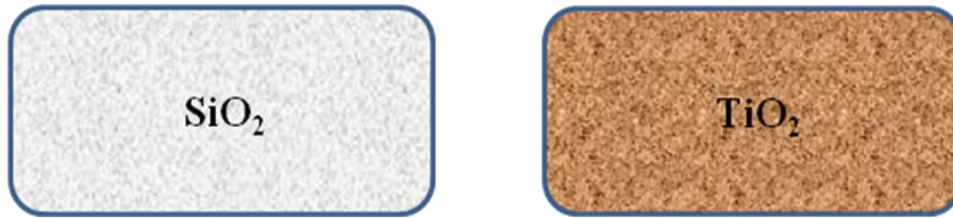


Figure 3.2: Targets used for fabrication of SiO₂ and TiO₂ thin films

Deposition is performed by sputtering alternatively changing the targets of SiO₂ and TiO₂ which are shown in Figure 3.2. The following steps are involved in the fabrication of 1D photonic crystals and microcavity in visible and NIR regions.

- ◆ Before the deposition process, the substrates should be cleaned inside the small vacuum chamber using IR lamp at 120 °C for 30 min. In this process the gas particles on the substrates will be completely removed inside the vacuum chamber.
- ◆ Once the base pressure inside the deposition chamber reaches $\sim 10^{-7}$ mbar, it is possible to start the deposition process.
- ◆ The applied power for the SiO₂ and TiO₂ targets are 150 W and 130 W respectively.
- ◆ Now, allow the Argon gas into the deposition chamber which has base pressure $\sim 10^{-7}$ mbar and we have set the working pressure $\sim 5.4 \times 10^{-5}$ mbar.
- ◆ Before the deposition, the targets are exposed to pre-sputtering in order to remove the impurities on the targets. This procedure is followed while preparing all the layers.
- ◆ First, we prepared SiO₂ layer and then the target was changed for TiO₂ layer. We fabricated the first Bragg mirror, which contains certain number of SiO₂ and TiO₂ layers.

- ◆ For the defect layer, we placed the metallic pieces of Erbium on the SiO_2 target and then deposited the layer (this is in the case of NIR microcavity).
- ◆ Fabricate the second Bragg mirror following the same steps as for the first Bragg mirror.

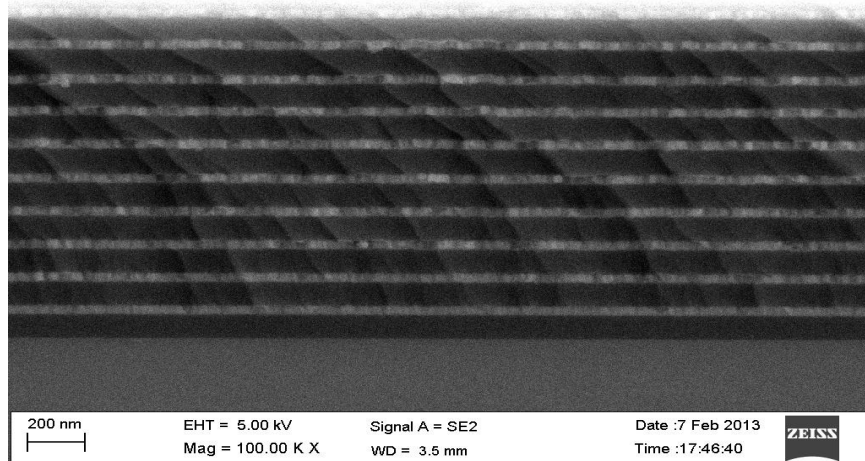


Figure 3.3: FESEM cross sectional image of the one dimensional photonic crystal with 10 bilayers in visible region. The dark regions correspond to SiO_2 layer and lighter regions correspond to TiO_2 layers.

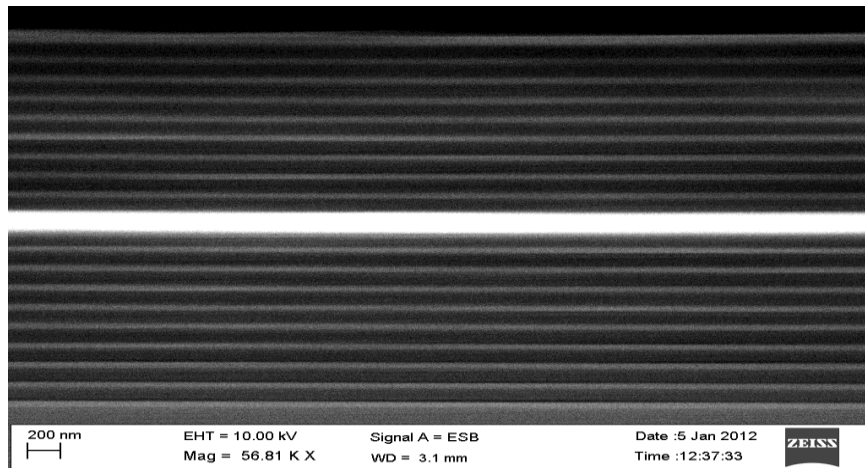


Figure 3.4: FESEM cross sectional image of one dimensional photonic crystal with ZnO defect layer containing 37 layers in visible region. The dark regions correspond to SiO_2 layer and bright regions correspond to TiO_2 layers. The brightest region corresponds to ZnO defect layer.

Figure 3.3 and Figure 3.4 shows the cross sectional images for one dimensional photonic crystal and microcavity in the visible region, which were fabricated using RFMS technique.

Due to the increase of the interest in the area of PBG materials, wavelengths ranging from visible to near infrared [19, 20], it requires an accurate design of the structures [21] and the definition of a flexible experimental protocol that is capable of applicable to different materials and spectral range. The thickness of the processed film during the deposition procedure is monitored by a quartz crystal microbalance (QCM) which is used for monitoring the growth rate during the sputtering [22]. Thickness monitor was calibrated for the two kinds of materials by a long deposition process (24 h of deposition) and by directly measuring the thickness of the deposited layer by an m-line apparatus [6, 23]. The final resolution on the effective thickness obtained by this quartz microbalance is about 4 Å.

3.3 Dispersion Relations

In the present work, we are working with SiO₂ and TiO₂ whose refractive index is 1.46 and 2.3 respectively at 633nm. The band diagram shown in the Figure 3.5 is related to the refractive index contrast values which are given above. Each layer has the same width of $a/2$. In the dispersion diagram, there are two regions called stop band and pass band. If the index contrast between dielectric materials is large enough and if the scattering from a periodic structures interferes constructively, then there are no propagating modes, irrespective of propagation direction within some frequency range is called stop band or PBG.

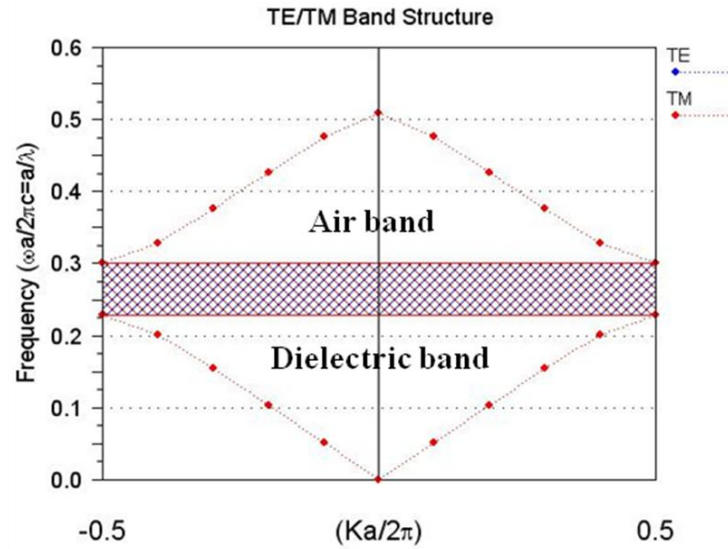


Figure 3.5: The dispersion relation for multilayer films with refractive index contrast (RIC) 1.46:2.24.

These band diagrams were calculated using RSoft's BandSOLVE commercial software, which implements the plane wave expansion method.

On the other hand, destructive interference will allow the light to propagate freely through the periodic material for a band of frequencies; this is called pass band. The low frequency and high frequency band edge of PBG are frequently called the dielectric and air bands, analogous to the valence and conduction bands in solids. Because of the scalability of the Maxwell equations, one can design the PCs operating in the optical regime with micron size or any other regions with corresponding sizes depending on the goal. This can be inferred from the Bragg condition ($\lambda = 2a \sin \theta$, where a width of unit is cell and θ is incident angle).

3.4 Optical properties

The transmission and reflection measurements were carried out using UV-Vis-NIR spectrophotometer (JASCO V-670). In the transmission geometry, a beam with the dimensions $1 \times 6 \text{ mm}^2$ at normal incidence was adopted to measure

the spectrum from 300 nm to 3000 nm, and fixed angle reflection geometry presents the circular beam with diameter of 2 mm for the photonic crystals in visible and NIR regions.

3.4.1 Transmission and reflection measurements

The transmittance spectra at different wavelengths in visible region are shown in Figure 3.6. The spectra were collected at normal incidence and the incident light was unpolarized. Photonic crystals related to spectra 1 and 2, containing 18 layers and that related to spectra 3 contains 20 layers. The spectrum 3 in Figure 3.6 exhibits a broad rejection band ranging from about 530 nm to about 710 nm, the spectrum 2 exhibit rejection band ranging from 550 nm – 750 nm and the spectrum 1 exhibits from 580 nm – 780 nm. The spectra 1 and 2 represent 0.11% minimum transmission band and spectrum 3 shows 0.06% minimum transmission band. All these spectra show around 80% attenuation with the maximum transmission losses at the values where minimum transmission occurs.

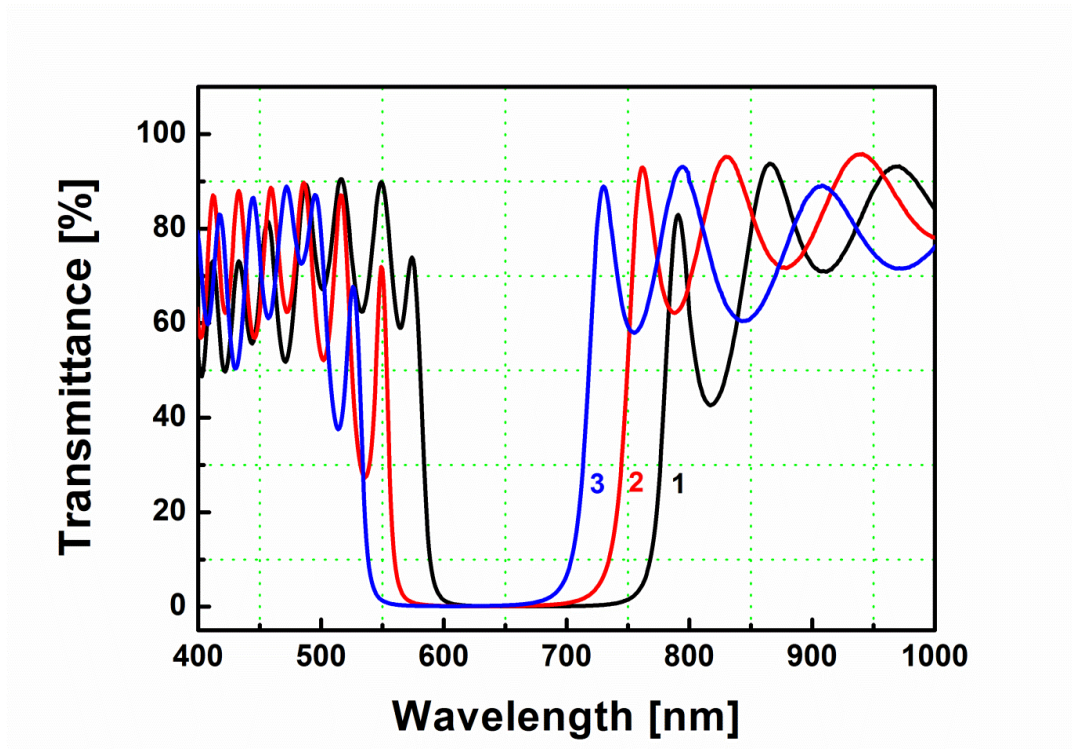


Figure 3.6: The transmission spectra of 1D photonic crystals in visible region. The small oscillations on the either side of the stop band indicate the Fabry-Perot fringes.

Modified Bragg's law for photonic crystals is given by $\lambda = 2d(n_{eff}^2 - \sin^2 \theta)^{1/2}$, where λ is the wavelength at which the transmission is minimum or the reflection is maximum and n_{eff} is effective refractive index, d is the thickness of unit cell and θ is the incident angle. The wavelengths, at which minimum transmission occurs, were calculated using Bragg's law. The calculated values are in good agreement with the experimental values.

Table 3.1: Comparison of experimental values and theoretically calculated values of minimum transmission band for visible region photonic crystals

Spectra related PC	Minimum Transmission band	
	Expt. (nm)	Bragg's law (nm)
Spectrum 1	610 (0.11%)	612
Spectrum 2	634 (0.11%)	637
Spectrum 3	666 (0.06%)	666

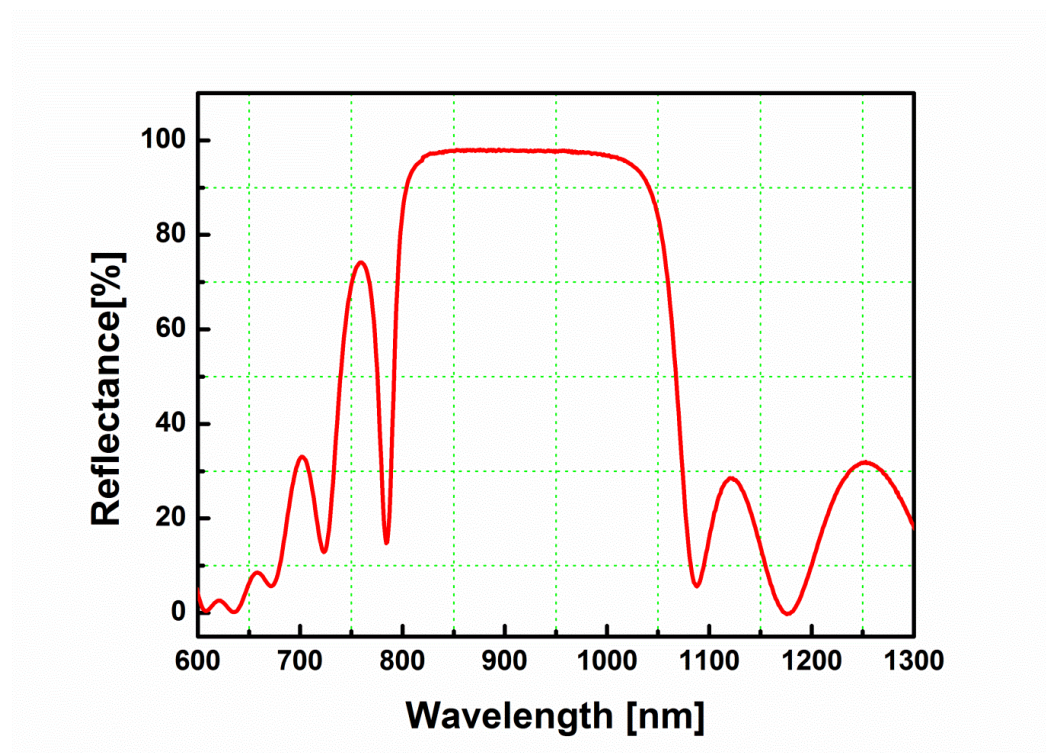


Figure 3.7: Reflection spectra for the photonic crystal in NIR region at normal incidence.

The reflection spectra in NIR region collected at the normal incidence angle is shown in Figure 3.7. The corresponding photonic crystal contains 18 layers with SiO₂ layer thickness of 210 nm and TiO₂ layer thickness of 120 nm. The stop band presents from 780 nm to 1080 nm with FWHM of about 280 nm.

The visible region transmission spectrum of the microcavity is shown in Figure 3.8. The photonic crystal contains 37 layers with ZnO defect layer. The spectra exhibit a broad rejection band ranging from about 535 nm to about 700 nm, and a resonance transmission band peaks at 655 nm, which falls nearly in the middle of the photonic crystal stop band. The transmission peak within the PBG corresponds to the cavity resonance wavelength related to the half wave layer inserted between the two Bragg mirrors.

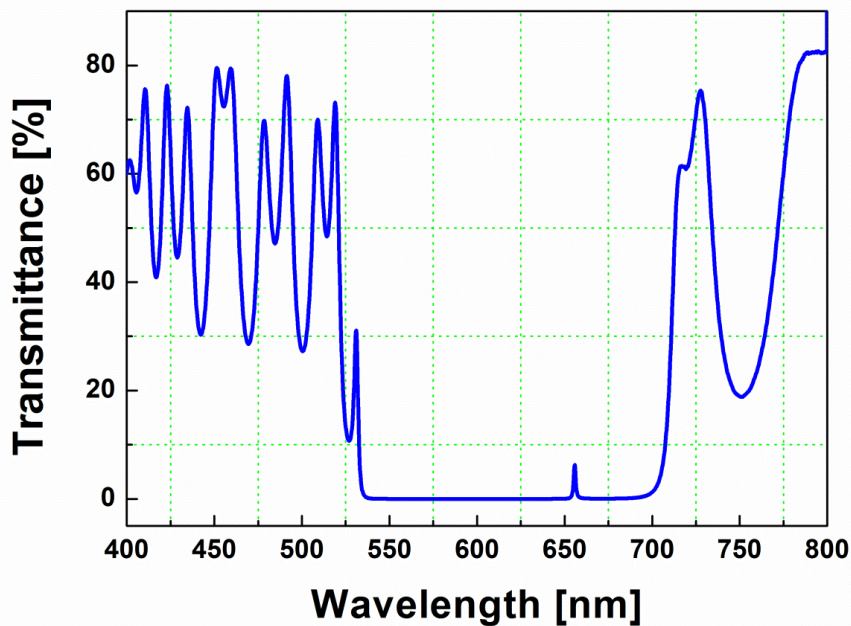


Figure 3.8: The transmittance spectra of one dimensional photonic crystal with defect layer in visible region.

Different parameters, like thickness of the spacer layer, refractive index of the spacer layer and number of periods in each distributed Bragg reflector (DBR) of microcavities will influence on the reflection/transmission spectrum of the microcavity. We could not work on all the above parameters at one stop band region. The detailed report about the above parameters is given in Chapter 1.

3.4.2 Effect of number of layers on stop band

The refractive indices of SiO_2 and TiO_2 at 632 nm are 1.457 and 2.3, respectively. Figure 3.9 displays the experimentally measured transmittance spectra of the photonic crystals consisting of SiO_2 and TiO_2 bilayers with different number of layers N . As N increases, a PBG phenomenon, as indicated by a small transmittance, develops at the designed wavelength. If N becomes large, the stop band appears more prominently. Figure 3.8, shows that a perfect stop band can be obtained in the photonic crystal with 10 bilayers.

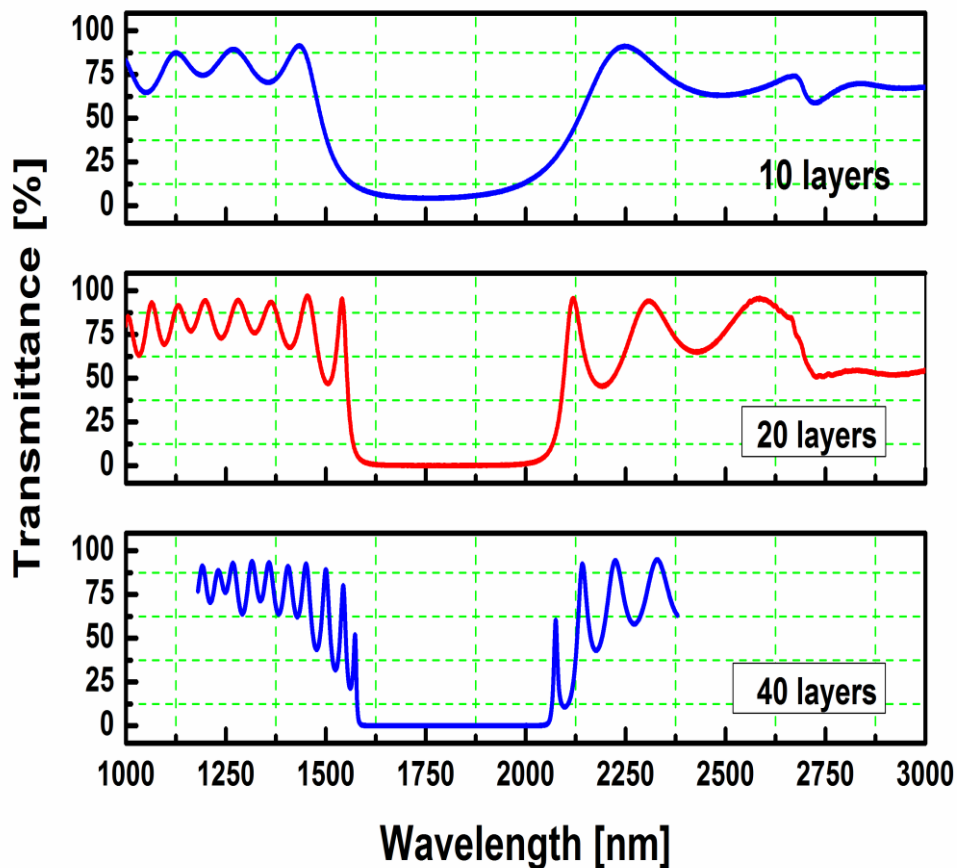


Figure 3.9: Transmittance vs Wavelength for different number layers N with normal incidence, the spectra are in NIR region.

This shows that when N is small, the transmittance in the stop band is large. The transmittance decreases with increasing N. At smaller N's, the transmission in the stop band decreases rapidly. As N increases further, the transmittance tends to be saturated to a small value. As Figure 3.9 shows, nearly zero transmission can almost be achieved when $N > 20$. This means that one may get a perfect stop band in 1D photonic crystals with more than 10 bilayers. This result is consistent with the arguments given above. Before measuring the transmission spectrum, we have measured the thickness of the constituent layers by using the prism coupling technique [18, 23]. The nominal thicknesses of the SiO₂ and TiO₂ layers were 320 nm and 165 nm, respectively.

Table 3.2: *Calculated minimum transmission for different layers*

No. of layers	Stop band(nm)	Min. transmission (%)
10	1440 - 2220	4.2
20	1540 - 2120	0.03
40	1570 - 2070	0.006

The calculated parameters are tabulated above for the photonic crystal containing 40 layers, have the minimum transmission of 0.006% which is very close to zero value. From Figure 3.9, it is clear that,

1. As the number of layers increases, the band edges become sharper and sharper.
2. Also, it can be seen that on the either side of the band gap the Fabry-Perot fringes gets increased as the number of layers increases, which can be attributed to the maximum number of reflections from the interface of the multilayer stack.
3. With increasing number of layers, N, the reflectivity (minimal transmission) increases while the band width (FWHM) of the reflection band decreases.

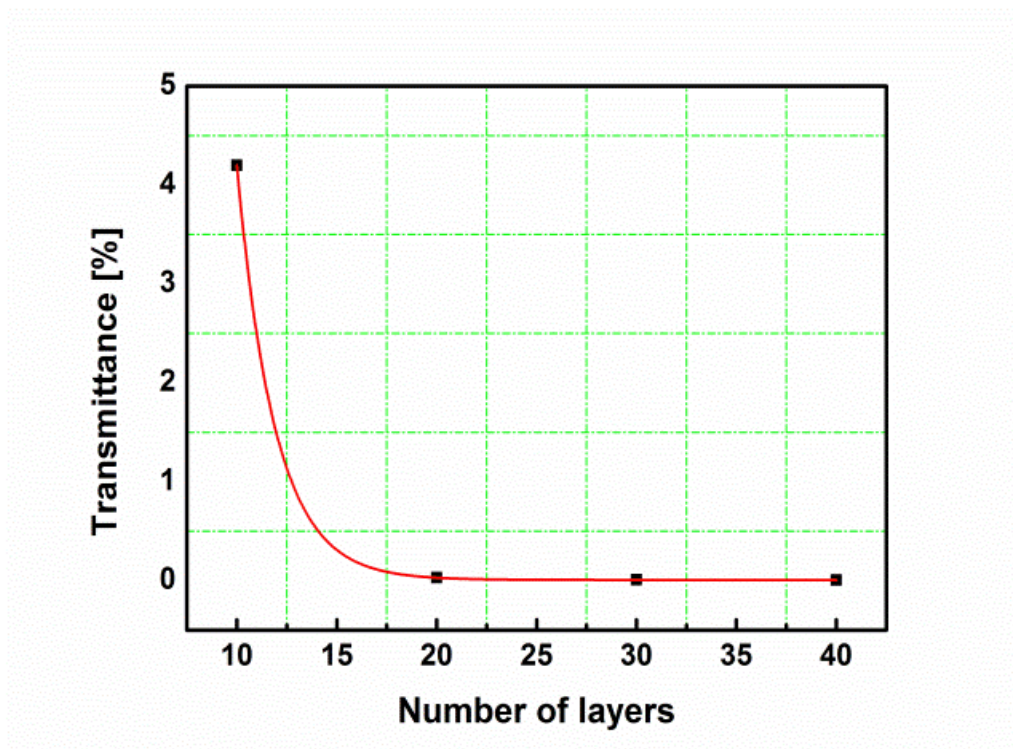


Figure 3.10: plot for transmittance vs. number of layers.

It is clearly indicates from the Figure 3.10 that, the minimum transmission will decrease exponentially as the number of layers increases.

3.4.3 Variable angle reflection measurements

As discussed in chapter 1, the reflectivity of a multilayer structure composed of two different materials with refractive indices n_1 , n_2 depends on the number of layers, N , the refractive index contrast, $n = n_L / n_H$ (assuming $n_L < n_H$), the polarisation of the incident light, the thickness of the individual layers d_L , d_H and the angle of light incidence. The reflectance behaviour of stacks of transparent, dielectric layers with distinct refractive indices results from the interference of light reflected from the different optical interfaces in the stack [14, 16].

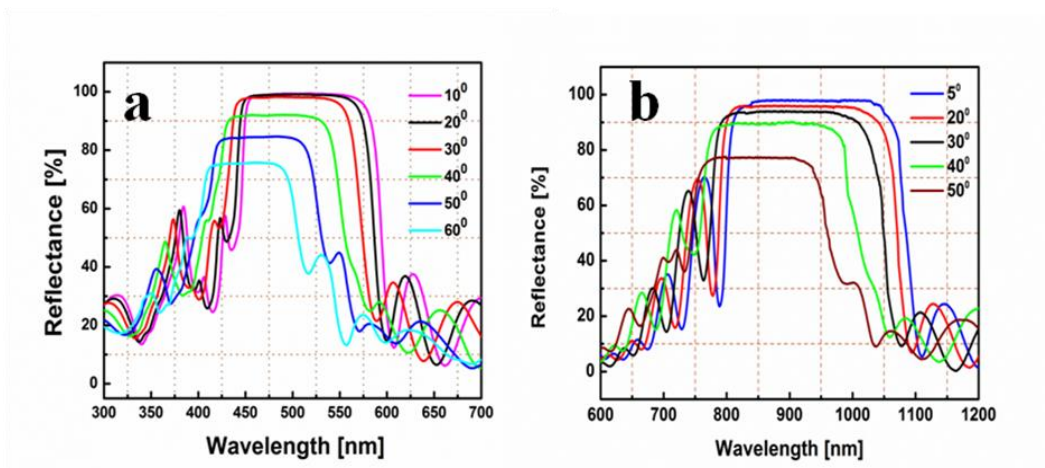


Figure 3.11: Angle resolved transmission spectra of one dimensional photonic crystal in (a) visible and (b) NIR regions. The incident light is unpolarized.

The reflectivity spectra of a 1D photonic crystal at different incidence angles, in visible and NIR regions are shown in Figure 3.11. As the angle of incidence increases, the stop band move towards the shorter wavelengths. In case of visible region photonic crystal, a stop band is obtained between 470 nm to 575 nm with more than 99% reflectance at 10° , with a gap to mid-gap ratio (the ratio of the FWHM of the stop band and the wavelength corresponding to the maximum reflectivity), which characterizes the quality of a stop band [7], of $\lambda / \Delta\lambda = 29.1\%$.

From the Figure 3.12, it is seen that, with the increase of incident angle, the stop band reflectivity decreases. Using modified Bragg's law, for each incident angle, the calculated maximum reflectivity positions match well with the values obtained from experimental results.

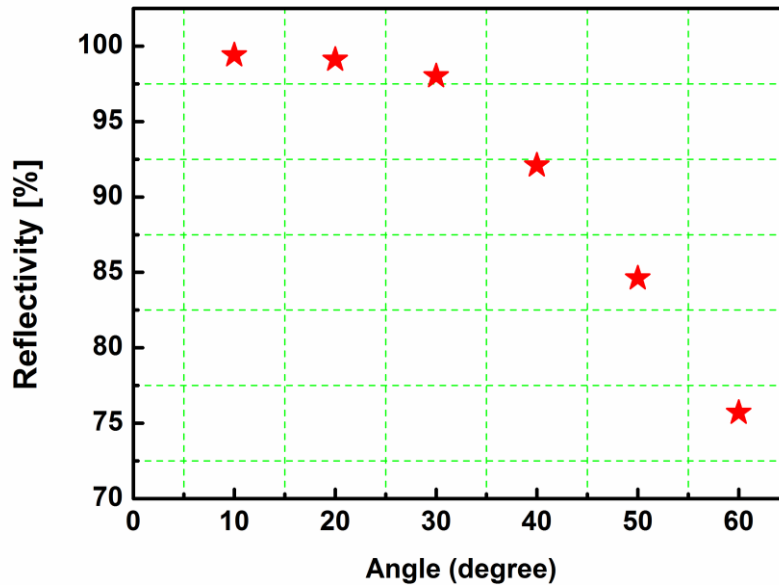


Figure 3.12: Plot shows reflectivity vs. incident angle

Angle resolved reflectance plots for a microcavity in the visible and NIR regions are shown in Figure 3.12. In NIR region, within the broad stop band (its FWHM is 450 nm), a narrow pass band appears at 1703 nm for 20° incidence angle, which corresponds to the resonant optical mode of the cavity defect layer. Similarly, in the visible region, within the broad stop band (its FWHM is 150 nm), narrow pass band appears at 654 nm for 5°, which corresponds to the resonant optical mode of the cavity defect layer.

The resonance behavior of the microcavity is strongly dependent on incident angle. From the Figure 3.13, in the visible and NIR regions, it is shown that with increasing the incident angle, the resonance peak shifts towards the lower wavelengths along with the stop band. The resonance tuning may be useful for modulation of signals.

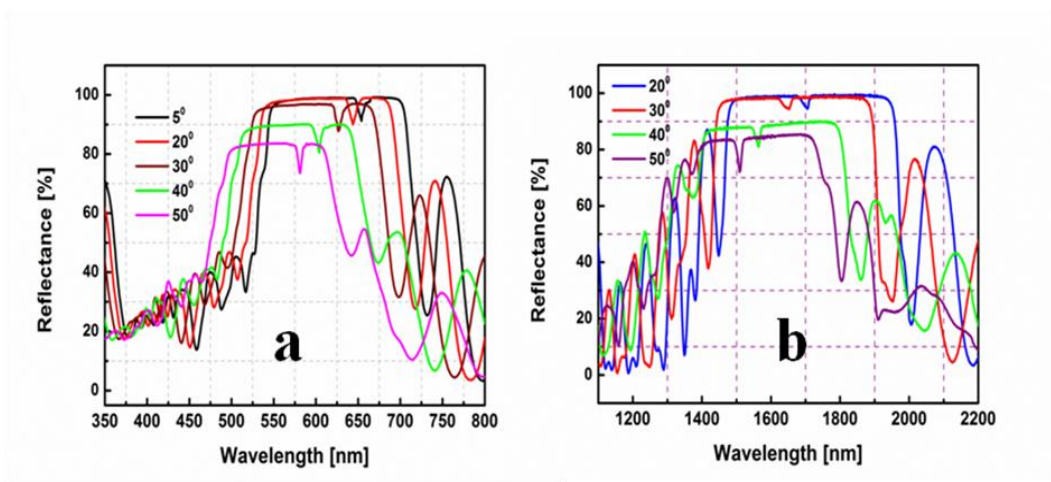


Figure 3.13: Angle resolved transmission spectra of the microcavity in (a) visible and (b) NIR regions. The incident light is unpolarized.

3.4.4 Thickness measurement

1D photonic crystals were prepared using SiO₂, TiO₂ thin films. The Fabry-Perot fringes can be observed on either side of the stop band in both reflection and transmission spectra as shown in Figure 3.8. These oscillations appear due to the interference of light reflected from the different optical interfaces in the multilayer stack. These fringes indicate the homogeneity of thickness and effective refractive index of the photonic crystal within the illuminated area. The experimental results could be comparable with the theoretical data to know the thickness parameters, but calculating them from the analytical expression would be more appropriate in order to determine the quality of the photonic crystals. From the spectral separation of the Fabry-Perot fringes, the thickness of the sample can be quantified. The amplitude of the local reflectance maxima due to Fabry-Perot resonances, will appear at [24]

$$m\lambda = 2hn_{eff} \quad (1)$$

Where m is the resonance order, λ is wavelength, h is the total thickness of photonic crystal and n_{eff} is the effective refractive index of the photonic crystal. Plotting the inverse wavelength as a function of the resonance order, a linear

relation is obtained. In Figure 3.13, the plot shows m vs $1/\lambda$ for the photonic crystal in NIR region. From the slope ($=1/2hn_{eff}$), the thickness of the sample can be calculated. The calculated thickness values for different layers of photonic crystals has been compared with the thickness values obtained with SEM measurements, which is shown in table 3.3. The calculated results are in good agreement with the SEM results.



Figure 3.14: Plot for fringe order m vs $1/\lambda$ for NIR region photonic crystal. Square symbol represents the experimental values and line represents the linear fit based on equation 1.

Table 3.3: Comparison of thickness values obtained with equation 1 and SEM analysis.

photonic crystal Name	No. of Layers	Wavelength region	Total thickness (SEM)	Total thickness (Slope)
PCQ66	20	Visible	2.1 μm	2.3 μm
PCQ08	20	NIR	4.9 μm	5.14 μm
PCQ10	40	NIR	9.8 μm	10.8 μm

3.4.5 Transfer Matrix Method (TMM) for 1D photonic crystals

The transfer matrix method is a method to analyze the propagation of electromagnetic waves through a stratified (layered) medium [25]. This is the most widely used method for the mathematical study of wave transmission in one-dimensional structures because it allows the calculation of reflectivity and transmission spectra [25], emission spectra [26] and guided modes [27].

To study the reflection and the transmission of electromagnetic radiation through a multilayer structure with the TMM method, we consider a one-dimensional structure consisting of alternative layers of different refractive indices coupled to a homogeneous medium characterized by refractive index n_0 at the interface. Figure 3.15 shows this structure, where n_1 and n_2 are the layer's refractive indices, h_1 , h_2 are thicknesses of the respective layers and h ($=h_1+h_2$) is the period of the structure.

plane wave solution can be written as $E = E(x)e^{i(\omega t - \beta z)}$, where the electric field distribution $E(x)$ can be written as

$$E(x) = \begin{cases} A_0 e^{-ik_{mx}(x-x_m)} + B_0 e^{-ik_{mx}(x-x_m)}; x < x_0 \\ A_m e^{-ik_{mx}(x-x_m)} + B_m e^{-ik_{mx}(x-x_m)}; x_{m-1} < x < x_m \\ A_s e^{-ik_{mx}(x-x_{2m})} + B_s e^{-ik_{mx}(x-x_{2m})}; x_{2N} < x \end{cases}$$

where k_{mx} is the x component of the wave vectors $k_{mx} = \omega n_m \cos \theta_m / c$ and θ_m is the ray angle in each layer. A_m and B_m represent the amplitude of the plane waves at interface $x = x_m$ (see Figure 3.14). If the two general amplitudes of $E(x)$ are represented as column vectors, the plane waves at different layers can be related by

$$\begin{pmatrix} A_{m-1} \\ B_{m-1} \end{pmatrix} = D_{m-1}^{-1} D_m \begin{pmatrix} A'_m \\ B'_m \end{pmatrix} = D_{m-1}^{-1} D_m P_m \begin{pmatrix} A_m \\ B_m \end{pmatrix} \quad m = 1, 2, \dots, 2N$$

where matrices D_m are the dynamical matrices given by

$$\begin{cases} \begin{pmatrix} 1 & 1 \\ n_m \cos \theta_m & -n_m \cos \theta_m \end{pmatrix} & \text{for TE wave} \\ \begin{pmatrix} \cos \theta_m & \cos \theta_m \\ n_m & -n_m \end{pmatrix} & \text{for TM wave} \end{cases}$$

and P_m is the propagation matrix, that can be written as

$$P_m = \begin{pmatrix} e^{ik_{mx}h_m} & 0 \\ 0 & e^{-ik_{mx}h_m} \end{pmatrix}$$

The relation between A_0, B_0, A'_s, B'_s can be written as

$$\begin{pmatrix} A_0 \\ B_0 \end{pmatrix} = D_0^{-1} [D_1 P_1 D_1^{-1} D_2 P_2 D_2^{-1}] D_s = \begin{pmatrix} M_{11} & M_{12} \\ M_{21} & M_{22} \end{pmatrix} \begin{pmatrix} A'_s \\ B'_s \end{pmatrix} \quad (\text{a})$$

where N is the number of periods in the structure.

3.4.5.1 Reflectance and Transmittance of the periodic structures

The reflectance and transmittance of monochromatic plane waves through the multilayer structure are calculated from the matrix elements. If the light is incident from medium 0, the reflection and transmission coefficients are defined as

$$r = \left(\frac{B_0}{A_0} \right)_{B_s=0} \quad t = \left(\frac{A_s}{A_0} \right)_{B_s=0} \quad (b)$$

Using the matrix equation (a) and following the definitions in Equation (b), we obtain,

$$r = \frac{M_{21}}{M_{11}}$$

$$t = \frac{1}{M_{11}}$$

Reflectance is given by

$$R = |r|^2 = \left| \frac{M_{21}}{M_{11}} \right|^2$$

If both the bounding media (0, s) are pure dielectric with real n_s and n_0 ,

Transmittance T is given by

$$T = \frac{n_s \cos \theta_s}{n_0 \cos \theta_0} |t|^2 = \frac{n_s \cos \theta_s}{n_0 \cos \theta_0} \left| \frac{1}{M_{11}} \right|^2$$

Figure 3.16 shows transmittance spectra of one dimensional photonic crystal containing 9 bilayers. The solid curve (red colour) represents experimental data and the dotted curve (blue colour) obtained using simulations in the NIR region. The theoretical model for the simulations adopted from the transfer matrix method (TMM) which is explained above. For the experimental data, the

stop band appears from 780nm to 1050nm with corresponding thickness values, $d_H = 90$ nm, $d_L = 185$ nm for TiO_2 , SiO_2 respectively. Thickness values were measured using SEM analysis and the same parameters are used for the simulations.

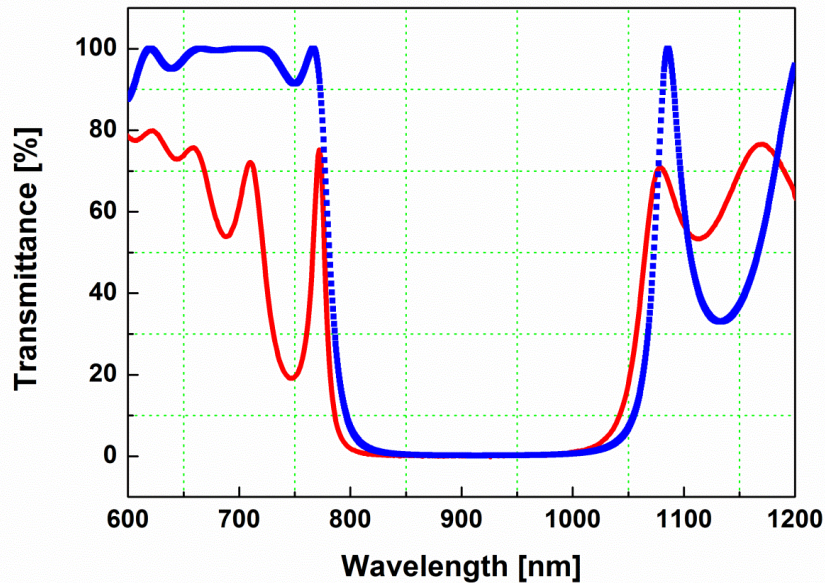


Figure 3.16: Transmission spectra for one dimensional photonic crystal in NIR region. Solid (red) curve represents experimental and dotted (blue) curve represents simulation results.

Although the agreement is satisfactory, there are some discrepancies between the experiment and the simulation. First, the overall value of the transmittance is slightly smaller in the measured spectrum than in the simulated spectrum. This could be attributed to the surface and the interfacial roughnesses of the sample. The surface and the interface of our sample are far better than being optically flat; however, it is still not enough to avoid light scattering completely. The scattering at the interface may reduce the intensity of the transmitted light, lowering the measured transmittance. Second, there are slight mismatches of the locations of stop band and also transmittance maxima and

minima. This may be due to the values of the refractive indices used in the simulation. In the simulation, we used the values, which are measured with m-line spectroscopy using single layer films of SiO₂ and TiO₂. However, the actual refractive indices of the constituent layers could be different from those of the single layers because of the stress and/or strain induced by the lattice mismatch between adjacent layers and the interfacial roughness.

3.4.6 Polarization dependence of spectral characteristics

The polarization dependant spectral characteristics for 1D photonic crystal and microcavity are carried out in reflection geometry using s- and p-polarized light. First we discuss here, about one dimensional photonic crystal with 10 pairs. The FWHM at near normal incidence remains constant irrespective of polarization as well as for the unpolarized light. In case of polarization dependant studies, some interesting features can be observed as shown in Figure 3.17.

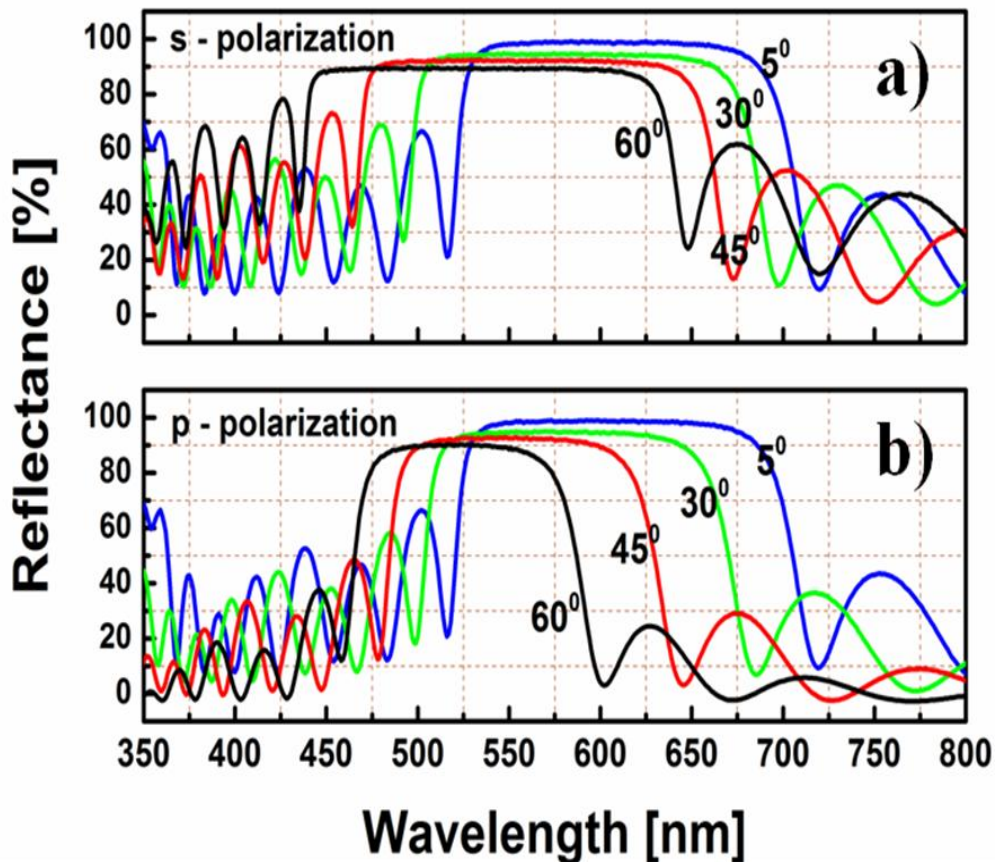


Figure 3.17: Angle resolved reflectance spectra of a 10 pair DBR on silica substrate in visible region, for: (a) s- and (b) p-polarizations.

With increasing angle, the reflection band width increases for the s-polarization, but decreases for the p-polarization, and the central wavelength of the stop band shifts toward shorter wavelength. These observations agree with the theoretical predictions [5]. Whereas, in case of unpolarized light, as the incident angle increases, FWHM decreases slowly. For small enough layer numbers there is a significant difference between s and polarization, and consequently unpolarized light becomes partly polarized upon reflection from a multilayer. The difference between s and p vanishes for a large number of layers in the stack.

The reflectance spectra obtained at $\theta=45^\circ$ and 60° for s- and p- polarized light is shown in Figure 3.18. Here it is clearly evident that the FWHM of

reflection spectra is different for different polarization which is an important property.

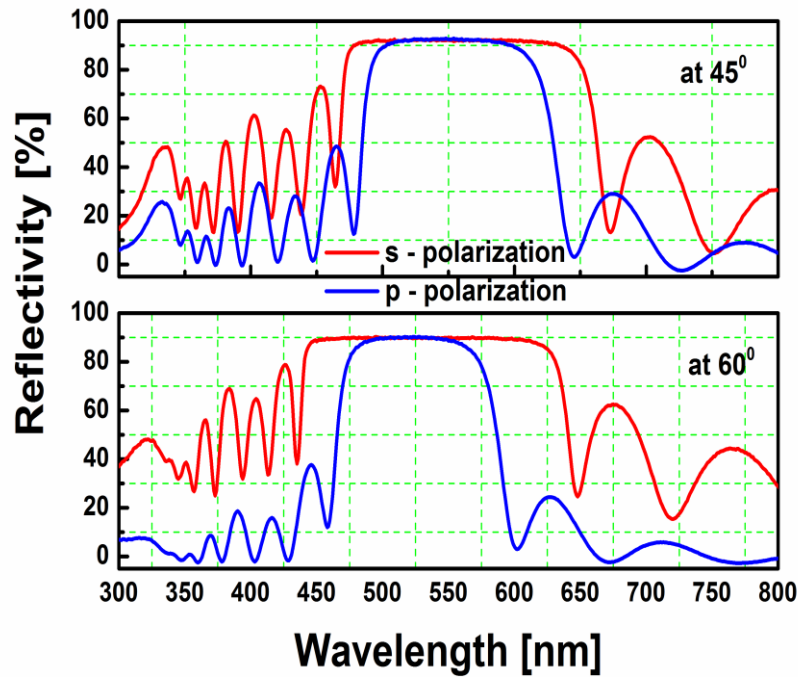


Figure 3.18: Polarization dependence at 45° and 60° in visible region.

The resonance observed in Figure 3.19 is dependent on the incidence angle. The resonance shifts toward shorter wavelength for both polarizations, with increasing angle. However, for s-polarization, the depth of the resonance is gradually reduced with the angle, for p- polarization, it increases.

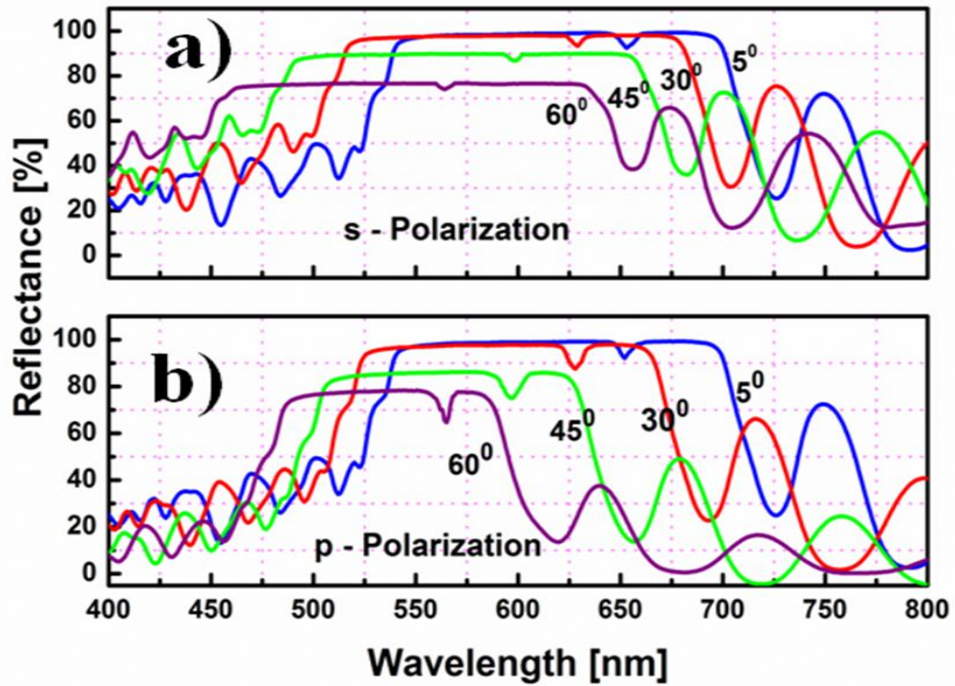


Figure 3.19: Angle resolved reflectance spectra of a microcavity on silica substrate in visible region, for: (a) s- and (b) p-polarizations.

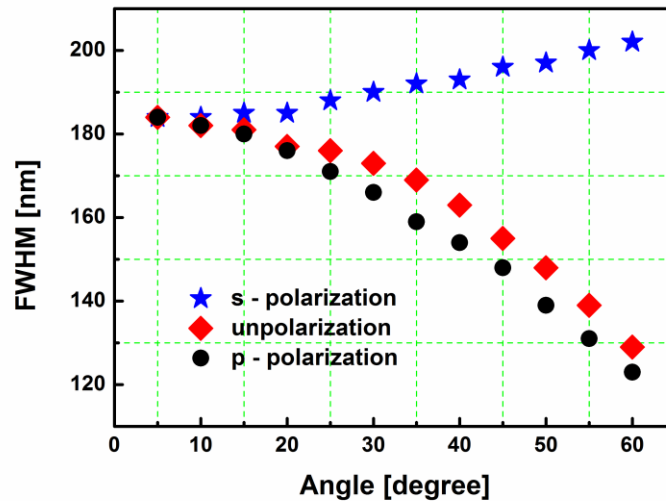


Figure 3.20: Plot shown for FWHM vs internal angle at different polarizations for visible region photonic crystals.

Figure 3.20 represents how the FWHM of multilayer stacks varies with s-, p-polarized and unpolarized light.

3.5 Conclusions

We have successfully fabricated 1D photonic crystals with controlled thickness covering from visible to NIR regions. Transmission and variable angle reflectance measurements were studied. Some of the results were compared with theoretical results based on TMM. Polarization dependant angle resolved reflections measurements were studied on DBR and microcavity in the visible region.

3.6 References

1. N. Tsurumachi, S. Tamashita, N. Muroi, T. Fuji, T. Hattori and H. Nakatusuka, "Enhancement of nonlinear optical effects using one dimensional photonic crystal structures," *Jpn. J. Appl. Phys.* **38**, 6302 (1999).
2. I. L. Lyubchanskii, N. N. Dadoenkova, M. I. Lyubchanskii, E. A. Shapovalov and Th. Rasing, "Magnetic photonic crystals," *J. Phys. D: Appl. Phys.* **36**, R277 (2003).
3. M. Inoue, K. Arai, T. Fujii and M. Abe, "Magneto-optical properties of one-dimensional photonic crystals composed of magnetic and dielectric layers," *J. Appl. Phys.* **83** (11), 6768 (1998).
4. N. Y. Ha, J. W. Wu and B. Park, "Fabrication and optical characterization of 3-D polystyrene colloidal photonic crystal," *J. Korean Phys. Soc.* **45**, 108 (2004).
5. S. Valligatla, A. Chiasera, S. Varas, N. Bazzanella, D. Narayana Rao, G. C. Righini and M. Ferrari, "High quality factor 1-D Er^{3+} - activated dielectric microcavity fabricated by rf sputtering," *Opt. Exp.* **20**, 21214-21222 (2012).
6. A. Chiasera, R. Belli, S. N. B. Bhaktha, A. Chiappini, M. Ferrari, Y. Jestin, E. Moser, G. C. Righini and C. Tosello, "High quality factor Er^{3+} -

- activated dielectric microcavity fabricated by RF sputtering,” *Appl. Phys. Lett.* **89** (17), 171910 (2006).
7. Y. Fink, J. N. Winn, S. H. Fan, C. P. Chen, J. Michel, J. D. Joannopoulos and E. L. Thomas, “A Dielectric Omnidirectional Reflector,” *Science* **282**, 1679 (1998).
 8. J. N. Winn, Y. Fink, S. H. Fan and J. D. Joannopoulos, “Omnidirectional reflection from a one-dimensional photonic crystal,” *Opt. Lett.* **23**, 1573 (1998).
 9. H. Y. Lee and T. Yao, “Design and evaluation of omnidirectional one-dimensional photonic crystals,” *J. Appl. Phys.* **93**, 819 (2003).
 10. I. Abdulhalim, “Omnidirectional reflection from anisotropic periodic dielectric stacks,” *Opt. Commun.* **174**, 43 (2000).
 11. R. St. J. Russell, S. Tredwell and P. J. Roberts, “Full photonic bandgaps and spontaneous emission control in 1D multilayer dielectric structures,” *Opt. Commun.* **160**, 66 (1999).
 12. T. Yonte, J. J. Monzon, A. Felipe and L. L. Sanchez-Soto, “Optimizing omnidirectional reflection by multilayer mirrors,” *J. Opt. A: Pure Appl. Opt.* **6**, 127 (2004).
 13. C. S. Kee, J. E. Kim and H. Y. Park, “Omnidirectional reflection bands of one-dimensional magnetic photonic crystals,” *J. Opt. A: Pure Appl. Opt.* **6**, 1086 (2004).
 14. M. D. Huang, S. Y. Park, Y. P. Lee and K. W. Kim, “Simulation of the Reflectivity of One-Dimensional Photonic Crystals Made of Ti_2O_3 and Al_2O_3 Films,” *J. Korean Phys. Soc.* **47**, 964 (2005).
 15. Y. Li, L. M. Fortes, A. Chiappini, M. Ferrari and R. M. Almeida, “High quality factor Er-doped Fabry–Perot microcavities by sol–gel processing,” *J. Phys. D: Appl. Phys.* **42**, 205104 (2009).
 16. R. M. Almeida, A. S. Rodrigues, “Photonic bandgap materials and structures by sol–gel processing,” *J. Non-Cryst. Solids* **326&327**, 405–409 (2003).

17. S. Rabaste, J. C. Plenet, J. Dumas, J. Bellessa, J. Mugnier, O. Marty, “Eu³⁺-doped microcavities fabricated by sol–gel process,” *Appl. Phys. Lett.* **79**, 14 (2001).
18. L. Persano, P. Del Carro, E. Mele, R. Cingolani, D. Pisignano, M. Zavelani-Rossi, S. Longhi, G. Lanzani, “Monolithic polymer microcavity lasers with on top evaporated dielectric mirrors,” *Appl. Phys. Lett.* **88**, 121110 (2006).
19. C. M. Johnson, P. J. Reece and G. J. Conibeer, “Slow light enhanced up conversion for photovoltaic applications in one dimensional photonic crystals,” *Opt. Lett.* **36** (20), 3990–3992 (2011).
20. Y. Li and R. M. Almeida, “Photoluminescence from a Tb-doped photonic crystal microcavity for white light generation,” *J. Phys. D*, **43** (45), 455101 (2010).
21. Y. G. Boucher, A. Chiasera, M. Ferrari and G. C. Righini, “Photoluminescence spectra of an optically pumped erbium-doped microcavity with SiO₂/TiO₂ distributed Bragg reflectors,” *J. Lumin.* **129** (12), 1989–1993 (2009).
22. A. Wajid, “On the accuracy of the quartz-crystal microbalance (QCM) in thin film depositions,” *Sens. Actuators A Phys.* **63** (1), 41–46 (1997).
23. S. J. L. Ribeiro, Y. Messaddeq, R. R. Gonçalves, M. Ferrari, M. Montagna and M. A. Aegerter, “Low optical loss planar waveguides prepared by an organic-inorganic hybrid system,” *Appl. Phys. Lett.* **77** (22), 3502–3504 (2000).
24. Max Born, Emil Wolf, “*Principles of Optics*” 7th edition.
25. P. Yeh, “*Optical waves in layered media*” (Wiley-Interscience, 2005).
26. Y. G. Boucher, A. Chiasera, M. Ferrari, G. C. Righini, “Extended transfer matrix modeling of an erbium-doped cavity with SiO₂/TiO₂ Bragg reflectors,” *Opt. Mat.* **31**, 1306–1309 (2009).
27. H. Taniyama, H. Taniyama, “Waveguide structures using one-dimensional photonic crystal,” *J. Appl. Phys.* **91**, 3511 (2002).

Chapter 4

High Quality factor Er³⁺ - activated dielectric microcavity

Abstract:

Rare earth-activated 1D photonic crystals were fabricated by RF-sputtering technique. The Bragg reflector consists of twenty SiO₂/TiO₂ bilayers, designed with a stop band in the near infrared region. The cavity is constituted of an Er³⁺ doped SiO₂ active layer inserted between two such Bragg reflectors. Scanning electron microscopy is employed to put in evidence the quality of the sample, the homogeneities of the layers thickness and the good adhesion among them. Near infrared (NIR) transmittance and variable angle reflectance spectra confirm the presence of a stop band from 1500 nm to 2000 nm with a cavity resonance centered at 1749 nm at 0° and a quality factor of 890. The influence of the cavity on the ⁴I_{13/2}→⁴I_{15/2} emission band of Er³⁺ ion is also demonstrated.

4.1 Introduction

Photonic crystals are periodic dielectric structures, possessing photonic band gaps [PBG]: the frequency range in which light cannot propagate through the structure [1- 3]. As mentioned in Chapter 1, an important application of PBGs is made possible by the controlled introduction of defects, along which light may propagate within the stop band, in a manner similar to the impurity levels of doped semiconductors. Fabry–Perot microcavity is an example for a 1D structure [4 - 7], which may be achieved by the introduction of an extra layer or the suppression of a layer, within a multilayer stack as is seen in Figure 4.1. The microcavity has the resonance mode within the stop band of the same structure. The reflectance minimum corresponding to the microcavity resonance inside the stop band appears at $\lambda=2nd$. The quality factor (Q) of a microcavity is given by:

$$Q = \frac{\lambda}{\Delta\lambda} \quad (4.1)$$

where λ is resonance wavelength and $\Delta\lambda$ is full width half maximum (FWHM).

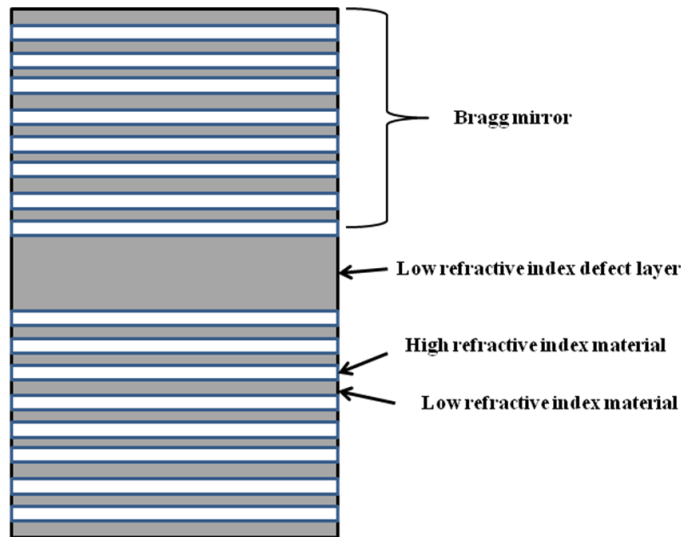


Figure 4.1: Schematic view of 1D microcavity with Bragg mirrors on either side of a low refractive index defective layer.

The recent developments of optically confined structures have opened new possibilities in the field of both basic and applied physics, in a large area covering communication, health, biology, energy and environment monitoring technologies [8 - 10]. On this scenario, rare earth-activated glasses have become one of the key materials in photonic systems because of their relevance for the development of optical amplifiers [11] and effort was directed to develop appropriate material systems and configurations to exploit at the best the luminescence properties of rare earth ions like Er^{3+} [12, 13]. The last decade has seen a remarkable increase in the experimental efforts to control and enhance the emission properties of emitters by tailoring the dielectric surrounding of the source [8, 12 - 14]. With this aim, several approaches, using nanocomposite materials or specific geometries, such as planar interfaces, photonic crystals, solid state planar microcavities, dielectric nanospheres and spherical microresonators have been proposed. Among these systems, planar microcavity resonators, also called one dimensional (1D) photonic crystals, are the simplest photonic bandgap (PBG) device exploitable to manage the spectroscopic properties of luminescent species such as rare earth ions [15 - 17] and quantum dots [18].

Oxide based dielectric materials are particularly suitable for fabricating PBG structures because they have wide transparency from the ultraviolet to the NIR. Furthermore, oxide based dielectric materials have good resistance to temperature, corrosion and radiation as well [19 - 21]. Various techniques have been employed to fabricate Fabry-Pérot dielectric microcavities where reproducible deposition of thin dielectric layers, that constitute distributed Bragg reflectors (DBRs) are mandatory to achieve a high quality factor (Q). Processes like ion implanting [15], sol-gel [17, 18], electron-beam evaporation [22] and sputtering [16, 20] can be successfully employed for the fabrication of microcavities based on oxide dielectric materials. However, to reach high Q factor using dielectric material, where the refractive index difference between the different materials is not as high as for the semiconductors. The real time control of the deposition process is mandatory to allow a precise tailoring of the deposition rate and obtain good uniformity in thickness. Moreover, an increasing

interest in shifting the rejected wavelengths in different zones ranging from visible to NIR [12, 21], requires an accurate design of the structures [23] and the definition of flexible experimental protocol capable to adapt itself to different materials and spectral range. A possible way to monitor the thicknesses of the processed film during the deposition procedure is represented by the quartz crystal microbalance (QCM) which could be used for monitoring the growth rate in physical vapor deposition and sputtering processes [24]. Sputtering methods are widely used in industrial process because high quality films can be obtained at low temperature substrates [25]. We have also demonstrated as the rf sputtering is a suitable technique for fabrication of dielectric microcavities and it is a cheap and versatile technique to deposit alternating layers of different materials with controlled refractive index and thickness [16]. With these advantages, as well as the possibility to incorporating QCM, rf sputtering process is an extremely appropriate candidate to fabricate high quality and homogeneous 1D photonic crystals.

In this chapter, we discuss a reproducible fabrication protocol based on rf-sputtering technique and optical, spectroscopic and morphological characterization of the realized high quality Er³⁺- activated dielectric microcavity consisting of alternating silica and titania films. A radical improvement of the fabrication and diagnostic methodologies are reported, leading to novel quantitative and qualitative results in terms of quality factor, morphology, and extended spectroscopic functionalities of the microcavity.

4.2 Experimental

Erbium doped dielectric microcavity is composed of alternating high and low refractive index dielectric layers, SiO₂ and TiO₂ respectively, with an optical thickness of $\lambda/4$ ($\lambda=1.749 \mu\text{m}$) [8, 9]. SiO₂/TiO₂ one dimensional photonic crystals with SiO₂ doped Er³⁺ defect layer was prepared by multi target rf sputtering technique [9]. The samples were deposited on silicon and v-SiO₂ substrates. The substrates were cleaned inside the rf sputtering deposition

chamber by heating at 120 °C for 30 min just before the deposition procedure. As a first step, Bragg mirrors were prepared. The Bragg mirrors formed by a stack of quarter wave layers of SiO₂ and TiO₂. In the pre-sputtering stage the face of the substrates is exposed to the plasma for 10 min. The residual pressure, before the deposition, was about 1.1x10⁻⁶ mbar.

During the deposition process, the substrates were not heated and the temperature of the sample holder during the deposition was 30 °C. The sputtering occurred with an Ar gas pressure of 5.4x10⁻³ mbar; the applied rf power was 150 W and 130 W and the reflected powers 0 W for silica and titania targets, respectively. Sputtering deposition of the films was performed by sputtering alternatively with 15x5 cm² titania target and a 15x5 cm² silica target. For the defect layer a 15x5 cm² silica target, on which metallic Erbium pieces were placed, was employed. The deposition time, necessary to reach the appropriate thickness of the Bragg mirror layers was 2 h 30 min for titania target and 1 h 20 min for silica target. The deposition time necessary to reach the appropriate thickness of the silica defect layer, to obtain cavity resonance centred at 1.749 μm, was 2 h 40 min.

Particular attention was paid to the reproducibility of the single layers. To monitor the thickness of the layers during the deposition, two quartz microbalances Veeco instruments thickness monitor model QM 311, faced on the two targets were employed. Thickness monitor was calibrated for the two kinds of materials by a long deposition process (24 h of deposition) and by directly measuring the thickness of the deposited layer by an m-line apparatus [16, 26]. The final resolution on the effective thickness obtained by this quartz microbalance is about 4 Å.

The compositional analysis was performed using energy dispersive spectroscopy (EDS), employing an Oxford model INCA PentaFETx3 apparatus. EDS measurement was employed in particular to quantify the Erbium content in the active layer. Scanning electron microscopy (SEM) was used to analyze the morphology of the multi layer films and thickness of each layer. The cross

section of the microcavity was analyzed by a FEG model JEOL JSM-7001F apparatus at 15 kV after covering the films with a 20 nm gold layer.

The transmittance and reflectance spectra in the NIR region of the sample was obtained by using a double beam Varian - Cary spectrophotometer with a resolution of 0.1 nm. The reflectance is also performed at different angles of incident light, in order to check the evolution of the photonic bandgap with the direction of the incident light. An evaporated aluminum mirror is used as the background for the reflectance measurements.

Photoluminescence (PL) spectroscopy was performed using the 514.5 nm line of an Ar⁺ ion laser as excitation source. The luminescence was dispersed by a 320 mm single-grating monochromator with a resolution of 1 nm. The light was detected with the help of a Hamamatsu photomultiplier tube and standard lock-in technique. More details about the experimental setup can be found in Chapter 2 and also from the reference [16]. In fact, the excitation angle must be chosen in order that not entire laser beam is reflected by the DBRs, and a part of the excitation light reaches the active defect layer. The angle of collection of luminescence is chosen in order to superimpose the cavity resonance to the Er³⁺ emission.

Schematic diagram of the excitation and detection geometries employed for a reliable assessment of the influence of the cavity on 1.5 μm emission band of Er³⁺ ion is shown in Figure 4.2 (a & b). The sample is fixed on a rotation stage in order to obtain the best angle resolution. In order to compare the emission from active ions in the microcavity and also the reference sample, we have used the same geometry for both the samples.

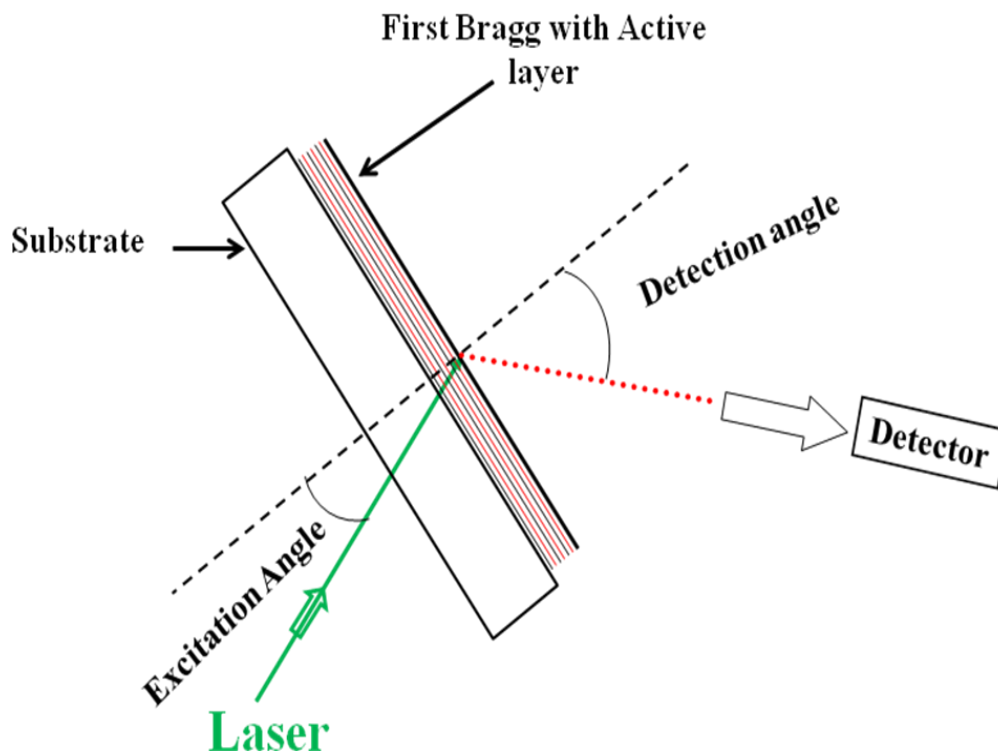


Figure 4.2 (a): configuration employed for the Er^{3+} -activated reference sample.

The effectiveness of a dielectric microcavity is determined by its Q-factor, in particular for active systems, where the luminescence features are crucial. To allow a direct comparison of the Er^{3+} luminescence intensity between the photonic crystal and the single active layer, a reference sample was fabricated. The reference sample was deposited on SiO_2 substrate during the same deposition run for the fabrication of the photonic crystal. It was therefore obtained employing the same fabrication protocol and targets used for the photonic crystal and so the layers that constitute the samples exhibit the same thickness and composition. Thus, in the reference sample the second Bragg reflector that should be placed above the active layer, is not present. In this way the luminescence from the reference sample can be emitted without any cavity effect but the excitation laser light that will come from the substrate through the Bragg mirror toward the active layer will be affected by the presence of the multilayer structure in the same way for the both photonic crystal and reference samples.

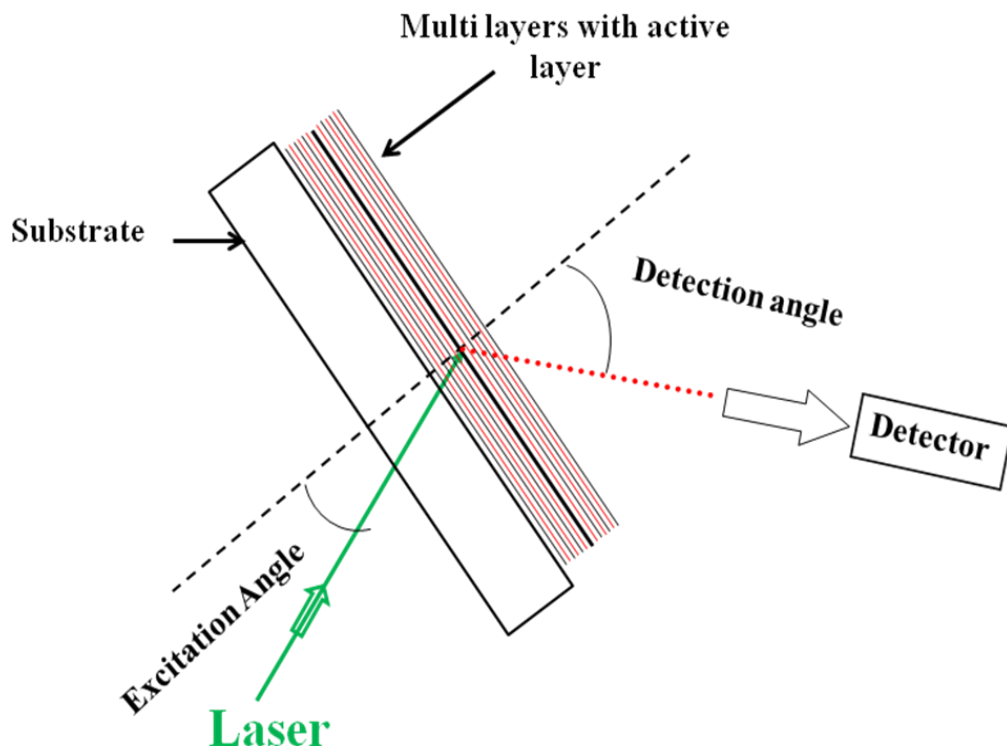


Figure 4.2 (b): configuration employed for the Er^{3+} - activated 1D microcavity.

As a result, the total amount of excitation laser light that reaches the active layer is the same for both the samples, as far the experimental conditions allow. Photoluminescence measurements were performed paying particular attention to the excitation and detection angles and the experimental condition adopted for the photonic crystal and reference sample was, as far as possible, the same. Figure 4.2 (a) and 4.2 (b) show the schematics of the excitation and detection geometries employed for the Er^{3+} -activated reference sample and the 1D cavity, respectively.

4.3 Results and Discussions

4.3.1 Structural and Optical properties of first Bragg mirror

Figure 4.3 shows the SEM cross sectional image of the first Bragg mirror. The Bragg mirror is constituted of ten SiO_2/TiO_2 doublets making the total number of layers stacked to fabricate this mirror to 20. The thickness of each of

the SiO₂ and TiO₂ layers measured on the image is about 325 ± 5 nm and 175 ± 5 nm respectively. From Figure 4.3, for both the materials the thickness fluctuation from one layer to the other is estimated at not more than ± 5 nm. The time period of the sputtering is optimized over several samples in order to obtain the

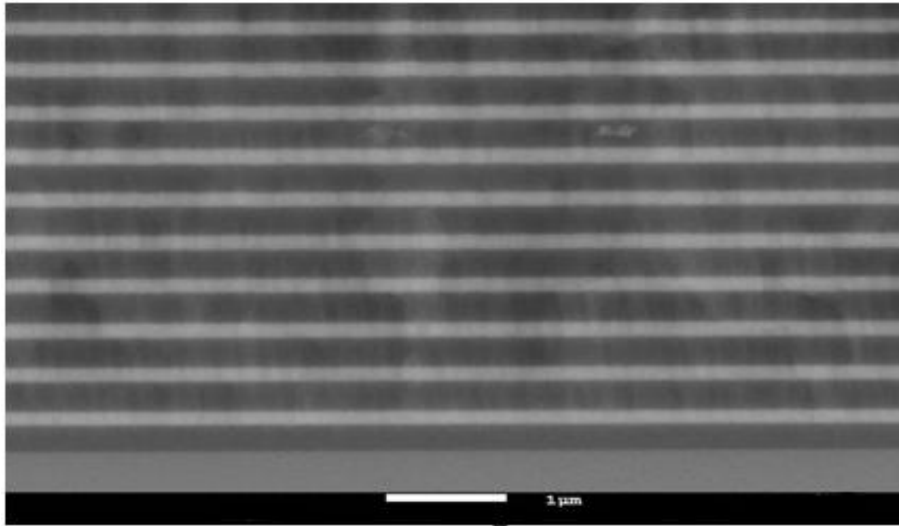


Figure 4.3: Cross sectional image of the Bragg mirror obtained with the SEM showing 20 layers, 10 each of SiO₂ and TiO₂ deposited on Si substrate. The scale bar is of one micron.

stop band centered at the $1.75 \mu\text{m}$ region, which is of current interest. SiO₂ target, having a higher sputtering yield is sputtered for 1 h 20 min and TiO₂ with a lower sputtering yield is sputtered for 2 h 30 min. The samples are found to be comparatively thicker and uniform at the centre (in an area of about 1 cm^2) and gradually thin down towards the edges, as the plasma is concentrated at the centre during the deposition process. Hence care is taken to perform all the characterization nearer to the centre of the sample.

The transmission spectrum of the first Bragg mirror performed using the Cary – Varian 5000 spectrophotometer is shown in the Figure 4.4. The ultra-low transmission band lies from about 1480 nm to 1950 nm with a 0.01 % minimum transmission through most parts of the stop band. The 470 nm wide stop band is

centred at 1725 nm which coincides with the $Er^{3+} \ ^4I_{13/2} \rightarrow \ ^4I_{15/2}$ emission peak at higher angles.

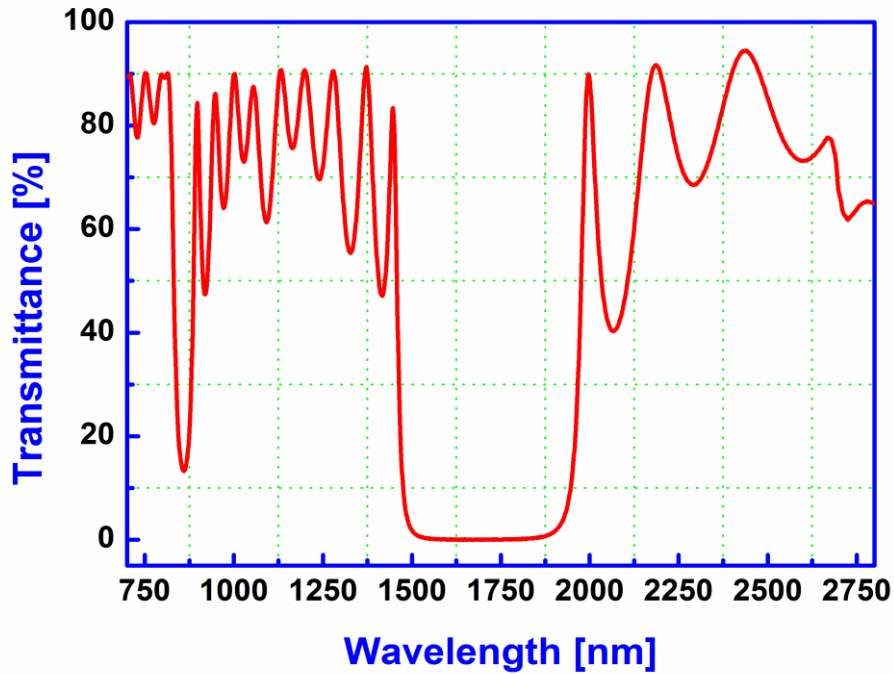


Figure 4.4: Transmission spectrum of the Bragg mirror with 10 doublet layers. The reflection window of the mirror lies from 1480 nm to 1950 nm.

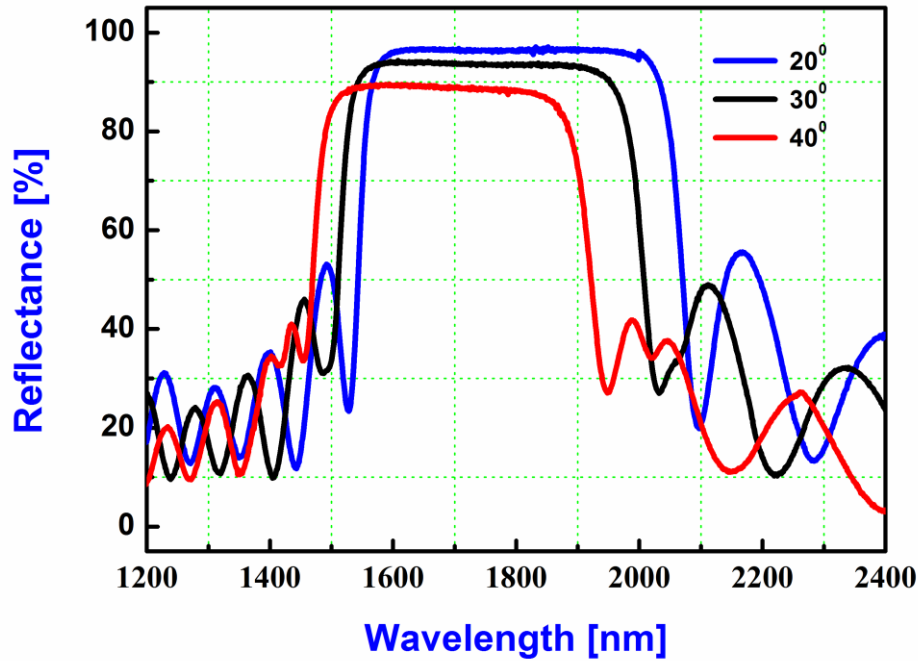


Figure 4.5: Reflectance spectra collected for the Bragg mirror containing 10 doublets using a variable angle reflection measurement system at 20°, 30° and 40° angle of incidence.

The angle dependent reflectance plots for the Bragg mirror at 20°, 30° and 40° angle of incidence using a variable angle reflection measurement system are shown in Figure 4.5. A gap to mid-gap ratio (the ratio of the FWHM of the stop band and the wavelength corresponding to the maximum reflectivity), which characterizes the quality of a stop band of $\Delta\lambda/\lambda_{max} = 523 \text{ nm}/1707 \text{ nm} = 30.6 \%$ is obtained at 20° of incidence. Similar values are obtained at 30 and 40 degrees of incidence too.

The dependence of the quality of the Bragg mirror on the number of alternating layers is seen in Figure 4.6. The film with 5 bilayers has a low transmission of about 4.3 % at the stop band. But, the film with 10 bilayers has a lower transmission of 0.02 % at the stop band with sharp band edges. The number of bilayers has hence bettered the optical transmission properties of the

Bragg mirror. However, with the increasing number of layers there exists a possibility of cracks being developed in the film due to internal stress.

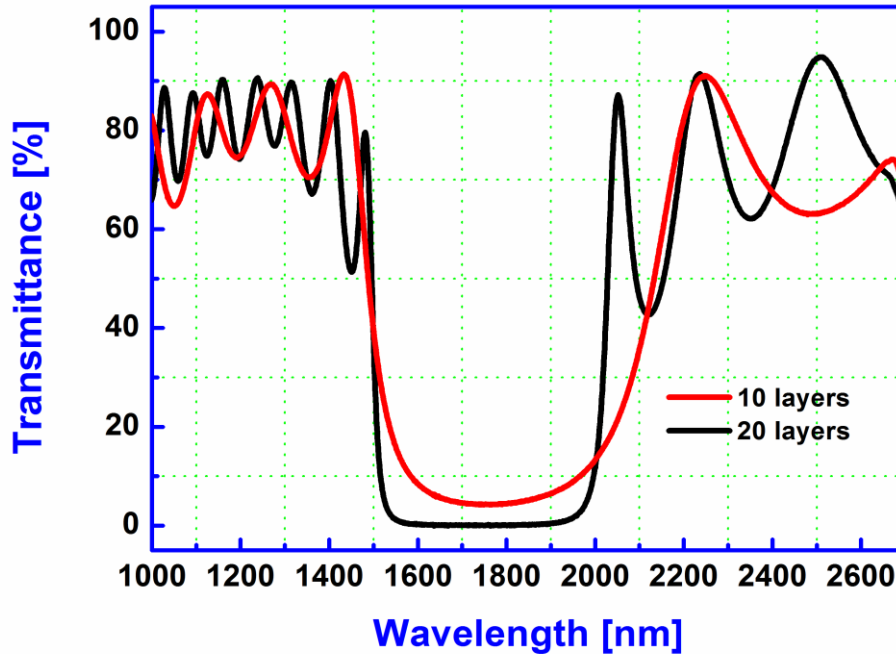


Figure 4.6: Comparative study of transmission spectra of Bragg mirrors with 5 and 10 bilayers. The sample with 10 bilayers is observed to have lower transmission in the stop band and sharp band edges.

4.3.2 Structural and Optical properties of microcavity

The cavity is constituted by an Er^{3+} - doped SiO_2 active layer inserted between two Bragg reflectors, each one consisting of ten pairs of SiO_2/TiO_2 layers. SEM images of the cross section of the 1D microcavity are shown in the Figure 4.7 (a) and 4.7 (b). The central $\lambda/2$ layer corresponds to the SiO_2 doped Er^{3+} active layer. The dark regions correspond to the SiO_2 layer and the bright regions correspond to the TiO_2 layer. The substrate is located at the bottom of the images and the air on the top. It is possible to identify the defect layer and the two Bragg reflectors. The SEM analysis allows to measure the thickness for the

Bragg mirrors of 320 ± 5 nm and 170 ± 5 nm for the silica and titania layers, respectively, and a thickness of 625 ± 5 nm for the Er^{3+} - doped SiO_2 active layer.

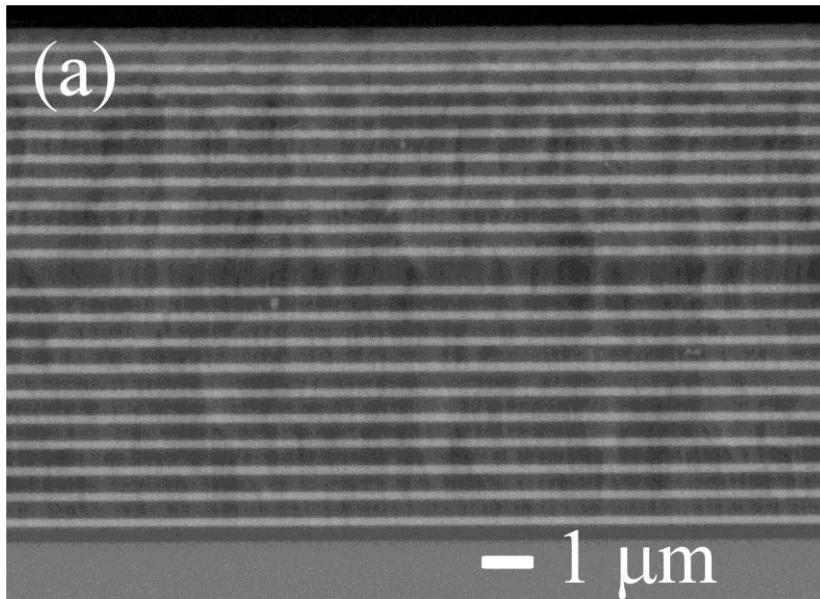


Figure 4.7(a): Image for a length of the sample of about 16 μm

From Figure 4.7 (b) it is possible to note how the deposition technique allows us having a good uniformity of the thickness as well as a perfect adhesion of the films on extent of the order of tens of micrometers in length. EDS measurements indicate that the Erbium content in the active layer is about 0.6 ± 0.1 mol%. A uniform thickness over a large area and, a low layer to layer thickness variation has been observed.

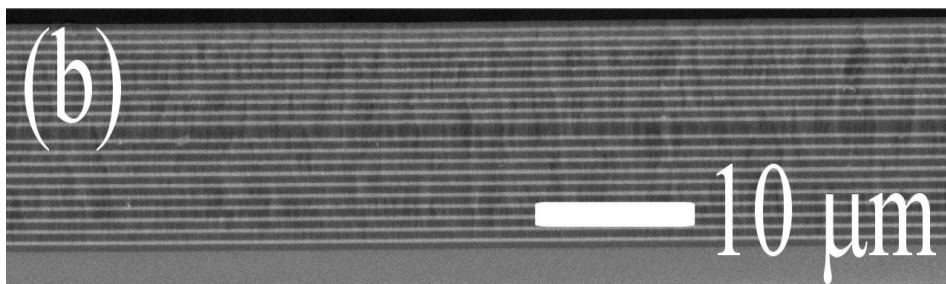


Figure 4.7(b): Image for a length of the sample of about 60 μm.

The NIR transmission spectrum for the microcavity is shown in Figures 4.8 and 4.9. The transmittance spectra were measured at zero degree of incident angle. In Figure 4.8 it is possible to note that as the spectral reflectance range, i.e. the stop band, ranges from 1490 nm to 1980 nm. A sharp peak in the transmittance spectrum appears at 1749 nm. It corresponds to the cavity resonance wavelength related to the half wave layer inserted between the two Bragg mirrors.

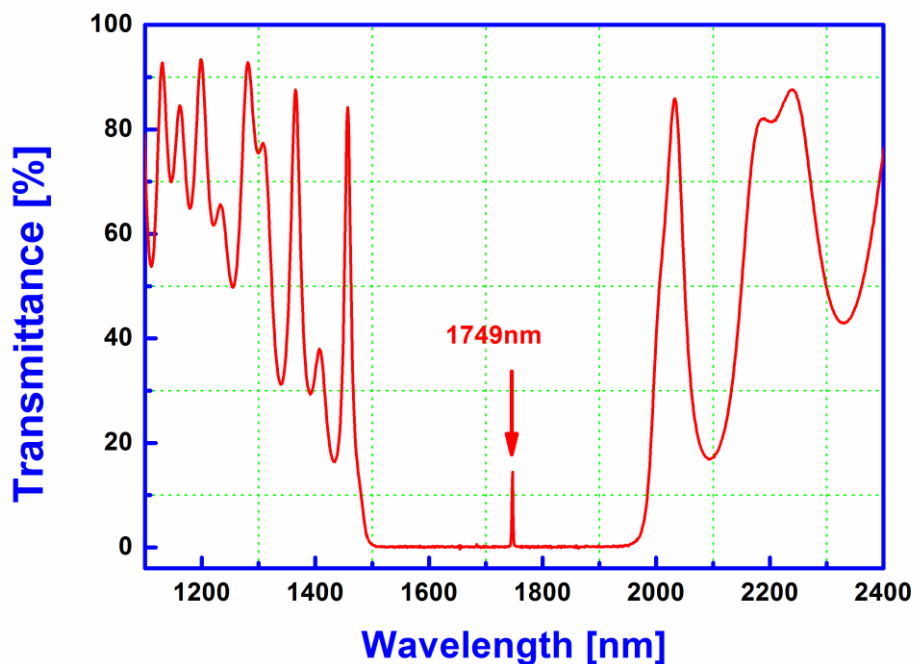


Figure 4.8: Transmission spectrum of the microcavity with twenty doublets Bragg mirror. The reflection windows of the mirrors lie from about 1490 nm to 1980 nm. The cavity resonance corresponds to the sharp maximum at 1749 nm, at the centre of the stop band.

The transmittance spectrum in Figure 4.9, obtained with a resolution of 0.1 nm, shows the sharp resonance line. The full width at half maximum (FWHM), calculated by a fit with a Gaussian curve, is 1.97 nm, corresponding to a Q factor of the cavity (Q), of about 890, according to the equation 4.1.

This value is one of the highest Q factor obtained so far for Erbium activated SiO₂ - TiO₂ system at 1.5 μm.

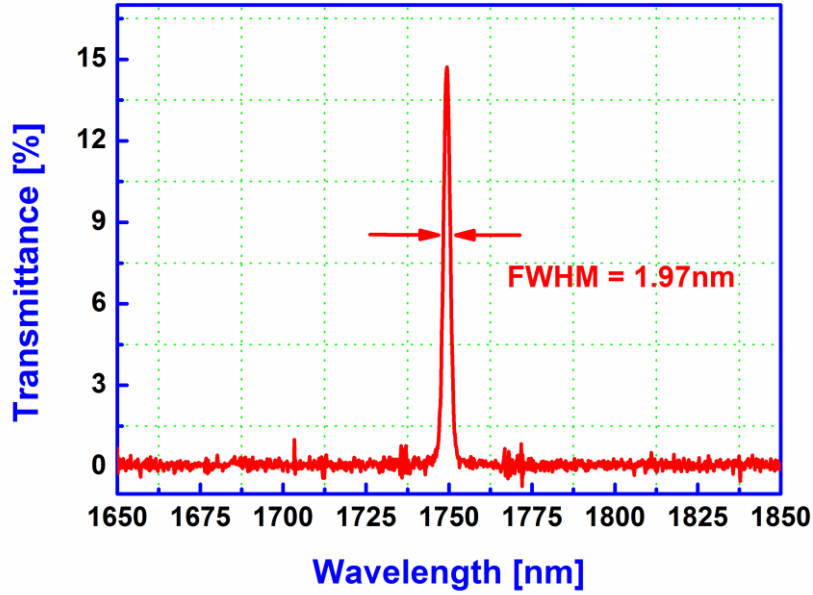


Figure 4.9: Spatially resolved transmission measurement of the cavity resonance. The line width of the resonance is 1.97 nm resulting in a cavity Q factor of 890.

Figure 4.10 shows the angle dependent Bragg reflection for the sample with a dip due to the cavity centered at 1708 nm for 20° angle of incidence. As the angle increases, the stop band shifts linearly to shorter wavelengths as observed with the Bragg mirror [7]. This is in accordance with Bragg's law [27],

$$\lambda = 2d(n_{eff}^2 - \sin^2 \theta)^{1/2} \quad (4.2)$$

where, λ is the free-space wavelength of light, d is the period ($= h_1+h_2$) of the PC, n_{eff} is the effective refractive index which can be calculated from the formula

$$n_{eff} = \frac{(n_{TiO_2} d_{TiO_2} + n_{SiO_2} d_{SiO_2})}{d_{SiO_2} + d_{TiO_2}}$$

Here, n_{TiO_2} is Refractive Index (RI) of TiO_2 thin film and n_{SiO_2} is the RI of SiO_2 thin film; d_{SiO_2} is the thickness of SiO_2 thin film and d_{TiO_2} is the thickness of TiO_2 thin film and θ is the angle of incidence. Considering $n_{eff} = 1.82$, and the position of the dip (λ) in Figure 4.10 for each angle of incidence (θ), the value of d is calculated using equation 4.2 and is tabulated in the Table 4.1. An average value of $d = 515$ nm is obtained, which is close to 495 ± 5 nm found from the SEM image. This formula holds good only at lower incident angles.

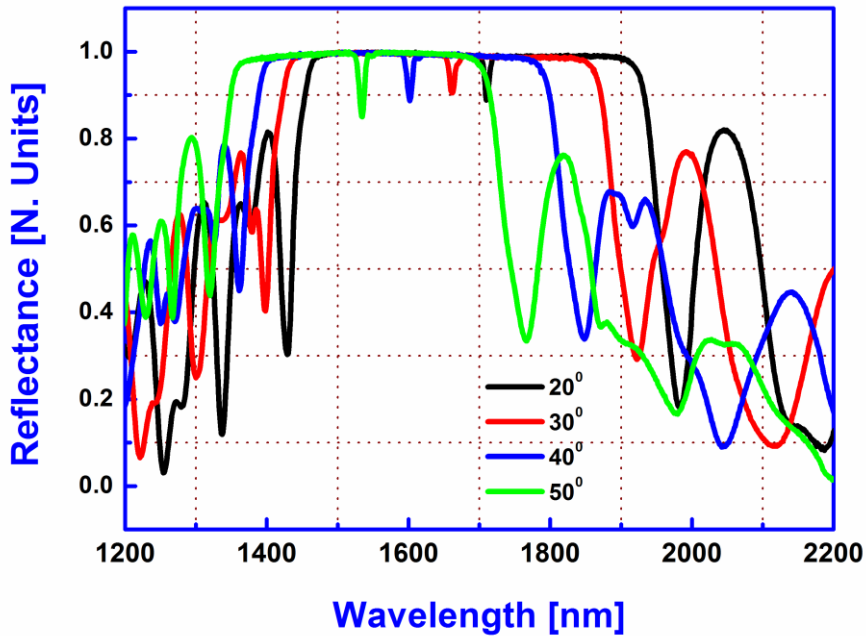


Figure 4.10: Reflectance spectra collected for the 1D PC using a variable angle reflection measurement system at 20° , 30° , 40° and 50° angle of incidence.

Table 4.1: The defect peak positions obtained from Figure 4.10 at different angles of incidence, the ‘d’ values calculated from Equation 4.2.

Angle of incidence (in degree)	Defect peak position (nm)	Calculated ‘d’ value (nm)
0	1749	492
10	1730	498
20	1710	543
30	1660	543

4.3.3 Spectroscopic properties of microcavity

Figure 4.11 shows the luminescence spectra of the ${}^4I_{13/2} \rightarrow {}^4I_{15/2}$ transition of the Er^{3+} ions observed for the 1D photonic crystal and for the reference sample composed by the single Er^{3+} - doped SiO_2 active layer, with only one Bragg mirror.

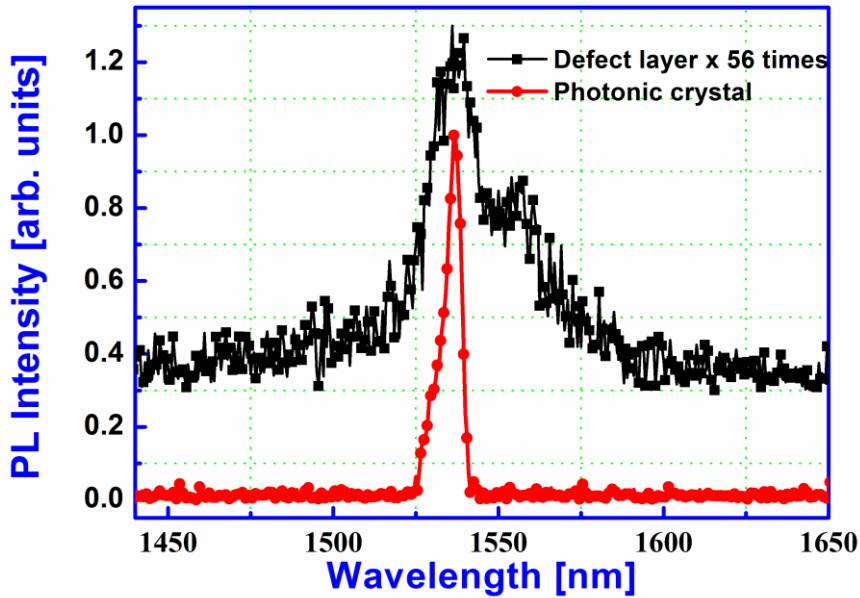


Figure 4.11: ${}^4I_{13/2} \rightarrow {}^4I_{15/2}$ photoluminescence spectra of the cavity activated by Er^{3+} ion in 1D photonic crystal (—●—) and of the single Er^{3+} - doped SiO_2 active layer with first Bragg mirror (—■—). The light is recorded at 50° from the normal on the samples upon excitation at 514.5 nm.

The excitation geometry as shown in Figure 4.2 has been used for the PL measurements. The excitation angle kept fixed at 20° for the plots shown in Figure 4.11. The luminescence from the cavity and from the Er³⁺ - doped single SiO₂ layer with one Bragg reflector was detected at 50° with solid angle of 10⁻¹ sr. All angles are measured with respect to the normal to the sample surface. Both the cavity and the Er³⁺ - doped single SiO₂ layer with first Bragg reflector were excited with the 514.5 nm line of an Ar⁺ ion laser with an excitation power of 180 mW. The Erbium emission from the reference sample is centered at 1538 nm with a FWHM of 29 nm and exhibits the characteristic shape of Er³⁺ ion in silica glass [8]. The position of the cavity resonance is strongly dependent on the detection angle. For a detection angle of 50°, the cavity resonance corresponds to the maximum of the Erbium PL of the Er³⁺ - doped SiO₂ active layer with the first Bragg. The peak luminescence intensity of Er³⁺ ions is enhanced by a factor 56, in respect to that detected for the reference at the corresponding wavelength. The Er³⁺ ⁴I_{13/2}→⁴I_{15/2} PL line shape is strongly narrowed by the cavity and exhibits a FWHM of 5 ± 0.5 nm (Figure 4.11). The Er³⁺ emission is enhanced when the wavelength corresponds to the cavity resonant mode and weakens for the other emission wavelengths.

To bring out the evidence on the effect of detection angle on the emission features of the photonic crystal, we have repeated the luminescence measurements with different detection configuration. In Figure 4.12, we report the angle dependent reflectance spectra obtained at 20°, 30°, 40° and 50° angle of incidence and the luminescence spectrum obtained by detecting the luminescence at 50° from the normal incidence. The position of the cavity resonance shifts with the detection angle and when the resonance corresponds to the wavelength of the emission band of the Er³⁺ ions the emission peak is observed from the sample and is aligned with the minimum of the reflectance.

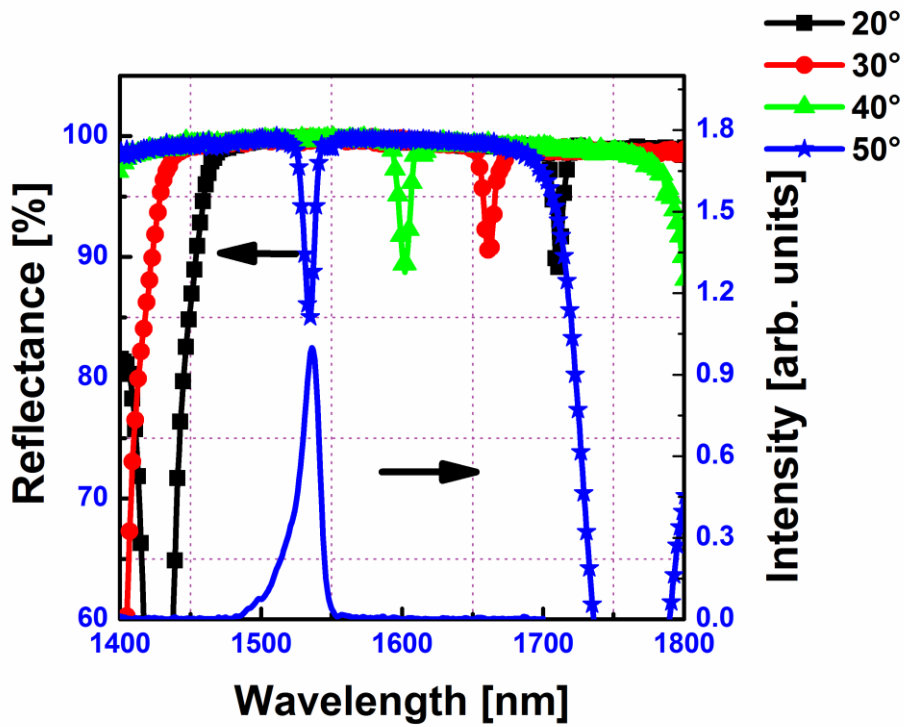


Figure 4.12: Angle dependence reflectance spectra and luminescence spectrum obtained detecting the luminescence at 50° from the normal incidence.

The reflectance spectrum of the microcavity is largely dependent on thickness and index variations of the individual layers. In a microcavity, the defect layer accommodates a resonant optical mode whose line width is determined by the reflectance of the adjacent mirrors. We calculated the Q value from PL spectra, which is 342. The reflectance (R) of each DBR is deduced from this Q value [5], with the relation

$$Q = \frac{(1 + \sqrt{R})^2}{(1 - R)}$$

Q value of 342 leads to R=98.8%. Thus, by measuring Q, we obtain a direct indication of the thickness and index of the films accurately.

The microcavity resonance is strongly dependent on the detection angle; for a detection angle of 50° angle, the cavity resonance corresponds to the centre of the Erbium PL line as is shown in Figure 4.13. At larger collection angles, the

cavity resonance moves away from the PL peak towards the emission tail. Keeping the excitation angle constant at 20° , for the 514.5 nm laser line, the detection angle is varied from 50° to 62° .

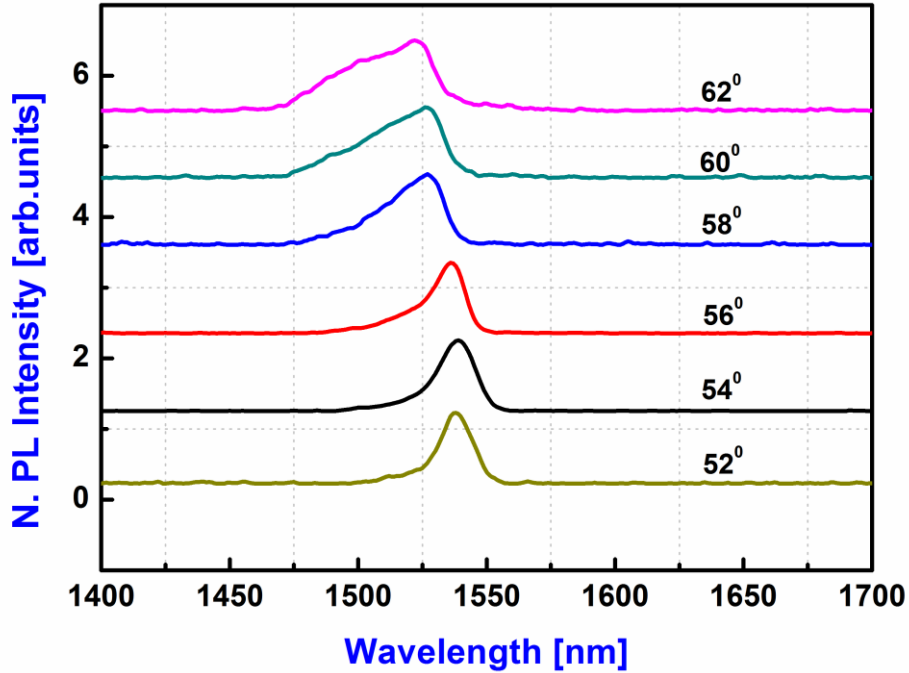


Figure 4.13: PL spectrum of the cavity at different angles of detection and fixed excitation angle using the back excitation geometry.

The PL spectrum is collected at intervals of 2 degrees. In agreement with the reflectance spectra of Figure 4.10, the PL peak shifts to lower wavelengths at higher angles. Also, at larger angles of detection, the emission at 1538 nm does not get completely subdued due to its high peak intensity in comparison to the emission tail. However, the luminescence peak position is observed to shift from 1538 nm (at 50°) to 1524 nm (at 62°) leading to a 14 nm wide tuning range within the stop band.

4.4 Conclusions

A valuable protocol based on rf sputtering technique was developed for the fabrication of Er^{3+} activated 1D photonic crystals. The cavity is constituted by

an Er^{3+} - doped SiO_2 active layer inserted between the two Bragg reflectors consisting of ten pairs of $\text{SiO}_2/\text{TiO}_2$ layers. Scanning electron microscopy was used to measure directly the thickness of the layers and put in evidence the homogeneities of the layers and their good adhesion. NIR transmittance and variable angle reflectance spectra confirm that the presence of a stop band from 1500 nm to 2000 nm with a cavity resonance centered at 1749 nm at 0° , a FWHM 1.97 nm, corresponding to a quality factor (Q) of about 890. The effect of the cavity on the ${}^4\text{I}_{13/2} \rightarrow {}^4\text{I}_{15/2}$ emission band is demonstrated by the narrowing of the emission band as well as by the enhancement of the Er^{3+} PL intensity. The latter effect is verified by the observation that the peak luminescence intensity from the photonic crystal is 54 times higher than that of the reference sample under the same excitation condition. In conclusion, three important outcomes characterize this work: 1) fabrication protocol leading to a specific control of compositional, optical and geometrical parameters allowing high Q factor and luminescence enhancement; 2) extent of the stop band and the resonance to longer wavelengths leading to potential new functionalities; 3) the reference sample fabrication and the employed geometry allowed a reliable assessment of the influence of the cavity and we believe that this method can be largely employed so that the errors on luminescence enhancement measurement due to the different configurations may be drastically reduced.

4.5 References

1. E. Yablonovitch, "Inhibited Spontaneous Emission in Solid State Physics and Electronics," *Phys. Rev. Lett.* **58**, 2059 (1987).
2. S. John, "Strong Localization of Photons in Certain Disordered Dielectric Super lattices," *Phys. Rev. Lett.* **58**, 2486 (1987).
3. J. D. Joannopoulos, R. Meade and J. N. Winn, "*Photonic Crystals: Molding the Flow of Light*" (Princeton U. Press, Princeton, N.J., 1995).
4. J. Bellessa, S. Rabaste, J. C. Plenet, J. Dumas, J. Mugnier and O. Marty, "Eu³⁺- doped microcavities fabricated by sol-gel process," *Appl. Phys. Lett.* **79**, 2142 (2001).

5. S. Rabaste, J. Bellessa, A. Brioude, C. Bovier, J. C. Plenet, R. Brenier, O. Marty, J. Mugnier and J. Dumas, "Sol-gel fabrication of thick multilayers applied to Bragg reflectors and microcavities", *Thin Solid Films* **416**, 242 (2002).
6. R.M. Almeida and Z. Wang, "Sol-gel preparation of one-dimensional photonic bandgap structures", *SPIE Proc.* **4655**, 24 (2002).
7. R. M. Almeida and A. S. Rodrigues, "Photonic bandgap materials and structures by sol-gel processing," *J. Non-Cryst. Solids* **326&327**, 405 (2003).
8. A. Chiappini, A. Chiasera, C. Armellini, S. Varas, A. Carpentiero, M. Mazzola, E. Moser, S. Berneschi, G. C. Righini and M. Ferrari, "Sol-gel derived photonic structures: fabrication, assessment, and application," *J. Sol-Gel Science & Technol.* **60**, 408-425 (2011).
9. T. Yoshie, L. Tang and S. Su, "Optical Microcavity: Sensing down to single molecules and atoms," *Sensors* **11**, 1972-1991 (2011).
10. V. E. Ferry, A. Polman and H. A. Atwater, "Modeling light trapping in nanostructured solar cells," *ACS Nano* **5**, 10055-10064 (2011).
11. M. Ferrari and G.C. Righini, "*Physics and Chemistry of Rare-Earth Ions Doped Glasses*" (Trans Tech Publishers 2008) Chapter 3.
12. C. M. Johnson, P. J. Reece and G. J. Conibeer, "Slow-light-enhanced up conversion for photovoltaic applications in one-dimensional photonic crystals," *Opt. Lett.* **36**, 3990-3992 (2011).
13. M. Clara Gonçalves, L. M. Fortes, R. M. Almeida, A. Chiasera, A. Chiappini, M. Ferrari and S. Bhaktha, "Photoluminescence in Er³⁺/Yb³⁺ - doped silica-titania inverse opal structures," *J. Sol-Gel Science & Technol.* **55**, 52-58 (2010).
14. G. C. Righini, Y. Dumeige, P. Féron, M. Ferrari, G. Nunzi Conti, D. Ristic and S. Soria, "Whispering gallery mode microresonators: fundamentals and applications," *Rivista del Nuovo Cimento* **34**, 435-488 (2011).

15. H. Rigneault, C. Amra, S. Robert, C. Begon, F. Lamarque, B. Jacquier, P. Moretti, A. M. Jurdyc and A. Belarouci, "Spontaneous emission into planar multi-dielectric microcavities: Theoretical and experimental analysis of rare earth ion radiations," *Opt. Mat.* **11**, 167-180 (1999).
16. A. Chiasera, R. Belli, S. N. B. Bhaktha, A. Chiappini, M. Ferrari, Y. Jestin, E. Moser, G.C. Righini and C. Tosello, "High quality factor Er³⁺-activated dielectric microcavity fabricated by rf-sputtering," *Appl. Phys. Lett.* **89**, 171910-1/3 (2006).
17. Y. Li, L. M. Fortes, A. Chiappini, M. Ferrari and R. M. Almeida, "High quality factor Er-doped Fabry-Perot microcavities by sol-gel processing," *J. Phys. D: Appl. Phys.* **42**, 205104-1/7 (2009).
18. J. Jasieniak, C. Sada, A. Chiasera, M. Ferrari, A. Martucci and P. Mulvaney, "Sol-gel based vertical optical microcavities with quantum dot defect layers," *Adv. Funct. Mater.* **18**, 3772-3779 (2008).
19. L. Persano, P. Del Carro, E. Mele, R. Cingolani, D. Pisignano, M. Zavelani-Rossi, S. Longhi and G. Lanzani, "Monolithic polymer microcavity lasers with on-top evaporated dielectric mirrors," *Appl. Phys. Lett.* **88**, 121110-1/3 (2006).
20. S. F. Chichibu, T. Ohmori, N. Shibata and T. Koyama, "Dielectric SiO₂/ZrO₂ distributed Bragg reflectors for ZnO microcavities prepared by the reactive helicon-wave-excited-plasma sputtering method," *Appl. Phys. Lett.* **88**, 161914-1/3 (2006).
21. Y. Li and R. M. Almeida, "Photoluminescence from a Tb-doped photonic crystal microcavity for white light generation," *J. Phys. D* **43**, 455101-1/7 (2010).
22. G. Ma, J. Shen, Z. Zhang, Z. Hua and S. H. Tang, "Ultrafast all-optical switching in one-dimensional photonic crystal with two defects," *Opt. Exp.* **14**, 858-865 (2006).
23. Y. G. Boucher, A. Chiasera, M. Ferrari and G. C. Righini, "Photoluminescence spectra of an optically pumped erbium-doped

- microcavity with SiO₂/TiO₂ distributed Bragg reflectors,” *J. Lumin.* **129**, 1989–1993 (2009).
24. A. Wajid, “On the accuracy of the quartz-crystal microbalance (QCM) in thin-film depositions,” *Sensors and Actuators A* **63**, 41-46 (1997).
25. S. Boyadzhiev, V. Georgieva and M. Rassovska, “Characterization of reactive sputtered TiO₂ thin films for gas sensor applications,” *Journal of Physics: Conference Series* **253**, 012040-1/6 (2010).
26. S. J. L. Ribeiro, Y. Messaddeq, R. R. Gonçalves, M. Ferrari, M. Montagna and M. A. Aegerter, “Low optical loss planar waveguides prepared by an organic-inorganic hybrid system,” *Appl. Phys. Lett.* **77**, 3502-3504 (2000).
27. R. M. Almeida and S. Porta, “Photonic band gap structures by sol-gel processing,” *Curr Opin Solid State Mater Sci.* **7**, 151 (2003).

Chapter 5

Enhanced nonlinear optical response in one dimensional photonic crystal with ZnO defect layer

Abstract:

Enhanced nonlinear optical response was observed in one dimensional photonic crystals with ZnO defect. One dimensional photonic crystals containing ZnO defect layer was fabricated by rf sputtering technique. The transmission spectra of this photonic crystal revealed a defect mode resonance and a broad photonic band gap. Open aperture Z-scan measurements shows that the Z-scan curve of the detuned resonant photonic crystal exhibited a larger transmittance dip as compared to a single layer of ZnO reference. Nearly 21 times increase in the nonlinear absorption was observed for the photonic crystal structure when compared to a single layer of the ZnO reference. The enhancement of the nonlinear absorption in the detuned resonant photonic crystal is due to the strong confinement of the optical field around the defect layer. We have observed good optical limiting behaviour in photonic crystal which is due to the large enhancement of nonlinear absorption in the photonic crystal structure.

5.1 Introduction

Since the photonic crystals can efficiently control the propagation of the electromagnetic wave, they have led to tremendous interest in recent years and many applications have been suggested, such as filters, wave guides, optical switches and so on [1 - 3]. In addition to micro lasers and waveguides, we need nonlinear optical devices which operate at very low power for future optical processing technology [4]. As far as the photonic crystals with optical nonlinearities are concerned, for the future practical applications of photonics, it is necessary to find nonlinear optical materials with high optical nonlinearity and fast time response. Such a device can reduce the intensities needed to achieve the required nonlinearity. A second option would be to enhance the local fields so that requirement on the external field reduces. Here we demonstrate the field enhancement in a one dimensional (1D) photonic crystal, which in turn can be used as an optical limiter. Optical limiting in two-dimensional photonic crystals was proposed and experimentally examined using a thermal nonlinearity [5]. Scalora et al. [6] first proposed 1D photonic band gap (PBG) optical limiters based on a nonlinear shift of the band edge. Recently, experimental results were also reported in 1D metallo-dielectric [7] and in 3D colloidal photonic crystals [8].

When a defect layer is inserted at the centre of the photonic crystal structure, a localized optical mode appears in the PBG as a defect level, and light can be strongly confined within the defect layer of the PBG. The localization of light leads to an increase in the optical electric field in the defect layer. If a nonlinear material is used as defect medium, it is expected that strong enhancement of optical nonlinearity by several orders of magnitude can be obtained in the defect layer, owing to the highly localized field [9]. Many bulk materials have been studied with widespread applications in optoelectronics and they display attractive nonlinear characteristics based on Kerr nonlinearity, two- or three-photon absorption (TPA) [10] and optical solitons [11]. Very little work

has been done on an important application such as optical limiting using a combined structure of the strong nonlinear absorbing material and the field confinement properties of the PBG structure [12, 13]. Due to an effective localization of electric field in the defect layer of a 1D PBG structure, the performance of an optical limiter can be improved by introducing the bulk nonlinear material into the PBG structure as a defect. High third order nonlinearity and large nonlinear absorption of ZnO has attracted many researchers to use this material for many prospective optical devices, such as optical switches and optical phase conjugators [14]. Therefore, the study of enhancement of optical nonlinearities in ZnO defect contained in a 1D photonic crystals are important for practical applications in optical limiting devices and all-optical switching elements, which involve intense fields.

In this chapter, we will be describing the fabrication of $\text{SiO}_2/\text{TiO}_2$ 1D photonic crystal with ZnO as a defect layer using rf sputtering and try to demonstrate the nonlinear optical properties by carrying out the nanosecond Z-scan studies.

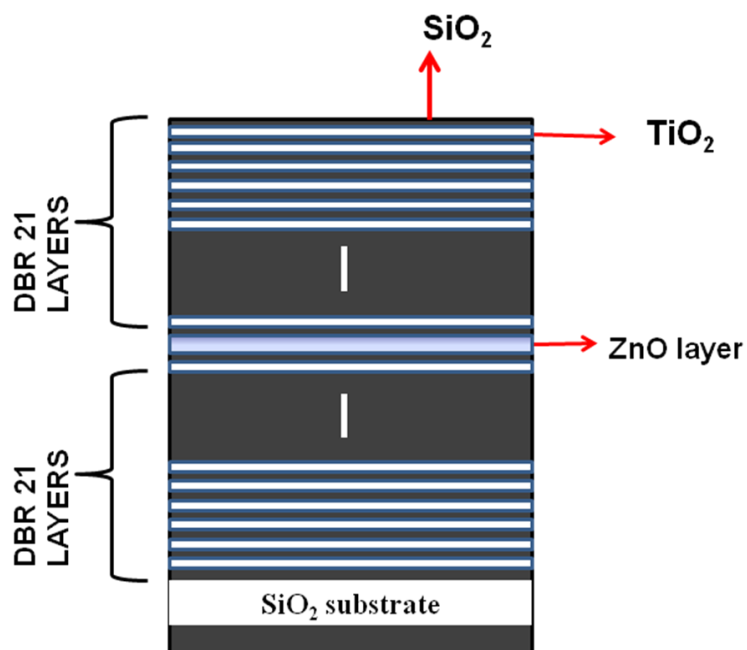


Figure 5.1: Schematic diagram for 1D microcavity with ZnO defect

5.1.1 Nonlinear Optics

Nonlinear optics is the study of phenomena that occur as a consequence of the modification of the optical properties of a material system by the presence of intense light. Typically, only laser light of sufficient intensity can modify the optical properties of a material system. Nonlinear optical phenomena are “nonlinear” in the sense that they occur when the response of a material system to an applied optical field depends on the strength of the optical field in a nonlinear manner.

In the case of linear (i.e., at low intensities) optics, the induced polarization \bar{P} depends linearly on the electric field strength \bar{E} in a manner that can often be described by the relationship,

$$\bar{P} = \varepsilon_0 \chi^{(1)} \cdot \bar{E} \quad (5.1)$$

where the proportionality constant $\chi^{(1)}$ is known as linear susceptibility, ε_0 is the permittivity of free space. The attenuation of an optical beam propagating in an absorbing medium can be described as

$$\frac{dI}{dz} = -\alpha I \quad (5.2)$$

where I is the beam intensity, z is the propagation length along the beam propagation direction, and α is a absorption coefficient for a given medium. The physical meaning of Eq. (5.2) is that the decrease of beam intensity in a unit propagation length is linearly proportional to the intensity itself. From the equation (5.2), we can obtain a well known Beer-Lambert law expression

$$I(z) = I(0)e^{-\alpha z} \quad (5.3)$$

In case of nonlinear optics, when a medium is subject to an intense electric field such that due to an intense laser pulse, the polarization response of the material is not adequately described by equation (5.1). Assuming that the polarization of the

medium is still weak compared to the binding forces between the electrons and nuclei, polarization can be expressed in a power series of the field strength \bar{E}

$$\bar{P} = \chi^{(1)}\bar{E} + \chi^{(2)}\bar{E}\bar{E} + \chi^{(3)}\bar{E}\bar{E}\bar{E}..... \quad (5.4)$$

The quantities $\chi^{(2)}$ and $\chi^{(3)}$ are known as the second- and third order nonlinear optical susceptibilities, respectively. $\chi^{(2)}$ involves in the processes like, second harmonic generation (SHG), difference frequency generation (DFG) etc. $\chi^{(3)}$ involves in multiphoton absorption processes. As $\chi^{(2)}$ vanishes for a centrosymmetric system and for the materials of the present study, we will consider only effects due to $\chi^{(3)}$ as the smallest nonlinear effect.

5.1.1.1 Nonlinear absorption

Nonlinear absorption refers to the change of transmittance of a material as a function of intensity or fluence. The high intensities can induce profound changes in the optical properties of a material leading to a nonlinear response of the real and imaginary parts of polarization. The imaginary part of the nonlinear polarization is associated, for instance, with multiphoton transitions and will exhibit a n -photon resonance when two level of an atomic or molecular system can be connected by n optical quanta.

5.1.1.2 Multiphoton absorption

TPA involves a transition from ground state (1) of a material to a higher lying state (2) by the simultaneous absorption of two photons via an intermediate virtual state, as schematically shown in Figure 5.2.

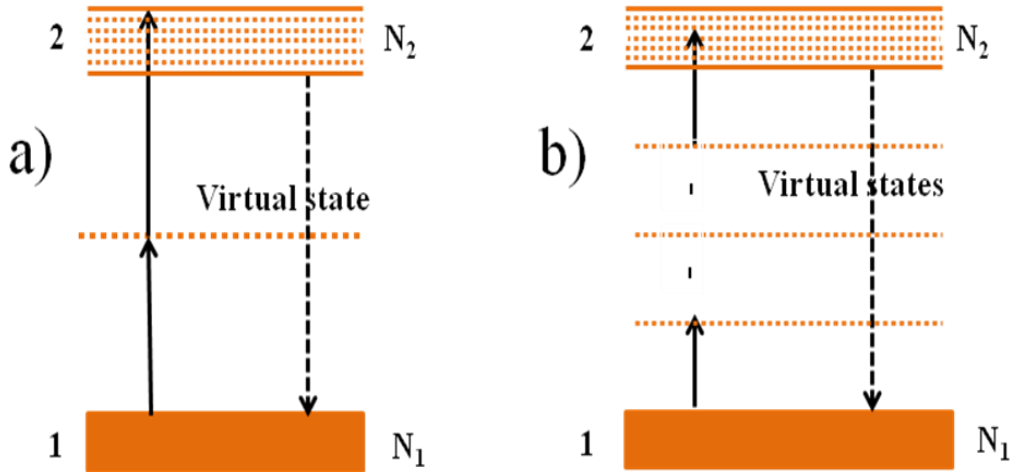


Figure 5.2: Schematic energy level diagram for (a) Two-photon absorption (TPA); (b) Multi-photon absorption.

In this case, the attenuation of the incident light is described by

$$\frac{dI}{dz} = -\beta I^2 \quad (5.5)$$

where β is the two-photon absorption coefficient.

Multiphoton absorption involves a transition from the ground state to a higher lying state by the simultaneous absorption of three or more number photons via multiple numbers of virtual states. Energy level diagrams of 1-photon to n-photon absorption are shown in the Figure 5.2(b).

In this case, the attenuation of the incident light is described by

$$\frac{dI}{dz} = -\alpha_n I^n \quad (5.6)$$

Where α_n is the n-photon absorption coefficient.

$$\frac{dI(z)}{dZ} = -\alpha_n I^n(z) \quad (5.7)$$

$$\int_{I_{in}}^{I_{out}} \frac{1}{I^n(z)} dI(z) = -\alpha_n \int_0^L dZ \quad (5.8)$$

$$\left[\frac{I^{-n+1}}{-n+1} \right]_{I_{in}}^{I_{out}} = -\alpha_n L \quad (5.9)$$

$$\frac{1}{n-1} \left[\frac{1}{I_{in}^{n-1}} - \frac{1}{I_{out}^{n-1}} \right] = \alpha_n L \quad (5.10)$$

where transmittance $T = \frac{I_{out}}{I_{in}}$

$$\frac{1}{(n-1)I_{in}^{n-1}} \left[1 - \frac{1}{T^{n-1}} \right] = \alpha_n L \quad (5.11)$$

$$T^{n-1} = \frac{1}{1 + (n-1)\alpha_n L I_{in}^{n-1}} \quad (5.12)$$

$$T = \frac{1}{\left[1 + (n-1)\alpha_n L I_{in}^{n-1} \right]^{1/n-1}} \quad (5.13)$$

$$\frac{I_{in}}{\omega_0^2} = \frac{I_{00}}{\omega_z^2}$$

$$I_{in}(z) = \frac{I_{00}}{\left[1 + \frac{Z^2}{Z_0^2} \right]} \quad (5.14)$$

where $\omega_z^2 = \omega_0^2 \left[1 + \frac{Z^2}{Z_0^2} \right]$

$$T = \frac{1}{\left[1 + (n-1)\alpha_n L \left(\frac{I_{00}}{\left(1 + \left(\frac{Z}{Z_0} \right)^2 \right)} \right)^{n-1} \right]^{1/n-1}} \quad (5.15)$$

$$T_{OA(nPA)} = \frac{1}{\left[1 + (n-1)\alpha_n L \left(\frac{I_{00}}{\left(1 + \left(\frac{Z}{Z_0} \right)^2 \right)} \right)^{n-1} \right]^{1/n-1}} \quad (5.16)$$

where I_{00} is the peak intensity (at $z = 0$), I_{in} is the intensity at sample position, $Z_0 = \frac{\pi\omega_0^2}{\lambda}$ is Rayleigh range, ω_0 is the beam waist at the focal point ($Z = 0$), dz is a small slice of the sample and $I_{out}(z)$ is output intensity of the sample. The Z-scan technique was introduced by Sheik-Bahae et al. [15] for accurate and sensitive measurements of nonlinear absorption ($\alpha_2 = \beta$) and refraction by translating a sample along the optical axis of a focused Gaussian beam.

A smart optical limiter is needed that is transparent for low input intensities and clamps throughput at high input intensities, and is effective over a wide band of wavelengths. Optical limiters (OL) are one of the most important types of devices used to control the amplitude of high intensity optical pulses. These devices work due to intrinsic properties of the materials used for their fabrication. An ideal optical limiter has a linear transmittance at low input intensities, but above the threshold intensity (I_{th}) (at which non linear absorption takes place) its transmittance becomes constant. The ideal behavior of such a device is shown in Figure 5.3. In literature people have reported the OL studies

with semiconductor, metal, organic nanoparticles and graphene composites [16-18]. A wide variety and well known nonlinear optical phenomenon like multiphoton absorption, excited state absorption, self-focusing or defocusing and nonlinear scattering are exploited for achieving OL [18-19].

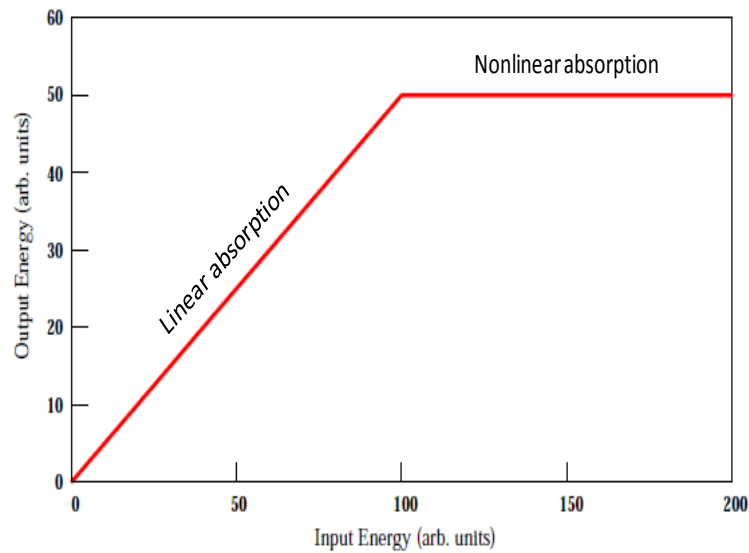


Figure 5.3: An ideal optical limiter.

5.1.1.3 Nonlinear refraction

The change in the refractive index or spatial distribution of the refractive index profile of a medium due to the presence of an intense optical field is called the nonlinear refractive index (n_2). The refractive index in the presence of this type of nonlinearity can be represented as

$$n = n_0 + n_2 I \quad (5.17)$$

where n_0 is the usual refractive index, and $n_2 = \frac{12\pi^2}{n_0^2 c} \chi^{(3)}$ is an optical constant

that characterizes the strength of the nonlinearity. Some of the processes that can occur as a result of the intensity dependent refractive index of our interest are self-focusing, and self-phase modulation.

5.2 Experimental

SiO₂/TiO₂ 1D photonic crystal with ZnO defect layer was prepared by using multi target rf sputtering technique using silica and silicon substrates. The sample deposited on silicon was employed for scanning electron microscopy (SEM) measurements and the sample deposited on silica substrate was employed for transmittance and nonlinear absorption measurements. The substrates were cleaned inside the rf sputtering deposition chamber by heating at 120° C for 30 min just before the deposition procedure. Sputtering deposition of the films was performed by sputtering alternatively a 15x5 cm² titania target and a 15x5 cm² silica target. For the defect layer, a 15x5 cm² ZnO target was used. The deposition time necessary to reach the appropriate thickness of the Bragg mirror layers was 50 min for titania target and was 30 min for silica target. The deposition time necessary to reach the appropriate thickness of the ZnO defect layer, to obtain cavity resonance centered at 0.545 μm, was 36 min. The residual pressure, before the deposition, was about 8.5x10⁻⁷ mbar. During the deposition process, the substrates were not heated and the temperature of the sample holder during the deposition was 30° C. The sputtering occurred with an Ar gas pressure of 5.4x10⁻³ mbar; the applied rf power was 150 W and 130 W with a reflected power 0 W for silica and titania targets, respectively. The applied rf power was 90 W for ZnO target.

Field emission scanning electron microscopy (FESEM) was used to analyze the morphology of the multi layer films and thickness of the each layer. The surface of the films was analyzed by a Carl - Zeiss Ultra 55 model apparatus at 15 kV by covering the films with a 2 nm gold layer. M-line spectroscopy was employed to obtain the refractive index and thickness of single layers of SiO₂, TiO₂ and ZnO films. The optical absorption of ZnO reference, visible region transmittance spectrum and variable angle reflectance spectrum of the cavity were obtained by using a double beam JASCO V-670 spectrophotometer. The variable angle Z-scan set up was used to measure the optical limiting and nonlinear optical absorption studies of the photonic crystal with ZnO defect and

ZnO reference. The ns laser source, which is a frequency doubled Nd: YAG laser (INDI-40, Spectra-Physics) with a 6 ns pulse duration and a repetition rate of 10 Hz at a 532 nm wavelength was employed for the Z-scan measurements. Open aperture Z-scan studies were carried out by focusing the input beam on to the sample using a lens of 120 mm focal length which gives $\sim 27 \mu\text{m}$ spot size at the focus in ns regime. The transmitted light was collected with a large area silicon photodiode. The peak intensity, I_{00} , estimated at the focus in the Z-scan experiments was 1.16 GWcm^{-2} for open aperture mode and 2.67 GWcm^{-2} for closed aperture mode. To allow a direct comparison of the nonlinear optical properties between the photonic crystal and the single active layer a reference sample was fabricated. The reference sample was deposited on a SiO_2 substrate during the same deposition run for the fabrication of the photonic crystal. The reference sample was therefore obtained by employing the same fabrication protocol and the targets used for the photonic crystal so that the defect layer in the 1D photonic crystal and the reference sample have the same thickness and composition.

5.3 Results and discussions

5.3.1 Refractive index profile

The simulated result of refractive index profile for the microcavity is shown in Figure 5.4. Y - Axis represents refractive index value and X - Axis represents thickness of the microcavity. Microcavity contains 43 layers with ZnO defect layer. The refractive index values used in the simulations were obtained with m-line technique. The refractive index values at 633 nm for SiO_2 , TiO_2 and ZnO are 1.46, 2.30 and 2.01 respectively.

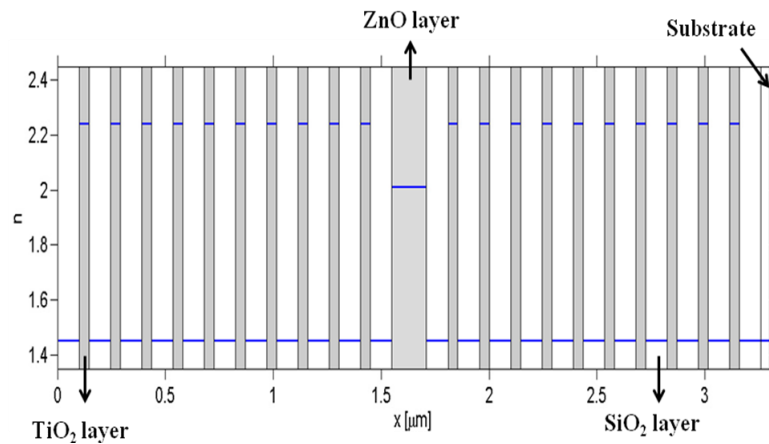


Figure 5.4: Refractive index profile for the microcavity.

5.3.2 Structural and optical properties of first Bragg mirror

Figure 5.5 shows the SEM cross sectional image of the first Bragg mirror. The Bragg mirror is constituted of 21 SiO₂/TiO₂ layers. The thickness of each of the SiO₂ and TiO₂ layers measured on the image is about 100 ± 5 nm and 45 ± 5 nm respectively. From Figure 5.5, for both materials the thickness fluctuation from one layer to the other is estimated at not more than ± 5 nm. The time period of the sputtering is optimized over several samples in order to obtain the stop band centered at 545 nm region, which is of current interest.

SiO₂ target, having a higher sputtering yield is sputtered for 30 min and TiO₂ with a lower sputtering yield is sputtered for 50 min. The samples are found to be comparatively thicker and uniform at the centre (in an area of about 1cm²) and gradually thin down towards the edges, as the plasma is concentrated at the centre during the deposition process. Hence care is taken to perform all the characterization nearer to the centre of the sample.

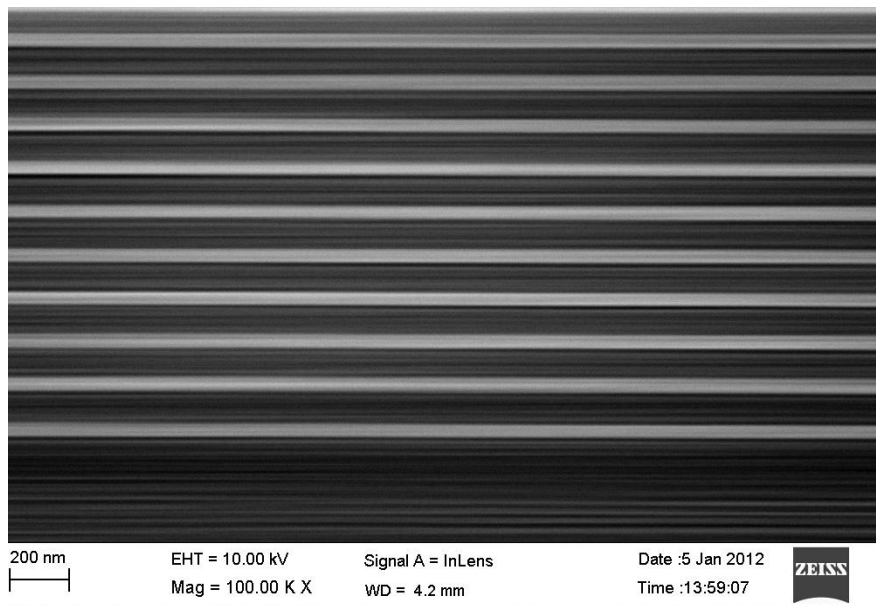


Figure 5.5: SEM cross sectional image of first Bragg mirror with 21 layers. Dark regions correspond to SiO_2 and bright regions correspond to TiO_2 .

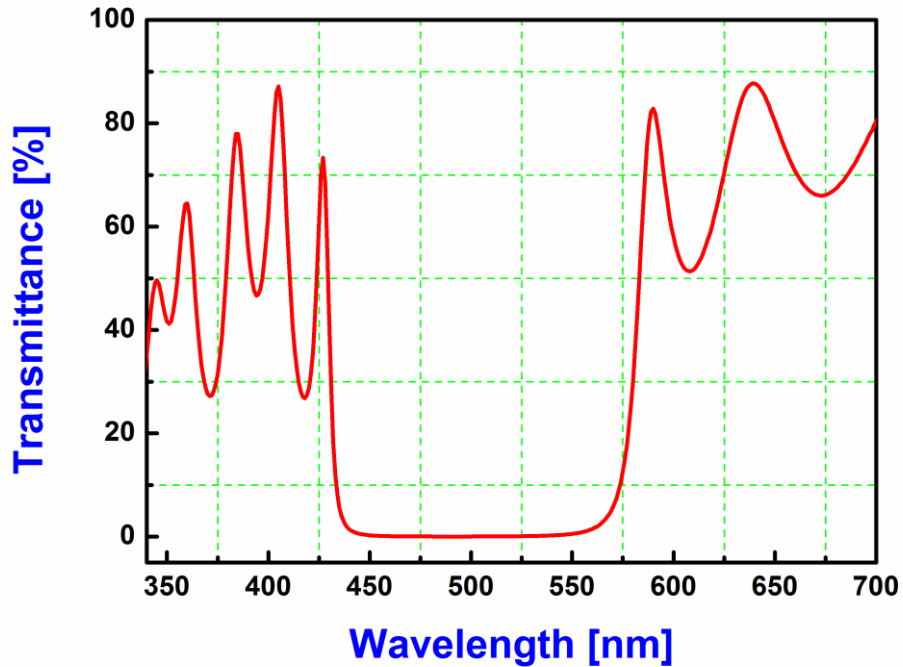


Figure 5.6: Transmission spectrum of the Bragg mirror with 21 layers. The reflection window of the mirror lies from 430 nm to 580 nm.

The transmission spectrum of the first Bragg mirror performed using the Jasco V-670 spectrophotometer is shown in the Figure 5.6. The ultra-low transmission band lies from about 450 nm to 550 nm with a 0.04 % minimum transmission through most parts of the stop band and contains 140 nm wide stop band.

5.3.3 Structural and optical properties of microcavity

The cavity is constituted by ZnO active layer inserted between two Bragg reflectors, each one consisting of 21 pairs of SiO₂/TiO₂ layers. SEM image of the cross section of the 1D photonic crystal with ZnO defect is shown in Figure 5.7. The dark regions correspond to SiO₂ and bright regions correspond to TiO₂ layers. It is possible to identify the defect layer and the two Bragg reflectors. From the SEM images, we estimated thicknesses of silica and titania layers as 100 ± 5 nm and 45 ± 5 nm respectively. ZnO defect layer thickness is found to be 160 ± 5 nm. The refractive indices at 633 nm of silica, titania and ZnO layers, measured by m-line spectroscopy on the single films, are 1.46 ± 0.001 , 2.30 ± 0.02 and 2.01 ± 0.02 respectively. The thickness of the single layer films measured by m-line spectroscopy is in good agreement with the measurement made with SEM analysis.

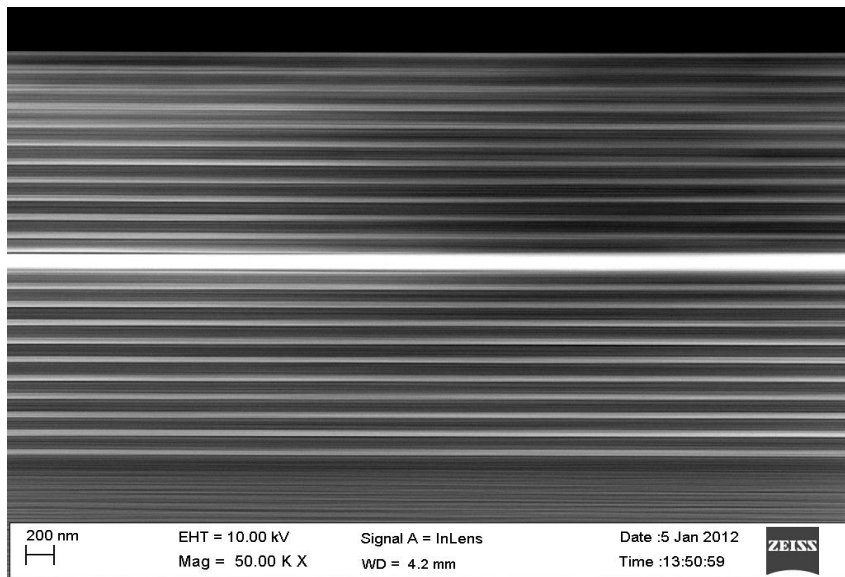


Figure 5.7: SEM micrograph of the 1D microcavity cross section. The bright and the dark areas are TiO_2 and SiO_2 layers, respectively; the defect layer can be recognized at the centre. The substrate is located on the bottom of the image and the air on the top.

The visible transmission spectrum is shown in Figure 5.8. The transmittance spectra were measured at 0° of incident angle. One can notice that the spectral reflectance range, i.e. the stop band, ranges from 420 nm to 590 nm. A sharp peak in the transmittance spectrum appears at 545 nm, which corresponds to the cavity resonance wavelength related to the half wave layer inserted between the two Bragg mirrors. To understand the position of the defect mode resonance, we performed a numerical simulation of the transmission spectra of multilayer structures [20, 21]. The optical constants used in the calculation of the transmission spectra were derived through m-line data. The calculated transmission spectra are close to the measured transmission spectra, as seen in Figure 5.8. This established that we could describe the observed transmission spectra using the optical transfer matrix formalism.

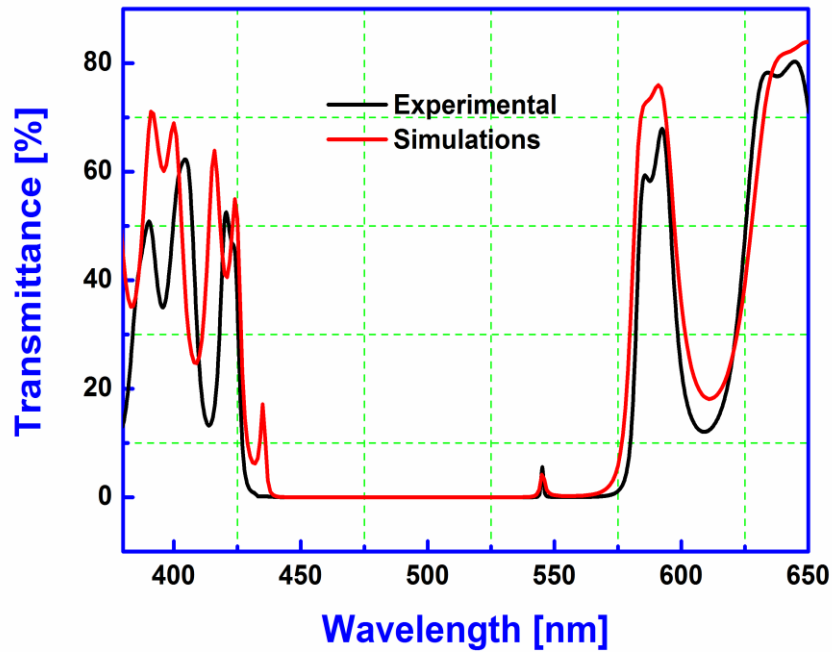


Figure 5.8: Transmittance spectrum of the microcavity with 43 layers. Experimental and simulation results on transmittance spectrum of the microcavity in the region between 400 and 600 nm. The stop band lies from 430 nm to 590 nm.

The transmittance spectrum presented in the Figure 5.9, obtained with a resolution of 0.1 nm, shows the sharp resonance line. The obtained FWHM for the resonance peak, with its maximum at 545 nm, is 1.08 nm which gives a quality factor (Q) of about 505.

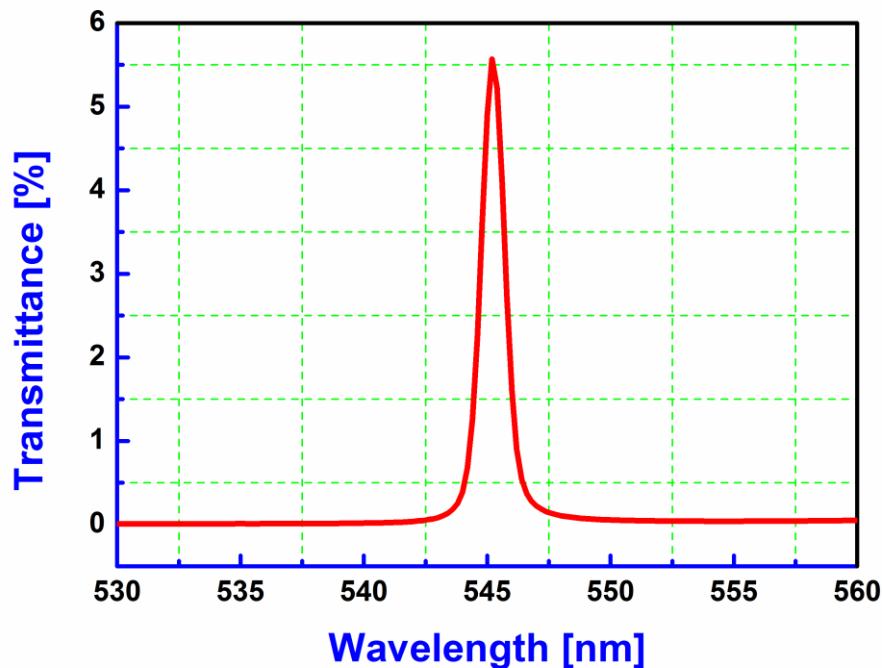


Figure 5.9: Experimentally obtained transmission spectrum of the cavity resonance correspond to the sharp maximum at 545 nm. The incident light is unpolarized.

5.3.4 Variable angle reflectance characteristics of microcavity

Figure 5.10 shows the variable angle reflection spectra for 1D photonic crystals with ZnO defect layer in the visible region. The spectra shown in Figure 5.10 (a) corresponds to the microcavity containing 40 layers of SiO₂, TiO₂, and ZnO defect layer. It is evident that the defect resonance appears at 594 nm at 10° incident angle. While moving to higher angle side, the stop band shifts towards the lower wavelengths region [22] and also the defect resonance shifts towards lower wavelengths region. The aim of the experiment is that, microcavity should transmit 532 nm wavelength light which should be due to defect resonance and study the nonlinear enhancements. In the case of, the spectra in Figure 10 (a), at 50° incident angle, the defect resonance presents at 532 nm light, but it transmits only 0.05% of 532 nm incident light. In case of spectra b, which is shown in

Figure 5.9 (b), microcavity contains 36 layers of SiO₂, TiO₂ and ZnO defect layer. The defect resonance appears at 532 nm while moving to 70° incident angle and it allows 0.06% of light.

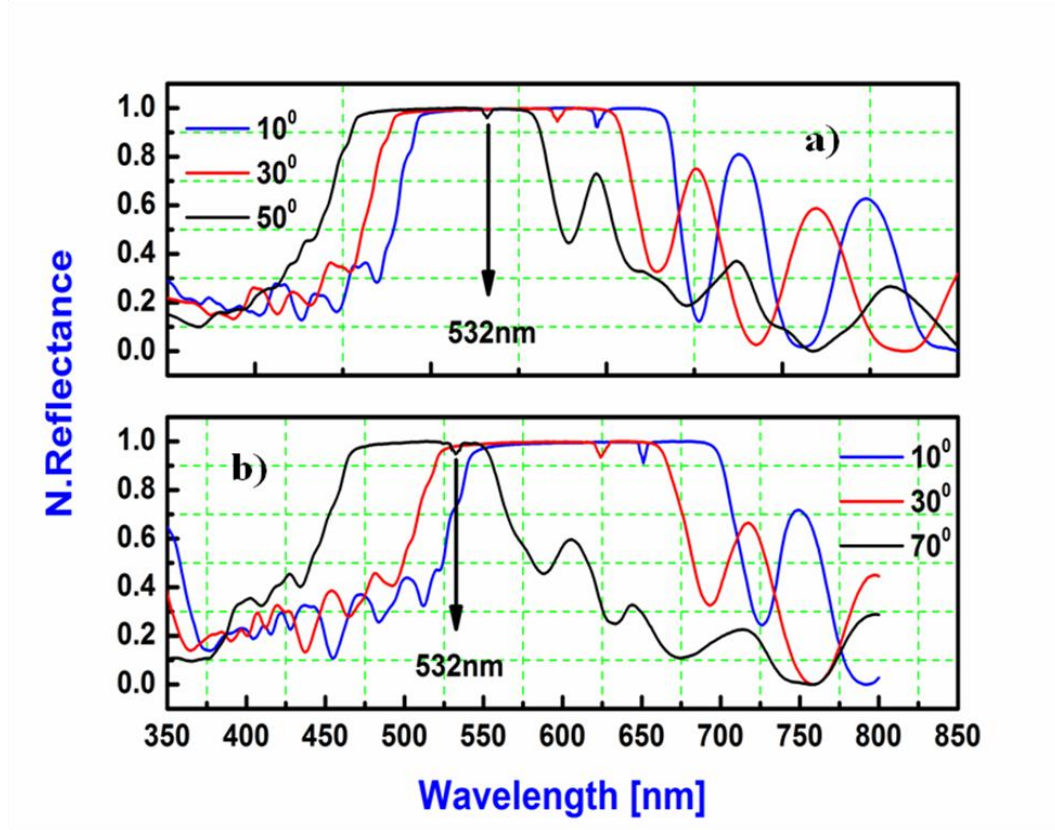


Figure 5.10: Variable angle reflectance spectra of the microcavity containing a) 41 layers with b) 37 layers. The spectra are measured at different incident angles.

We have prepared some series of samples, which contains ZnO defect layer. The variable reflection spectra shown in Figure 5.11, relates to the microcavity containing 42 layers of SiO₂, TiO₂ layers and ZnO defect layer. It is evident that at zero degree incident angle, the cavity positioned at 545 nm, while moving to higher angles, the stop band shifts towards the shorter wavelengths. At 30° angle, the cavity resonance peak appears at 532 nm and plays major role in transmission properties of the incident light as we measure the nonlinear absorption by using variable angle Z-scan set up with 532 nm laser light. At this position, the sample transmits 0.1% of incident light wavelength 532 nm. At the

position of 30° angle, we refer the photonic crystal with ZnO defect as “detuned resonant photonic crystal”. Among these three microcavities, we have chosen the sample which transmits maximum incident light of 532 nm.

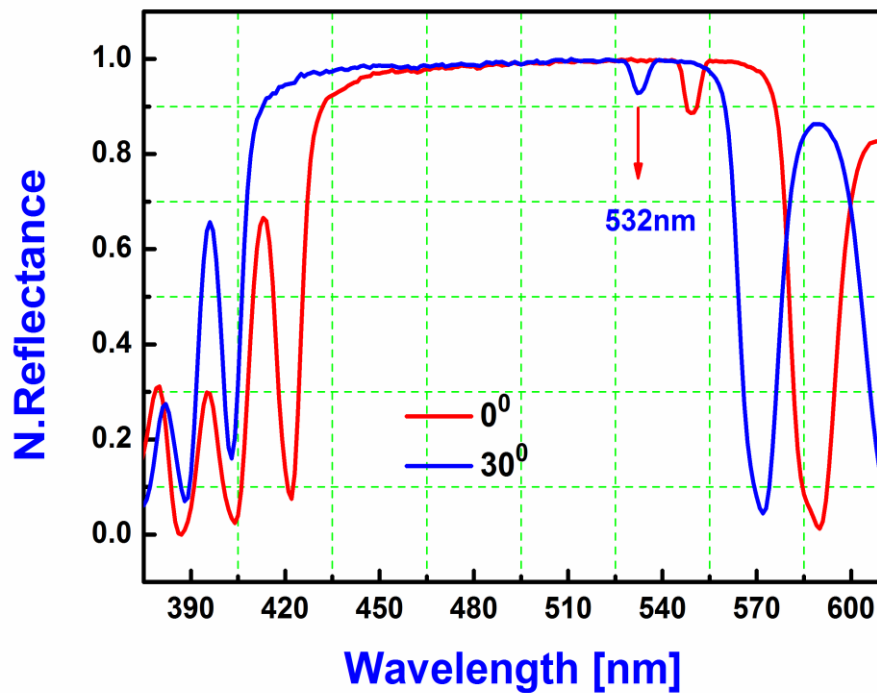


Figure 5.11: Variable angle reflectance spectra of the photonic crystal containing 43 layers with ZnO defect. The spectra are measured at 0° and 30° angles.

5.3.5 Optical absorption of ZnO

The absorption spectra of ZnO reference film is shown in Figure 5.12. It can be seen that the absorbance of the ZnO film is high at short wavelengths nearly 360 nm and low at long wavelengths > 380 nm. The intrinsic absorption in a semiconductor occurs for wavelengths in the vicinity of the energy gap. This absorption band of ZnO, leads to a strong two photon absorption for the excitation wavelength at 532 nm.

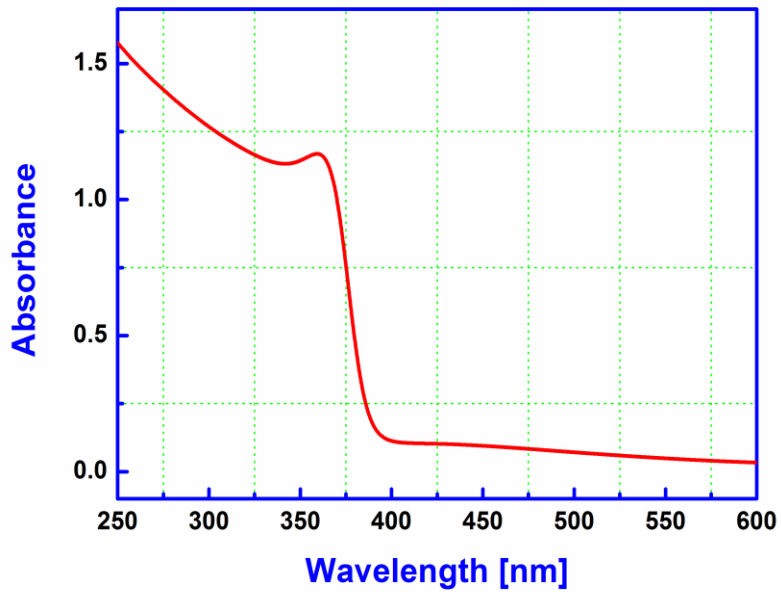


Figure 5.12: Optical absorption spectra of ZnO reference film.

5.3.6 Nonlinear optical properties

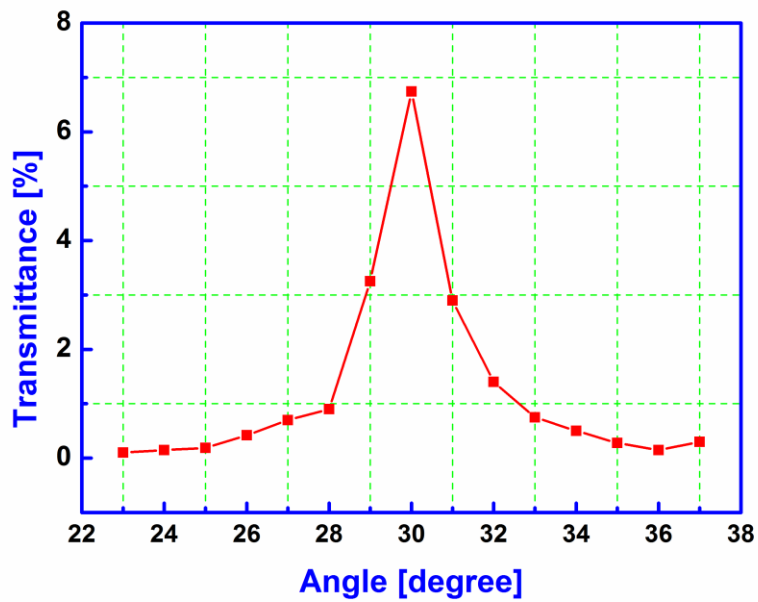


Figure 5.13: 532 nm light transmission through the photonic crystal with defect layer as a function of incident angle.

The spectra shown in Figure 5.13, describe the transmittance of 532 nm incident laser light as a function of the incident angle. The measurement was carried out during the Z-scan experiment, the sample was kept at focus and the transmittance was collected for different incident angles. At 30° incident angle, the 532 nm falls at the defect resonance and due to the defect mode transmission, we can see maximum light transmission from the photonic crystal. From the variable angle reflection spectra (Figure 5.11), the resonance mode move towards 532 nm while moving the higher angle side. This measurement is an evident that the system allows maximum light at 30° incident angle.

5.3.6.1 Nonlinear absorption and refraction

The nonlinear optical absorption of the samples was carried out with an open aperture angle dependant Z-scan technique. Assuming a spatial and temporal Gaussian profile for laser pulses and utilizing the open aperture (OA) Z-scan theory for TPA, we have the general equation for OA normalized energy transmittance, which can be obtained using equation (5.16), giving $n = 2$ and we have

$$T_{OA(TPA)} = \frac{1}{1 + \beta L_{eff} (I_{00} / (1 + (z/z_0)^2))} \quad (5.17)$$

Here β is the effective TPA coefficient, I_{00} is the peak intensity at the centre of the focus, z is the sample position, $z_0 = \frac{\pi\omega_0^2}{\lambda}$ is the Rayleigh range; ω_0 is the beam waist at the focal point ($z = 0$), λ is the laser wavelength; effective path lengths in the sample of length L for TPA is given as $L_{eff} = \frac{1 - e^{-\alpha_0 L}}{\alpha_0}$.

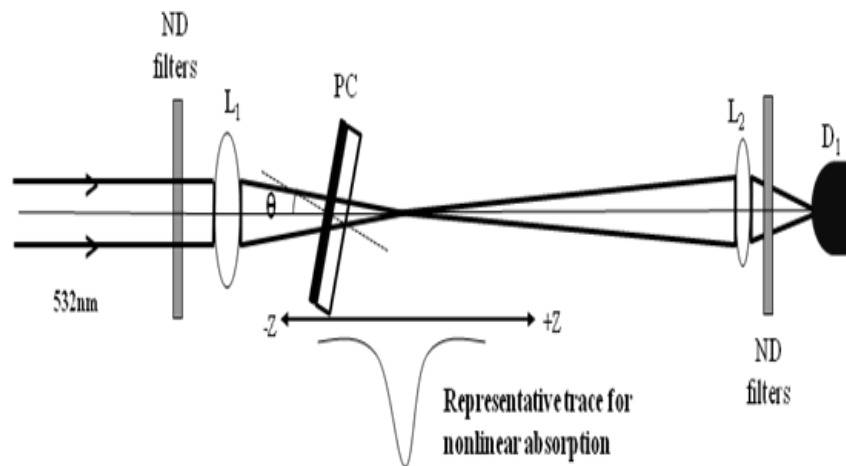


Figure 5.14: Schematic of the open aperture variable angle Z-scan set up for recording the nonlinear absorption. PC – Photonic crystal, L_1, L_2 – lens and D_1 – detector.

Figure 5.15 shows the normalized transmission of a Z-scan curve as function of distance from the focal point when 532 nm laser light made to incident at an angle of 30° for both microcavity and ZnO reference samples obtained at the same input intensity of about 1.6 GW/cm^2 in the open aperture mode. The data obtained with Z-scan measurement was fitted with the theoretical equation (5.17). The best fit produced an effective nonlinear absorption coefficient ($I\beta$) is $9.6 \times 10^3 \text{ cm}^{-1}$ for the photonic crystal and $1.76 \times 10^3 \text{ cm}^{-1}$ for ZnO reference sample. It is observed that nonlinear absorption for the photonic crystal was increased by 21 times when compared with single layer of ZnO reference film. This is attributed to the strong confinement of the optical field around the defect layer. Therefore the Z-scan curve of the detuned resonant photonic crystal produces larger two photon absorption value as compared with that of ZnO reference film.

Figure 5.16 shows the intensity dependant Z-scan curves for the photonic crystal with ZnO defect layer. It is clearly shows that, as the input intensity increases, the nonlinear absorption also increase. The damage threshold for the photonic crystal is $\sim 2 \text{ GW/cm}^2$.

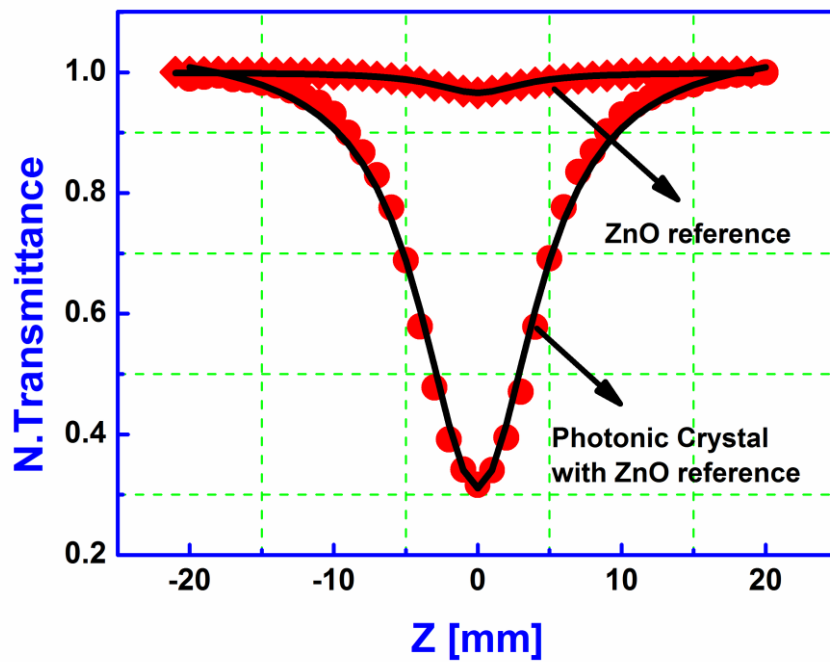


Figure 5.15: Z - Scan traces showing the normalized transmission of the ZnO reference (tetragon) and 1D photonic crystal with ZnO defect (circles) samples at 532 nm as a function of the distance from the focal point. The intensity at the focus was 1.6 GW/cm^2 . The solid lines represent the fit obtained by numerical calculations.

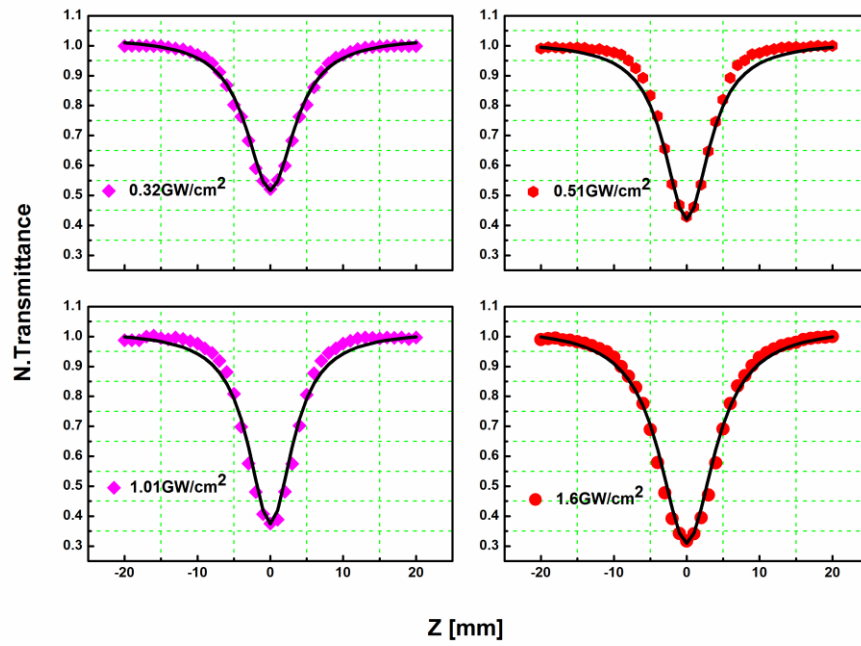


Figure 5.16: Intensity dependant Z-scan curves for photonic crystal with ZnO defect layer.

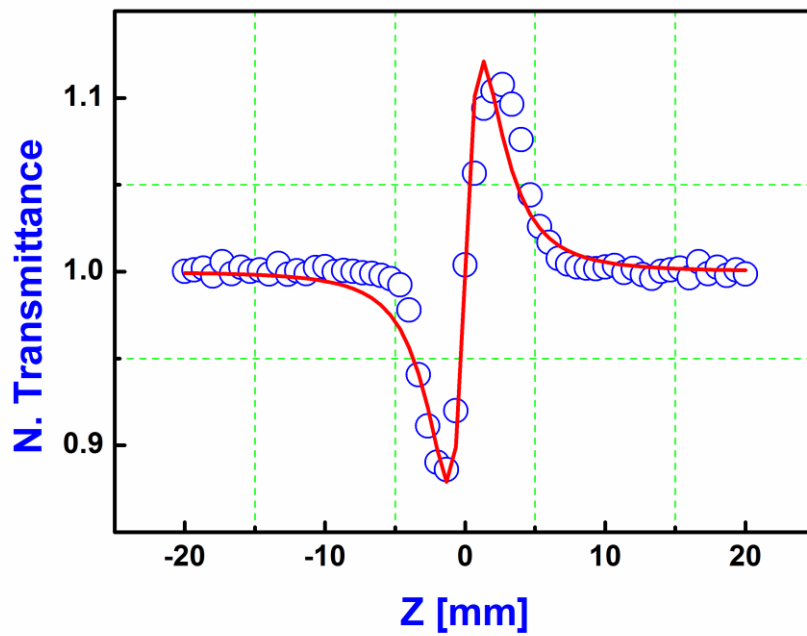


Figure 5.17: Closed aperture curve for the photonic crystal with ZnO defect.

Figure 5.17 shows the closed aperture curve for the photonic crystal with ZnO defect layer. It means that photonic crystal shows the nonlinear refraction. From the closed aperture signature, it shows that photonic crystal with ZnO defect shows a positive nonlinearity. The nonlinear refraction values obtained [15] with the equation

$$n_2 = \frac{\Delta\phi\lambda}{2\pi L_{\text{eff}} I_0} \quad (5.18)$$

where $\Delta\phi$ is the phase shift, can be obtained by fitting the experimental closed

aperture data with this equation: $T_{CA} = 1 + \frac{4\Delta\phi x}{(x^2 + 9)(x^2 + 1)}$ and $x = \frac{Z}{Z_0}$, Z_0 is the

Rayleigh range. λ is incident light wavelength and L_{eff} is effective length of the sample, I_0 is the input intensity at the focus. The nonlinear refraction value obtained for the photonic crystal with ZnO defect, from the equation is, $n_2 = 5.4 \times 10^{-11} \text{ cm}^2/\text{W}$. In case of ZnO reference sample, at a particular intensity, we have not observed any closed aperture signature at the same operating intensity.

5.3.6.2 Optical limiting

The nonlinear optical response of the 1D photonic crystal with ZnO defect layer was further explored by studying its optical limiting properties, where the optical power limiting devices are designed to control the transmission of intensity of a system. At low powers, the device displays linear transmittance until a set threshold is reached, after which point the transmitted intensity becomes nearly a constant. Such devices have attracted interest due to applications in providing protection from laser damage to eyes and optical sensors. In addition, the efficient control of optical limiting devices can lead to applications requiring pulse generations and shaping [23].

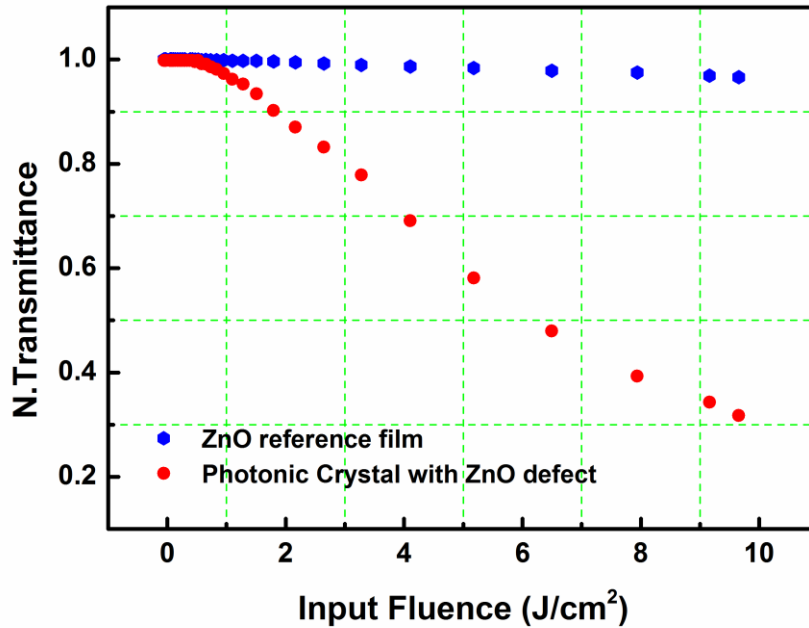


Figure 5.18: Optical limiting curves photonic crystal and ZnO reference as function of Normalized Transmittance vs Input fluence (J/cm²).

Optical limiting studies were carried out for the photonic crystal and ZnO reference sample using the same experimental conditions is shown in above Figure 5.18. It shows the normalized transmittance vs. input fluence for both photonic crystal and reference sample which represents the optical limiting behaviour of the photonic crystal and ZnO reference sample. Figure 5.19 shows the corresponding plots of the output energy (J/cm²) as function of the input energy density (J/cm²) and the red and black color spectra represent photonic crystal with ZnO defect layer and ZnO reference sample respectively. The linear transmittance for ZnO reference sample is 90% and for photonic crystal, it is 79%, which is due to the scattering losses in the Bragg reflectors. From Figure 5.19, we see that, for the photonic crystal, with increasing the input fluence, the output eventually begins to clamp.

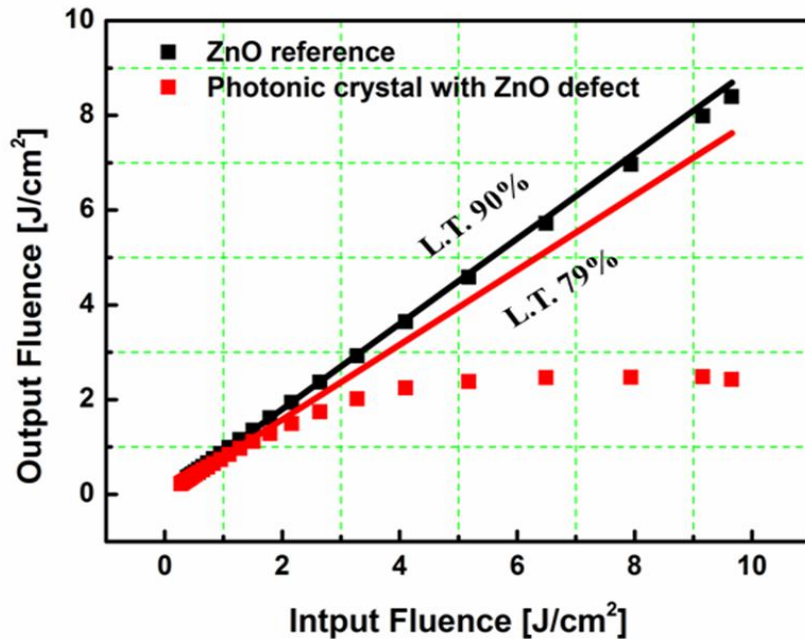


Figure 5.19: Optical limiting curves for photonic crystal and ZnO reference as a function of output fluence (J/cm^2) vs input fluence (J/cm^2). One dimensional photonic crystal output is shown to clamp at $2.3 (J/cm^2)$ indicating that optical limiting response from photonic crystal.

The output fluence at which the photonic crystal structure starts clamp, is called optical limiting threshold, is $2.3 J/cm^2$, while for the ZnO reference sample; we don't observe such behaviour because of the negligible nonlinearity at the given input intensity. The thickness of the ZnO reference film is nearly the same as that of the defect layer in the photonic crystal. It can be seen that the photonic crystal structure shows good optical limiting behaviour whereas the reference sample doesn't show it, which is due to the properties of the photonic bandgap of the photonic crystal and shows a very good promise as an optical coating on glass surface that can lead to a good optical limiter, switch, modulator or as band pass filter.

5.4 Conclusions

A valuable protocol based on rf sputtering technique is developed for the fabrication of 1D photonic crystal with defect layer. The cavity is constituted by ZnO defect layer between the two Bragg reflectors containing 21 pairs of SiO₂/TiO₂ layers. Scanning electron microscopy was used to measure directly the thickness of the layers and put in evidence the homogeneities of the layers and their good adhesion. The visible range transmittance and variable reflectance spectra confirm that the presence of a stop band from 420 nm to 590 nm with a cavity resonance centered at 545 nm for normal incidence of light. Nonlinear optical properties of photonic crystal with ZnO defect layer and ZnO reference sample were measured by variable angle Z-scan technique. We have observed that large enhancement in the nonlinear absorption of the photonic crystal as compared with ZnO reference. This effect is verified by the observation that the nonlinear absorption for the photonic crystal nearly increases by 21 times when compared with the reference sample under the same excitation conditions, which is attributed to the local field enhancement around the defect layer. As a result, we observed that photonic crystal shows good optical limiting behaviour, which has potential applications towards nonlinear optical devices.

5.5 References

1. X. Gu, X. F. Chen, Y. P. Chen, X. L. Zheng, Y. X. Xia and Y. L. Chen, "Narrowband multiple wavelengths filter in a periodic optical super lattice," *Opt. Commun.* **237**, 53 – 58 (2004).
2. J. K. Yang, H. Noh, M. J. Rooks, G. S. Solomon, F. Vollmer and H. Cao, "Lasing in localized modes of a slow light photonic crystal waveguide," *Appl. Phys. Lett.* **98**, 241107 (2011).
3. A. Hache and M. Bourgeois, "Ultrafast all-optical switching in a silicon-based photonic crystal," *Appl. Phys. Lett.* **77(25)**, 6951 (2000).
4. R. Buhleier, V. Bardinal, J. H. Collet, C. Fontaine, M. Hubner and J. Kuhl, "Four-wave mixing in bulk GaAs microcavities at room temperature," *Appl. Phys. Lett.* **69**, 2240 (1996).

5. H. B. Lin, R. J. Tonucci and A. J. Campillo, "Two-dimensional photonic band gap optical limiter in the visible," *Opt. Lett.* **23**, 94-96 (1998).
6. M. Scalora, J. P. Dowling, C. M. Bowden and M. J. Bloemer "Optical Limiting and Switching of Ultra short Pulses in Nonlinear Photonic Band Gap Materials," *Phys. Rev. Lett.* **73**, 1368 (1994).
7. S. Husaini, H. Teng and V. M. Menon, "Enhanced nonlinear optical response of metal nanocomposite based photonic crystals" *Appl. Phys. Lett.* **101**, 111103 (2012).
8. K. S. Alee, M. B. M. Krishna, B. Ashok and D. N. Rao, "Experimental verification of enhanced electromagnetic field intensities at the photonic stop band edge of 3D polystyrene photonic crystals using Z-Scan technique," *Phot. Nano. Fund. Appl.* **10**, 236 (2012).
9. G. H. Ma, J. Shen, K. Rajiv, S. H. Tamg, Z. J. Zhang and Z.Y. Hua, "Optimization of two-photon absorption enhancement in one-dimensional photonic crystals with defect states," *Appl. Phys. B* **80**, 359–363, 2005.
10. Y. V. Kartashov, V. V. Konotop, V. A. Vysloukh and L. Torner, "Dissipative defect modes in periodic structures," *Opt. Lett.* **35(10)**, 1638-1640 (2010).
11. M. G. Vivas, T. Shih, T. Voss, E. Mazur and C. R. Mendonca, "Nonlinear spectra of ZnO: reverse saturable, two- and three-photon absorption," *Opt. Exp.* **18(9)**, 9628-9633 (2010).
12. N. N. Lepeshkin, A. Schweinsberg, G. Piredda, R. S. Bennink and R. W. Boyd, "Enhanced Nonlinear Optical Response of One-Dimensional Metal-Dielectric Photonic Crystals," *Phys. Rev. Lett.* **93**, 123902 (2004).
13. X. Liu, S. Chen, W. Zang and J. Tian, "Optical limiting in one-dimensional photonic band gap material with a bulk nonlinear defect," *J. Opt.* **13**, 015202 – 015207 (2011).
14. Z. K. Tang, G. K. L. Wong, P. Yu, M. Kawasaki, A. Ohtomo, H. Koinuma and Y. Segawa, "Room-temperature ultraviolet laser emission from self-assembled ZnO microcrystallite thin films," *Appl. Phys. Lett.* **72(25)**, 3270–3272 (1998).

15. M. Sheik-Bahae, A. A. Said, T. H. Wei, D. J. Hagan and E. W. Van Stryland, "Sensitive measurement of optical nonlinearities using a single beam," *IEEE Journal of QE* **26**, 760–769 (1990).
16. S. Porel, N. Venkatram, D. N. Rao and T. P. Radhakrishnan, "In situ synthesis of metal nanoparticles in polymer matrix and their optical limiting applications," *J. Nano. Nanotech.* **7**, 1887–1892 (2007).
17. M. B. M. Krishna, V. P. Kumar, N. Venkatramaiah, R. Venkatesan and D. N. Rao, "Nonlinear optical properties of covalently linked graphene-metal porphyrin composite materials," *Appl. Phys. Lett.* **98**, 081106 (2011).
18. L. W. Tutt, and T. F. Boggess, "A review of optical limiting mechanisms and devices using organics, fullerenes, semiconductors and other materials," *Progress in Quant. Elec.* **17**, 299–338 (1993).
19. R. L. Sutherland, "*Handbook of Nonlinear Optics*". (CRC Press: 2003).
20. P. Yeh, "*Optical waves in layered media*" (Wiley-Interscience, 2005).
21. J. Danlaert, K. Fobelets, I. Veretennicoff, G. Vitran and R. Reinisch, "Dispersive optical bistability in stratified structures," *Phys. Rev. B* **44**, 8214 (1991).
22. Y. Fink, J. N. Winn, S. H. Fan, C. P. Chen, J. Michel, J.D. Joannopoulos and E. L. Thomas, "A Dielectric Omni directional Reflector," *Science* **282**, 1679 (1998).
23. L. W. Tutt and T. F. Boggess, "A review of optical limiting mechanisms and devices using organics, fullerenes, semiconductors and other materials," *Prog. Quantum Electron.* **17**, 299 (1993).

Chapter 6

CO₂ laser and positron irradiation effects on pure GeO₂ planar waveguides

Abstract:

GeO₂ based planar optical waveguides were characterized using a protocol combining radio frequency sputtering technique and CO₂ laser, positron irradiation effects. The effects of pulsed CO₂ laser irradiation on the optical and structural properties of the waveguides are evaluated by different techniques as m-line and micro-Raman spectroscopy and atomic force microscopy (AFM). Amorphous GeO₂ planar waveguides were fabricated by Radio Frequency magnetron sputtering system on ν -SiO₂ substrate. After pulsed CO₂ laser annealing, an increase of the refractive index of approximately 0.04 at 1.5 μm and a decrease of the attenuation coefficient from 0.9 to 0.5 dB/cm at 1.5 μm was observed. Raman spectroscopy and AFM results put in evidence that after an adapted pulsed CO₂ laser annealing, the system showed a crystalline environment in which the phase of the crystalline GeO₂ varies with varying irradiation time. Moreover, positron annihilation spectroscopy was used to study the depth defect profile of the as prepared and laser annealed samples. The results obtained allowed getting information on the structural changes produced inside the waveguides films of approximately 1 μm thickness after the irradiation process. In addition, a density value for the amorphous GeO₂ samples was also obtained.

6.1 Introduction

GeO₂-based glasses have demonstrated to be one of the most promising candidates for a high-functionality material platform for integrated optics. Germania glass exhibits a lower T_g (~ 790 K) and a lower phonon energy (~ 900 cm⁻¹) than SiO₂ based glasses. GeO₂ glass has attracted particular attention as a potential material for optical fibers with less transmission loss than SiO₂ fibers [1, 2]. Moreover, GeO₂ glasses are transparent in the near infrared region and their refractive index allows fabrication of confined structures. Finally, Germania allows fabrication of highly photorefractive planar waveguides [3] and drawing fiber with smaller absorption losses in the middle IR range as compared to silica glass [4]. However, the tailoring of the synthesis and optimization of a particular phase of GeO₂ crystals is very important as this material exhibits several polymorphs [5]. For these reasons it is of technological and scientific importance to develop a particular fabrication protocol to allow obtaining optical waveguides based on GeO₂ system that exhibit low attenuation coefficients and simultaneously embedded GeO₂ nanocrystals with a particular phase.

Various techniques can be used to fabricate these particular kind of nanostructured systems called glass ceramic in planar format [6] like, as examples, sol-gel technique with top-down and bottom-up approach [7], and physical vapor deposition [8]. Recently, we have also demonstrated that radio frequency magnetron sputtering (RFMS) is a suitable technique to fabricate amorphous optical planar waveguides based on the SiO₂-HfO₂ and SiO₂-GeO₂ binary systems with appropriate optical features for developing the applications at 1.5 μm [9, 10].

In order to produce active rare earth nanocrystals in a glass matrix, heat treatment using a furnace has been commonly used, but a potential candidate for reaching the future technology is the laser annealing (LA) process. For laser annealing several types of lasers have been used, which differs primarily in

wavelength (e.g. XeCl at 308 nm, frequency doubled Nd-YAG at 532 nm, Nd-YAG at 1064 nm and CO₂ at 10.6 μm) [11, 12]. It was reported that CO₂ laser annealing can reduce scattering losses in Corning 7059 glasses [13, 14] and ZnO [15] thin-film waveguides fabricated on thermally oxidized silicon substrates; losses as low as 0.05 dB/cm for Corning 7059 glass waveguide [13] and 0.01 dB/cm for ZnO waveguides [15] have been achieved by this technique.

During the last few decades, the positron annihilation technique has been proven to be one important technique for modifying the properties of materials, and it has developed into a powerful and versatile tool in material preparation [16 - 18]. When an energetic positron enters the medium, it diffuses inside the material and gets thermalized within a few picoseconds. Then the positron either annihilates via a free annihilation process or forms a bound state with an electron, positronium (Ps), and subsequently annihilates. The simplest and most readily used antimatter probe is the positron (the antiparticle to the electron), as its resulting gamma photons carry information about the localization sites of the probe and thus about the electrons of the solid under investigation. When a positron is injected into materials, it will eventually annihilate with an electron with the complete conversion of the pair's combined mass, m , into high-energy photons with total energy E , given by Einstein's famous formula $E = mc^2$.

Recently, positron annihilation spectroscopy (PAS) has been successfully applied to measure the free-volume [19], for surface and interface studies in nanoscale polymeric films [20], free volume in a bulk metallic glass [21], characterization of defects in Si and SiO₂ [18] and also it is a useful technique for modifying the photoluminescent structures of porous silicon [22]. Moreover, with its unique sensitivity to the atomic level free volume in thin films, PAS is emerging as a promising tool to measure depth profiling in thin films through Doppler broadening spectroscopy [23, 24].

In this chapter, we develop a fabrication protocol for GeO₂ planar waveguides and studied the changes in optical and structural properties by combining CO₂ laser and positron irradiation effects.

6.2 Experimental

6.2.1 Planar waveguide fabrication

Pure GeO₂ planar waveguide was prepared by RFMS technique. The wave guiding film was deposited on a silica substrate. In order to improve the adhesion of the films, the substrate was cleaned inside the chamber by heating at 120 °C for 30 min just before the deposition procedure. Sputtering deposition of the film was performed by using a 15x3 cm² Germania target. The residual pressure, before deposition, was about 1.6x10⁻⁶ mbar. During the deposition process, the substrates were not heated. The sputtering was carried out with an Ar gas at a pressure of 5.4x10⁻³ mbar; the applied rf power was 80 W and the reflected power was 0 W. The deposition time, necessary to reach the appropriate thickness for one propagating mode at 1.5 μm was 1 h 58 min.

6.2.2 CO₂ Laser irradiation

As prepared GeO₂ planar waveguides has been used for the irradiation with pulsed CO₂ laser. We have used S50 TEA CO₂ laser which is a mixture of CO₂: N₂: He gas concentrations fixed at 33%:33%:33% percentages. The pulsed laser was used with energy 0.8 J per pulse and having 5 Hz repletion rate and 380 ns pulse width, 10.6 μm wavelength with a beam diameter of 1.5 cm. The experimental set up used for laser irradiation is shown in the Figure 6.1. The laser beam is allowed to incident on the sample directly. Special care was taken to irradiate all over the sample. As the laser beam diameter used for laser annealing is 1.5 cm and it is necessary to avoid the irradiation of the beam on the place where irradiation was made. We have used the iron plate which contains a circular hole with the same diameter of the laser beam. This has been done in order to have a comparison between the irradiated sample and unirradiated

sample. We have used single substrate on which the half part was irradiated and the other half was left as unirradiated. The samples were irradiated in air with 1.3W medium power and the irradiation times were varied from 1 h to 2 h.

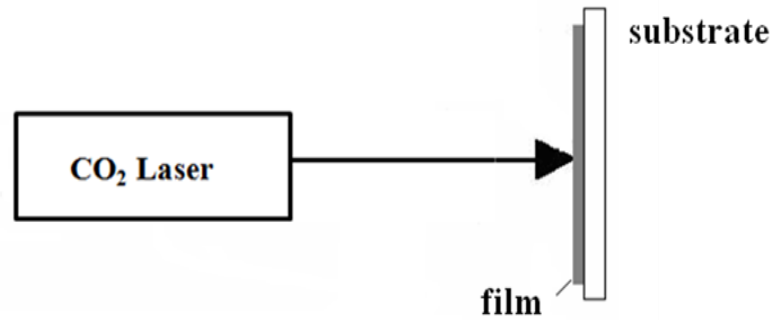


Figure 6.1: Experimental set up for CO₂ laser annealing

6.2.3 Optical and structural properties

The thickness of the waveguide and the refractive index at wavelengths 543.5, 632.8, 1319 and 1542 nm were measured in TE and TM polarizations, by m-line apparatus (Metricon model 2010) based on the prism coupling technique. The losses at 632.8, 1319 and 1542 nm were evaluated by collecting the light intensity scattered out of the waveguide plane for the TE₀ mode using a fiber scanner [25].

Raman scattering measurements were performed at room temperature in a wave number range between 100 and 1000 cm⁻¹ using a microprobe setup (Horiba-Jobin-Yvon, LabRam Aramis) consisting of a He-Ne laser operating at 633 nm and 20 mW power, a narrowband notch filter, a 46 cm focal length spectrograph using a 1800 grooves/mm grating and a charge-coupled device (CCD) as detector. Exciting radiation at 632.8 nm was focused onto the sample surface with a spot size of about 1 μm² through a 100X objective with NA = 0.9. To avoid unwanted laser-induced transformations, neutral filters of different

optical densities were used, whenever necessary. The resolution was about 0.35 cm⁻¹/pixel. The compositional analysis was performed using energy dispersive spectroscopy (EDS), by using a Noran Instruments model Voyager apparatus. Standard AFM technique has been used to measure the surface roughness of the samples before and after laser annealing.

6.2.4 Positron irradiation

Doppler Broadening Spectroscopy – Positron Annihilation Spectroscopy (DBS - PAS) measurements were performed with an electrostatic slow positron beam [17, 26]. The beam was tunable in the 0.05 – 25 keV energy (E) ranges. In GeO₂, these positron implantation energies correspond to a probed film thickness ranging from about 0.1 nm to approximately 2 μ m. The positron beam was coupled to two high purity germanium detectors (HPGe), 45% efficiency, a 1.4 keV resolution at 511 keV, in a 180° configuration. At each positron implantation energy, the 511 keV gamma line was acquired with a micro spectrum method and stabilized by a software procedure [27]

6.3 Results and discussions

6.3.1 Optical properties

The thickness of the waveguide is around 1 μ m and support one TE and TM mode at 1319 and 1542nm. No evident change in the thickness was observed after the laser irradiation. The refractive indices measured in TE and TM polarizations are equal within the experimental uncertainty, so that film birefringence can be considered negligible. Moreover, the laser irradiation does not induce changes between the refractive indices measured in TE and TM polarizations. So, we can affirm that under these condition the CO₂ laser annealing does not induce birefringence in these systems.

Table 6.1: Optical parameters for as prepared sample and after CO₂ laser irradiation for 2h.

Laser wavelength(nm)		Refractive Index		thickness (μm)	Attenuation coefficient(dB/cm)
		TE	TM		
632	Before LA	1.614±0.01	1.616±0.01	1.1±0.1	1.9±0.2
	After LA	1.652±0.01	1.653±0.01	1.1±0.1	1.1±0.2
131	Before LA	1.590±0.01	1.590±0.01	1.0±0.1	1.4±0.2
	After LA	1.631±0.01	1.634±0.01	1.0±0.1	0.7±0.2
154	Before LA	1.585±0.01	1.585±0.01	1.0±0.1	0.9±0.2
	After LA	1.623±0.01	1.624±0.01	1.0±0.1	0.5±0.2

Comparing the refractive indices in the GeO₂ waveguides before and after the CO₂ laser irradiation, we observe an increase of about 0.04 (2.48%) with the irradiation for all the considered wavelengths. Similar results were obtained in other systems treated with CO₂ laser irradiation [28]. Table 6.1 reports the optical parameters for as prepared sample and after CO₂ laser irradiation for 2h. We have observed that laser annealing can lead to waveguides with a lower attenuation coefficient than that obtained for the as prepared sample. In fact, we observe an attenuation coefficient at 1542 nm of 0.5 dB/cm, for the irradiated system while the same parameter for the system before laser annealing is 0.9 dB/cm. The decrease in the attenuation coefficient for the CO₂ laser irradiated systems has been attributed by Dutta et al [14] to the reduction of the surface irregularities. As shown in Table 6.1, these studies show a reduction of the attenuation coefficient with the CO₂ laser irradiation at all the considered wavelengths.

6.3.2 Structural properties

6.3.2.1 EDS and Raman analysis

EDS analysis was used to monitor the composition of the all samples, that as deposited and those submitted to the laser annealing treatments. The

results confirm that the composition of the sample is not affected by the laser irradiation and the correct ratio between germanium and oxygen is always present.

In Figure 6.2, the Micro Raman spectra measured at room temperature for GeO₂ planar waveguide before and after laser irradiation for different times are reported.

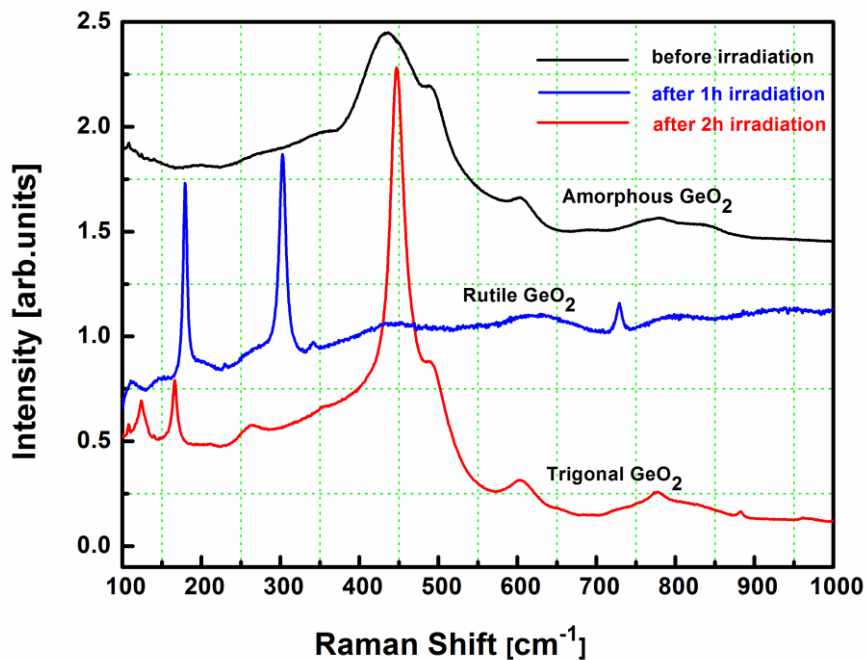


Figure 6.2: Micro Raman measurements carried out at room temperature for GeO₂ planar waveguide before and after CO₂ laser irradiation for different time.

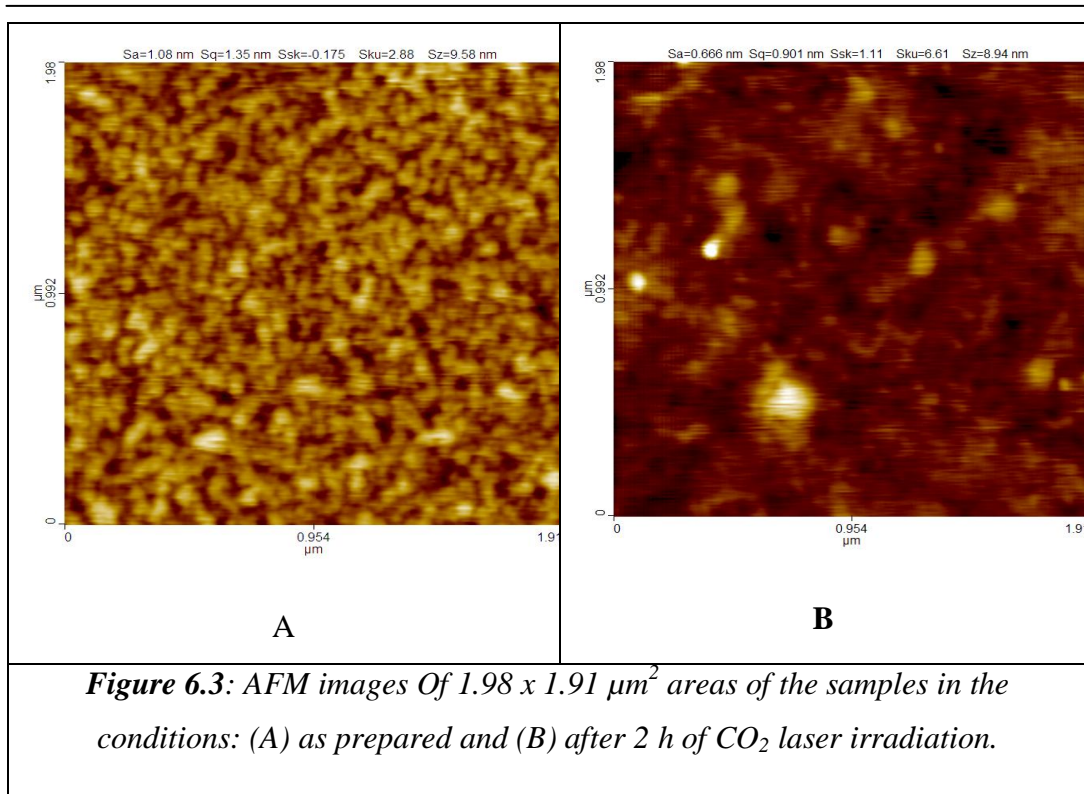
The Raman spectra observed for the as prepared GeO₂ waveguide before irradiation is typical of a GeO₂ amorphous system. In fact, the broad peak at 440 cm⁻¹ clearly indicates the amorphous nature of the GeO₂ film [29]. After 1 h of CO₂ laser irradiation, the Raman spectra indicate the presence of a rutile-like GeO₂ crystalline phase. The peaks observed in the Raman spectra for after 1h CO₂ laser irradiation sample are in good agreement with those reported in the

literature [29]. The peak at 302 cm^{-1} corresponds to Ge optical phonons, related to the Ge–Ge bond [30].

After 2 h of CO_2 laser irradiation, the Raman spectrum obtained from the GeO_2 planar waveguide shows the presence of a trigonal GeO_2 crystal phase. The peaks at 124, 168 and 263 cm^{-1} correspond to the complex translation and rotation of GeO_4 tetrahedra [31]. The peak at 882 cm^{-1} is assigned to Ge-O stretching motion with tetrahedral GeO_4 units [32]. A shift in the band at 444 cm^{-1} is due to symmetric Ge-O-Ge stretching [32]. The peaks observed at 490 and 603 cm^{-1} are D_1 and D_2 defect bands from the Silica substrate. All the bands in the spectrum obtained for the GeO_2 waveguide after 2 h of CO_2 laser irradiation are in good agreement with those of GeO_2 calcinated under a temperature of $T = 1050\text{ }^\circ\text{C}$ [33].

6.3.2.2 AFM analysis

The AFM images of a $1.98 \times 1.91\text{ }\mu\text{m}^2$ area obtained for the as prepared sample (A) and for that submitted to 2h of CO_2 laser irradiation (B) are shown in Figure 6.3. AFM analysis gave the roughness as 1.1 nm in the as prepared sample and a roughness of 0.7 nm for the waveguide after 2h of CO_2 laser irradiation. This result is in agreement with the reduction of the attenuation coefficient with the laser annealing.



Moreover, the AFM image of Figure 6.3 (B) shows the presence on the surface of the sample of structures of nanometer sized particles ranging from 10 to 50 nm. These structures are due to the presence of GeO₂ nanocrystals. It is interesting to note that, although the presence of these scattering points can increase the attenuation coefficient [14], the protocol developed for the CO₂ irradiation allows reducing the total value of the attenuation coefficient.

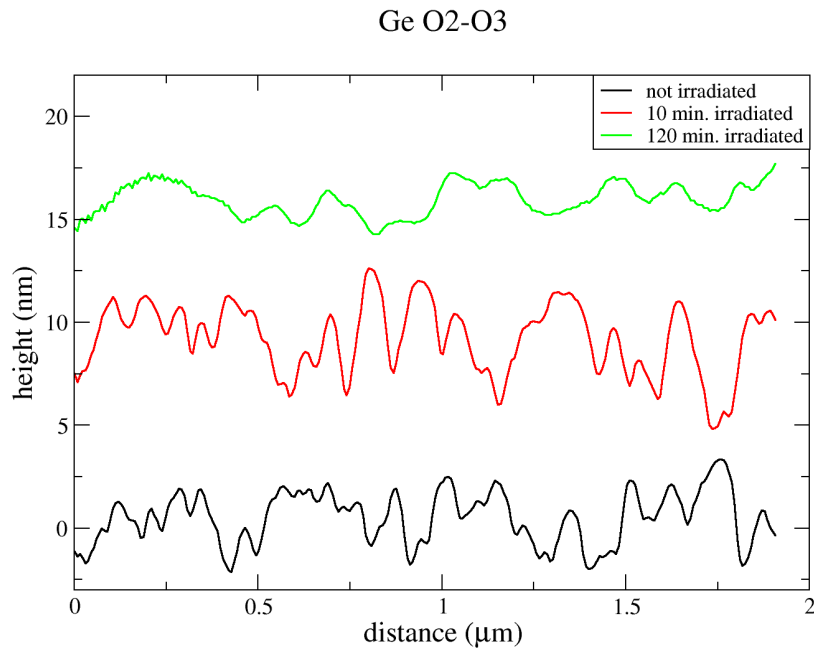


Figure 6.4: Representative profiles of sample Ge O₂.

From the AFM measurement, we have measured the surface roughness values for as prepared, 10 min and 2h irradiated GeO₂ planar waveguides and are shown in the Figure 6.4. It clearly indicates that the surface roughness value decreases as the irradiation time increases which is attributed to the thermal diffusion within the GeO₂ thin film. The surface roughness values shown in table 6.2, which was measured at two different areas. The increase in the surface roughness when measured over large areas is attributed to the presence of the nanoparticle formation. The 10 min irradiated sample still shows the surface roughness almost same as the pristine sample, which we believe that could be mainly due to (1) the AFM scan is from altogether a different area than what is recorded for the pristine sample and (2) the irradiation time is too small to induce major changes in the overall area.

Table 6.2: *Surface roughness values for the sample as prepared and after laser irradiation.*

Irradiation time	Roughness in 1.98x1.91 μm ²	Roughness in 7.68x7.98 μm ²
As prepared	1.1 nm	1.2 nm
10 min	1.3nm	1.2nm
120 min	0.7nm	1.3nm

6.3.3 Effect of positron irradiation

Positrons injected in a solid with energy ranging from a few eV to some keV slow down in few picoseconds (1-3 ps at 300 K) depositing an equivalent thermal energy within the material. Then, after a certain diffusion length, positrons become efficiently trapped in open volume structures and there they annihilate with electrons. The high specific trapping rate of positron for open volumes present in a solid makes this particle a very efficient non-destructive probe for characterizing variations in open volumes or defects from mono vacancies up to voids. The annihilation characteristics are determined by the local electronic environment of the annihilation site (i.e., positron trap) [34].

For mono-energetic positrons, the stopping profile can be well-described by a derivative of a Gaussian function [18, 35]. The mean positron implantation depth $\langle z \rangle$ is related to the positron implantation energy E by the equation:

$$\langle z \rangle = \frac{40}{\rho} E^{1.6} \text{ nm} \quad (1)$$

where E is expressed in keV and the material density ' ρ ' in g/cm³ [18]. When using Doppler Broadening Spectroscopy (DBS), the 511 keV annihilation peak is usually characterized by two line shape parameters S and W . The shape parameter S represents a fraction of positrons annihilating with low-momentum electrons

and is defined as the ratio between the counts in a central area of the annihilation peak, $|511 - E_\gamma| \leq 0.85 \text{ keV}$, and the counts in the total area of the photo peak, $|511 - E_\gamma| \leq 4.25 \text{ keV}$. The wing parameter W represents the fraction of positron annihilating with high-momentum electrons: it is defined as the ratio between the counts in the wing regions of the annihilation peak, $1.6 \text{ keV} \leq |511 - E_\gamma| \leq 4 \text{ keV}$, and the counts in the total area of the photo peak. The narrowing of the 511 keV annihilation line indicates that more positrons are getting annihilated with electrons of low momentum; this behavior is reflected in an increase of the S values and a decrease of the W ones, respectively.

In the present work, from the DBS spectra the S and W parameters were estimated with a statistical error of about 0.1% (more than 2.5×10^5 counts under each annihilation spectrum). Usually, to analyze DBS data, shape line parameters are normalized to that of the substrate bulk (S_b and W_b , respectively); that is $S_n = S/S_b$ and $W_n = W/W_b$. In this work, Silica was used as the substrate material.

In Figure 6.5, the positron depth profiling obtained for the as prepared and for the 2 h CO_2 laser irradiated GeO_2 waveguides samples are shown, specifically, the normalized shape parameter S_n as a function of the positron implantation energy. For the sake of clarity, in the figure only two S curves are shown; i.e., the S_n curve corresponding to 1h CO_2 laser irradiated sample was omitted.

To analyze the positron depth profiling of all the studied GeO_2 waveguides, the experimental data were fitted using a procedure based on the solution of the stationary positron diffusion equation (VEPFIT program [36]). The equation requires an input of the positron implantation profile. Experimental data obtained from the measurements of the as prepared film were well fitted considering two layers plus the silica substrate. On the other hand, in the case of the irradiated samples it was found that the data of both waveguides could be satisfactory fitted using three layers plus the silica substrate. To fit the positron depth profiles it is necessary to have the density of different layers including that

of the substrate (see the relation between depth and density given in equation 1). For silica the density value used was 2.1 g/cm³. However, taking advantage of having precise measurements of the layer thicknesses of each deposited germania films that we have obtained using an m-line apparatus; the S_n versus E curves were analyzed considering the density values of the GeO₂ films of each sample as guess parameters. Under these assumptions, a summary of the main results obtained is presented in table 6.3. Taking into account the density values reported in the table and using equation (1), we transformed energy units, in keV, to nm. So, in the upper abscissa axis of Figure 6.6, the positron mean implantation depth is shown. From fitting, the characteristic values obtained for the silica substrate are $S_b = 0.529 \pm 0.001$ and $W_b = 0.186 \pm 0.001$.

In the as prepared film, positrons detect first a thin superficial layer of about 10 nm which is characterized by a very high S_n value of 1.006. This thin layer is followed by another layer of GeO₂ which we have labelled as layer II. This is characterized by a $S_n = 0.952$ and an uniform structure up to the silica substrate.

With the laser irradiation, the superficial layer reduces to half of its initial thickness and the uniform second layer observed in the as prepared film splits now into two regions, named layers II and III respectively. The first region is structurally similar to the second layer of the non irradiated sample having about the same S_n value (~ 0.95). In the sample irradiated during 1 h, the thickness of the second layer is around 300 nm; and in the case of the sample irradiated for 2 h, the thickness decreases to approximately 170 nm. On the other hand, the second region (i.e., layer III) is characterized by higher S_n value (~ 0.96) than the previous one and it extends up to silica surface.

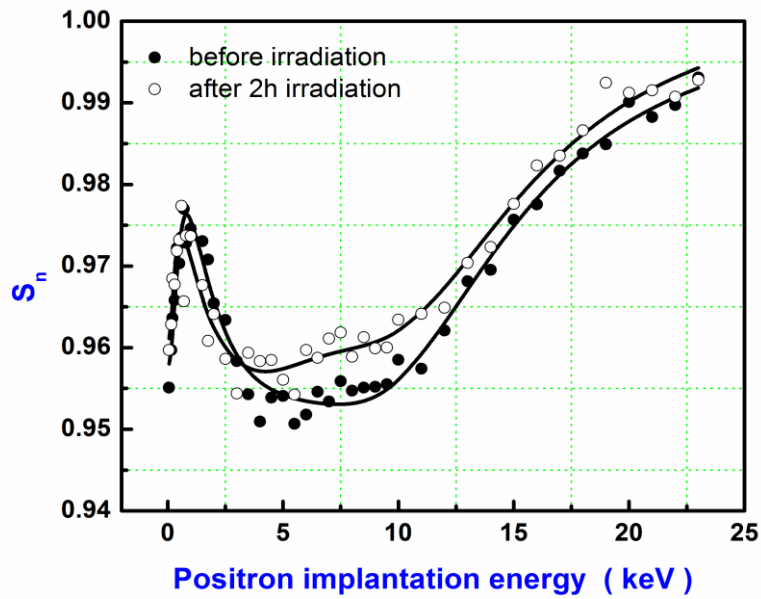


Figure 6.5: Normalized shape parameter S_n as a function of the positron implantation energy for the as prepared and after 2 h CO_2 laser irradiated GeO_2 samples. In the upper scale the mean positron implantation depth is reported. Solid lines represent the best fit obtained using the VEPFIT program (see text). The vertical dash-dotted line points out the interface limit between the film and the silica substrate.

Table 6.3: S_n values characterizing each layer in the as deposited and the two irradiated samples, as obtained using the usual fitting procedure of the positron depth profiles. The density value of the GeO₂ film was used as a guess parameter into the frame of the VEPFIT analysis (see text). The thickness of each layer is taken by taking into account the thickness of the silica interface layer (equal to 983 nm) from the surface.

Sample	Layer I $\rho = 3.15 \text{ g/cm}^3$		Layer II $\rho = 3.15 \text{ g/cm}^3$		Layer III $\rho = 3.15 \text{ g/cm}^3$		Bulk $\rho = 2.1 \text{ g/cm}^3$
	S_n W_n	depth (nm)	S_n W_n	boundary depth (nm)	S_n W_n	boundary depth (nm)	S_n W_n
before irradiation	1.006	11 ± 2	0.952	983 ± 20	-	-	1.000
	1.057		1.104				0.998
after 1h irradiation	1.003	$2 \pm$	0.946	320 ± 25	0.966	983	0.999
	1.052	0.2	1.123		1.076		1.005
after 2h irradiation	0.980	$5 \pm$	0.950	175 ± 32	0.960	983	1.000
	1.043	0.1	1.0999		1.087		0.997

It is worth noting that a simultaneous analysis of S_n and W_n values in a plot $S_n(E)$ vs. $W_n(E)$ provides information about the nature of the positron trapping sites [37]. Specifically, this plot can provide complementary information on the defects and is usually used to verify the change of defect species or the chemical composition surrounding the defects. The different trapping layers are characterized by (S , W) coordinates instead of a single S -value. For example, for the high-energy implantation all positrons annihilate in the silica substrate.

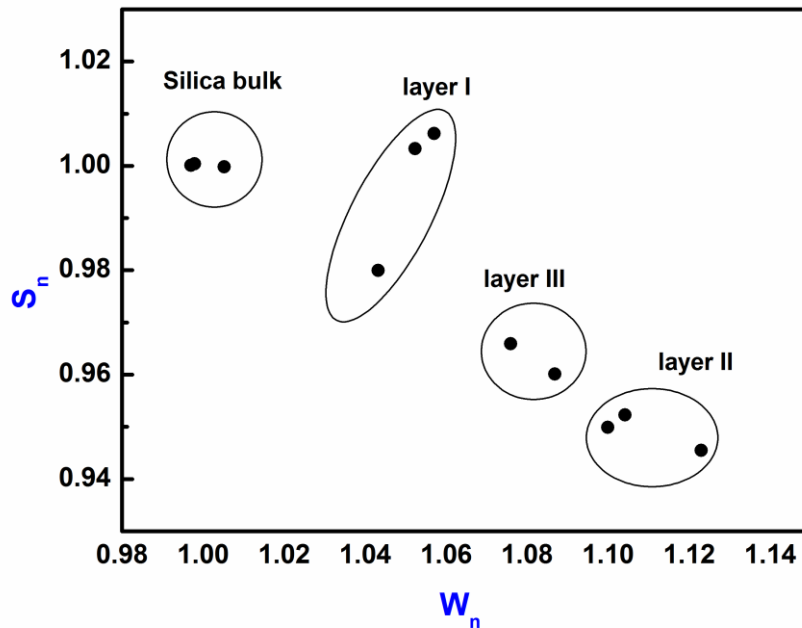


Figure 6.6: S_n - W_n plot for GeO_2 planar waveguide before and after CO_2 laser irradiation for different times (values of both parameters are reported in Table P.1). To obtain this plot, the implantation energy was used as a running parameter.

In the $S_n - W_n$ plane this is seen from the clustering of the experimental data around the point with coordinates $(S_{b-Silica}, W_{b-Silica}) = (1.0, 1.0)$. In Figure 6.7, a S_n - W_n plot for the as prepared and CO_2 laser annealed waveguide samples using the implantation energy as a running parameter is shown. In the figure, different regions were evident from the circles. For all the GeO_2 films, when comparing with the (S_n, W_n) values of the tiny layer I the parameter values corresponding to layers II and III are characterized by the lowest S_n and highest W_n values, respectively. Besides, in the figure it can be seen that the (S_n, W_n) data obtained for the last two layers are positioned along a straight line. This behavior points out that the open volume defects detected in layers II and III are the same type.

The structural changes in the GeO_2 films with the irradiation are illustrated in the scheme plotted in Figure 6.7. For all the samples and the

different layers we have obtained values of the positron diffusion length (L_+) range between 5 nm and 25 nm.

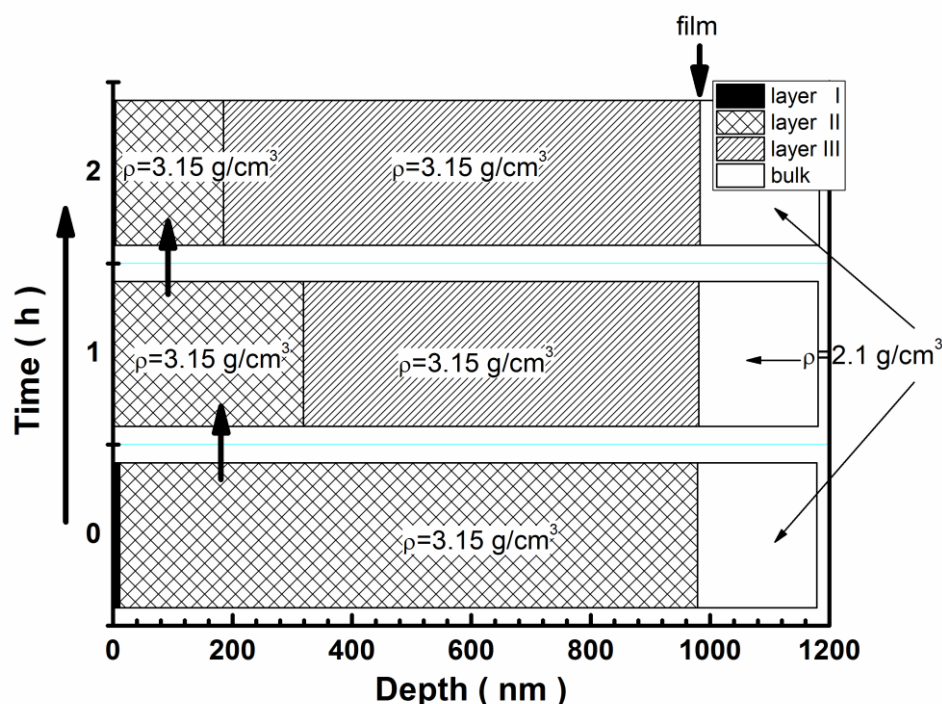


Figure 6.7: Scheme of the nanostructural transformation of the GeO₂ films as a function of the layer thickness and the irradiation time. As shown in this scheme, besides the silica substrate ($\rho = 2.1 \text{ g/cm}^3$) different layers in the GeO₂ films are detected by positron annihilation spectroscopy. From the fitting of the positron data reported in Figure 6.5, a density value of $\rho = 3.15 \text{ g/cm}^3$ for the GeO₂ is obtained.

6.4 Conclusions

GeO₂ planar waveguides were successfully fabricated using RF sputtering technique. The changes in the structural properties on planar waveguides were studied by combining CO₂ laser and positron annihilation spectroscopy technique. After the adopted CO₂ laser annealing, the refractive index of the waveguides increases and the attenuation coefficient decreases. This is interpreted as due to decrease in the surface roughness by thermal diffusion. Raman and AFM results give an evidence for the formation of nanocrystals

inside GeO₂ matrix after laser irradiation. PAS technique was used to measure the depth profile of the laser irradiated samples.

6.5 References

1. R. Olshansky and G. W. Scherer, "High GeO₂ optical waveguides," in Tech. Dig. 5th European Conference on Optical Communications (The Netherland), (1979).
2. T. Miyashita and T. Manabe, "Infrared optical fibers," *IEEE J. Quantum Electron.* **QE-18**, 1432–1450 (1982).
3. S. Sebastiani, G. Nunzi Conti, S. Pelli, G. C. Righini, A. Chiasera, M. Ferrari and C. Tosello, "Characterization of a highly photorefractive RF-sputtered SiO₂-GeO₂ waveguide," *Opt. Exp.* **13**, 1696 (2005).
4. V. P. Prakapenk, G. Shen, L. S. Dubrovinsky, M. L. Rivers and S. R. Sutton, "High pressure induced phase transformation of SiO₂ and GeO₂: difference and similarity," *J. Phys. Chem. Solids* **65**, 1537 (2004).
5. A. V. Anan'ev, V. N. Bogdanov, B. Champagnon, M. Ferrari, G. O. Karapetyan, L. V. Maksimov, S. V. Smerdin and V. A. Solovyev, "Origin of Rayleigh scattering and anomaly of elastic properties in vitreous and molten GeO₂," *J. Non-Cryst. Solids* **354**, 3049 (2008).
6. A. Chiasera, G. Alombert-Goget, M. Ferrari, S. Berneschi, S. Pelli, B. Boulard, C. Duverger Arfuso, "Rare earth-activated glass-ceramic in planar format," *Opt. Eng.* **50**, 071105-1 - 071105-10 (2011).
7. S. Berneschi, S. Soria, G. C. Righini, G. Alombert-Goget, A. Chiappini, A. Chiasera, Y. Jestin, M. Ferrari, S. Guddala, E. Moser, S. N. B. Bhaktha, B. Boulard, C. Duverger Arfuso and S. Turrell, "Rare-earth-activated glass-ceramic waveguides," *Opt. Mat.* **32**, 1644-1647, (2010).
8. B. Boulard, G. Alombert, I. Savelii, C. Duverger-Arfuso, Y. Gao, M. Ferrari and F. Prudeniano, "Er³⁺/Yb³⁺/Ce³⁺ co-doped fluoride glass ceramics waveguides for application in the 1.5 μm telecommunication window," *Advances in Science and Technology* **71**, 16-21 (2010).

9. A. Chiasera, C. Armellini, S. N. B. Bhaktha, A. Chiappini, Y. Jestin, M. Ferrari, E. Moser, A. Coppa, V. Foglietti, P. T. Huy, K. Tran Ngoc, G. Nunzi Conti, S. Pelli, G. C. Righini and G. Speranza, “Er³⁺/Yb³⁺-activated silica-hafnia planar waveguides for photonics fabricated by rf-sputtering,” *J. Non-Cryst. Solids* **355**, 1176–1179 (2009).
10. G. Nunzi Conti, S. Berneschi, M. Brenci, S. Pelli, S. Sebastiani, G. C. Righini, C. Tosello, A. Chiasera and M. Ferrari, “UV photoimprinting of channel waveguides on active SiO₂–GeO₂ sputtered thin films,” *Appl. Phy. Lett.* **89**, 121102-1 – 121101-3 (2006).
11. S. Dutta, H. E. Jackson, J. T. Boyd, R. L. Davis and F. S. Hickernell, “CO₂ laser annealing of Si₃N₄, Nb₂O₅ and Ta₂O₅ thin film optical waveguides to achieve scattering loss reduction,” *IEEE J. Quantum Electron. QE-18* (4), 800–806 (1982).
12. M. Zevin and R. Reisfeld, “Preparation and properties of active waveguides based on zirconia glasses,” *Opt. Mater.* **8**, 37 (1997).
13. S. Dutta, H. E. Jackson and J. T. Boyd, “Reduction of scattering from a glass thin-film optical waveguide by CO₂ laser annealing,” *Appl. Phy. Lett.* **37** (6), 512–514 (1980).
14. S. Dutta, H. E. Jackson and J. T. Boyd, “Extremely low-loss glass thin-film optical waveguides utilizing surface coating and laser annealing,” *J. Appl. Phys.* **52** (6), 3873–3875 (1981).
15. S. Dutta, H. E. Jackson, J. T. Boyd, F. S. Hickernell and R. L. Davis, “Scattering loss reduction in ZnO optical waveguides by laser annealing,” *Appl. Phy. Lett.* **39** (3), 206–208 (1981).
16. Y. C. JEAN, “Positron Annihilation Spectroscopy for Chemical Analysis: A Novel Probe for Micro structural Analysis of Polymers,” *Microchem. J* **42**, 72-102 (1990).
17. A. Zecca, M. Bettonte, J. Paridaens, G. P. Karwasz and R. S. Brusa, “A new electrostatic positron beam for surface studies,” *Meas. Sci. Technol.* **9**, 409 (1998).

18. P. Asoka-Kumar, K. G. Lynn and D. O. Welch, "Characterization of defects in Si and SiO₂-Si using positrons," *J. Appl. Phys.* **76**, 4935 (1994).
19. J. D. Ferry, "*Viscoelastic Properties of Polymers*" Third ed., Wiley, New York (1980).
20. Y. C. Jean, J. Zhang, H. Chen, Y. Li and G. Liu, "Positron annihilation spectroscopy for surface and interface studies in nanoscale polymeric films," *Spectrochimica Acta Part A* **61**, 1683–1691 ((2005).
21. K. M. Flores, D. Suh, R. H. Dauskardt, P. Asoka-Kumar, P.A. Sterne and R.H. Howell, "Characterization of free volume in a bulk metallic glass using positron annihilation spectroscopy," *J. Mater. Res.* **17(5)**, 1153 (2002).
22. Y. M. Huang, "Positron irradiation: A technique for modifying the photoluminescent structures of porous silicon," *Appl. Phys. Lett.* **71(26)**, 3850 (1997).
23. Robert I. Grynszpan, W. Anwand, G. Brauer and Paul G. Coleman, "Positron depth profiling in solid surface layers," *Ann. Chim. Sci. Mat.* **32(4)**, 365-382 (2007).
24. W. H. Eijt, R. Kind, S. Singh, H. Schut, W. J. Legerstee, R. W. A. Hendrikx, V. L. Svetchnikov, R. J. Westerwaal and B. Dam, "Positron depth profiling of the structural and electronic structure transformations of hydrogenated Mg-based thin films," *J. Appl. Phys.* **105**, 043514 (2009).
25. S. J. L. Ribeiro, Y. Messaddeq, R. R. Gonçalves, M. Ferrari, M. Montagna, M. A. Aegerter, "Low optical loss planar waveguides prepared by an organic-inorganic hybrid system," *Appl. Phys. Lett.* **77**, 3502 (2000).
26. C. Macchi, S. Mariazzi, G. P. Karwasz, R. S. Brusa, P. Folegati, S. Frabboni and G. Ottaviani, "Single-crystal silicon co-implanted by helium and hydrogen: Evolution of decorated vacancy like defects with thermal treatments," *Phys. Rev. B* **74**, 174120 (2006).
27. R. S. Brusa, G. P. Karwasz, N. Tiengo, A. Zecca, F. Corni, R. Tonini, and G. Ottaviani, "Formation of vacancy clusters and cavities in He-

- implanted silicon studied by slow-positron annihilation spectroscopy,” *Phys. Rev. B* **61**, 10154 (2000).
28. C. Goyes, M. Ferrari, C. Armellini, A. Chiasera, Y. Jestin, G. C. Righini, F. Fonthal and E. Solarte, “CO₂ laser annealing on erbium-activated glass–ceramic waveguides for photonics,” *Opt. Mater.* **31**, 1310–1314 (2009).
29. A. Trukhin and B. Capoen, “Raman and optical reflection spectra of germanate and silicate glasses,” *J. Non-Crys. Solids* **351**, 3640–3643 (2005).
30. Y. M. Yang, L. W. Yang and P. K. Chu, “Polarized Raman scattering of Ge nanocrystals embedded in *a*-SiO₂,” *Appl. Phys. Lett.* **90**, 081909 (2007).
31. T. P. Mernagh and L. -g. Liu, “Temperature dependence of Raman spectra of the quartz-and rutile-types of GeO₂,” *Phys. Chem. Miner.* **24**, 7–16 (1997).
32. Victor V. Atuchin, T. A. Gavrilova, S. A. Gromilov, V. G. Kostrovsky, L. D. Pokrovsky, I. B. Troitskaia, R. S. Vemuri, G. Carbajal-Franco and C.V. Ramana, “Low-Temperature Chemical Synthesis and Microstructure Analysis of GeO₂ Crystals with α -Quartz Structure,” *J. Cryst. Growth* **9** (4), 1829-1832 (2009).
33. M. Madon, Ph. Gillet, Ch. Julien and G. D. Price, “A vibrational study of phase transitions among the GeO₂ polymorph,” *Phys. Chem. Miner.* **18**, 7 (1991).
34. P. Schultz and K. G. Lynn, “Interaction of positron beams with surfaces, thin films, and interfaces,” *Rev. Mod. Phys.* **60**, 701 (1988).
35. S. Valkealahti and R. M. Nieminen “Monte Carlo calculations of keV electron and positron slowing down in solids. II,” *Appl. Phys. A* **35**, 51 (1984).

36. A. van Veen, H. Schut, J. de Vries, R. A. Hakvoort and M. R. Ijpma. “Analysis of positron profiling data by means of ‘VEPFIT’,” *AIP Conf Proc.* **218**, 171 (1990).
37. M. Clement, J. M. M de Nijs, P. Balk, H. Shut, A. J. van Veen, “Analysis of positron beam data by the combined use of the shape- and wing-parameters,” *J. Appl. Phys.* **79**, 9029 (1999).

Chapter 7

Conclusions and future perspectives

7.1 Conclusions

It has been of major interest in recent research to produce faster optical processing for many telecommunications applications and other applications such as optical limiting devices. Most applications of photonic crystals are based on how to introduce the defects in the photonic crystals engineering, one can control, trap, or change the wave propagation.

This thesis is focused on fabrication and their characterization of one dimensional photonic crystals with the defect layer for the telecommunication and nonlinear optical device applications. Also as a primary test, we have fabricated pure GeO_2 planar waveguides and consequently CO_2 laser and positron irradiation effect on optical and structural properties. Further it can be extended to the system Erbium doped GeO_2 planar waveguides for 1.5 μm telecommunication applications. In the variety of technologies employed for the fabrication of one dimensional photonic crystals and planar waveguides, we have used radio frequency magnetron sputtering technique and as active films SiO_2 and TiO_2 for photonic crystals and GeO_2 for planar waveguides were chosen.

In conclusion, we present the fabrication protocol for one dimensional photonic crystals using rf sputtering technique. Thin films of SiO_2 and TiO_2 were used to fabricate photonic crystals with defect (microcavity) and without defect (Bragg mirror) layer and the stop band contains in the visible and near infrared regions. The position, width, depth, and shape of the stop band strongly depend on the periodicity, symmetry properties, refractive index contrast, and internal lattice structure of the unit cell. These effects were studied by observing the transmission and reflection measurements. One of the important properties of photonic crystals is angle resolved reflection measurements. As the incident angle increases the stop band move towards the lower wavelength regions. Variable angle reflection geometry was used to study the angle resolved spectral characteristics for Bragg mirror and also for microcavity.

The Fabry-Perot fringes on either side of the stop band can be observed in both transmission and reflection spectra as explained in the chapter 3 and these oscillations are due to the interference of light reflected from the front and back surface of the each interface of the dielectric layer. These fringes indicate the homogeneity of the thickness and effective refractive index of the photonic crystal within the illuminated area. The total thickness of the photonic crystal was calculated using these Fabry-Perot fringes. Transfer matrix method was explained to calculate the transmission and reflection properties of Bragg mirror and some of the results were compared with experimental results.

Another important property of photonic crystals is the polarization dependence. In the case of TE polarization, the stop band width increases as the incident angle increases where as in case of TM polarization, it reduces. Similarly, the microcavity affects the polarization of light on at the stop band and the height of cavity resonance decreases in case of TE polarization, where as in case of TM polarization, gradually increases.

Erbium-doped materials are of great interest in optoelectronics due to the Er^{3+} emission at 1.535 μm , a standard telecommunications wavelength. With this aim, the Bragg reflector consists of twenty $\text{SiO}_2/\text{TiO}_2$ bilayers, designed with a stop band in the near infrared region. The cavity is constituted of an Er^{3+} doped SiO_2 active layer inserted between two such Bragg reflectors. Scanning electron microscopy was used to measure directly the thickness of the layers and put in evidence the homogeneities of the layers and their good adhesion. NIR transmittance and variable angle reflectance spectra confirm that the presence of a stop band from 1500 nm to 2000 nm with a cavity resonance centered at 1749 nm at 0° , a FWHM 1.97 nm, corresponding to a quality factor (Q) of about 890. The effect of the cavity on the ${}^4\text{I}_{13/2} \rightarrow {}^4\text{I}_{15/2}$ emission band is demonstrated by the narrowing of the emission band as well as by the enhancement of the Er^{3+} PL intensity. The latter effect is verified by the observation that the peak luminescence intensity from the photonic crystal is 56 times higher than that of the reference sample under the same excitation condition. In conclusion, three

important outcomes characterize this work: 1) fabrication protocol leading to a specific control of compositional, optical and geometrical parameters allowing high Q factor and luminescence enhancement; 2) extent of the stop band and the resonance to longer wavelengths leading to potential new functionalities; 3) the reference sample fabrication and the employed geometry allowed a reliable assessment of the influence of the cavity and we believe that this method can be largely employed so that the errors on luminescence enhancement measurement due to the different configurations may be drastically reduced.

Another important application of photonic crystals is the localization of light. We have prepared one dimensional photonic crystal with ZnO defect layer. We have observed that photonic crystal containing ZnO defect layer exhibits large enhancement in the nonlinear absorption when compared with that of ZnO reference sample. Enhancement in the nonlinear absorption can be attributed to the strong confinement of the optical field around the defect layer. Bragg mirror consists 21 layers of SiO₂, TiO₂ dielectric films. The cavity is constituted of nonlinear ZnO defect layer inserted between two such Bragg reflectors. SEM analysis shows surface morphology of multilayer films. Transmission spectra reveal that there is a broad stop band from 430 nm to 560 nm. Variable angle reflection spectra show that the defect resonance appears at 532 nm at 30⁰ incident angle. Angle dependant Z-scan technique was used to measure nonlinear optical properties of photonic crystals and ZnO reference sample. Open aperture Z-scan measurements shows that the Z-scan curve of the detuned resonant photonic crystal exhibited a larger transmittance dip as compared to a single layer of ZnO reference. Nearly 21 times increase in the nonlinear absorption was observed for the photonic crystal structure when compared to a single layer of the ZnO reference. We have observed good optical limiting behaviour in photonic crystal which is due to the large enhancement of nonlinear absorption in the photonic crystal structure.

Pure GeO₂ planar waveguides were fabricated using rf sputtering technique. Combining CO₂ laser and positron irradiation effects, optical and

structural properties of planar waveguides were studied. The effects of pulsed CO₂ laser irradiation on the optical and structural properties of the waveguides are evaluated by different techniques as m-line and micro-Raman spectroscopy and atomic force microscopy (AFM). After pulsed CO₂ laser annealing, an increase of the refractive index of approximately 0.04 at 1.5 μm and a decrease of the attenuation coefficient from 0.9 to 0.5 dB/cm at 1.5 μm was observed. Raman spectroscopy and AFM results put in evidence that after an adapted pulsed CO₂ laser annealing, the system showed a crystalline environment in which the phase of the crystalline GeO₂ varies with varying irradiation time. Moreover, positron annihilation spectroscopy was used to study the depth of the defect profile for the as prepared and laser annealed samples. The results obtained allowed getting information on the structural changes produced inside the waveguides films of approximately 1 μm thickness after the irradiation process. In addition, a density value for the amorphous GeO₂ samples was also obtained.

7.2 Future perspectives

Work is under way to improve the fabrication of GeO₂ planar waveguides doped with rare earth ions for telecommunication applications. As discussed above, CO₂ irradiation affects optical and structural properties of pure GeO₂ planar waveguides. In this way it is possible to produce GeO₂ nanocrystals.

The drive toward advanced photovoltaic (PV) devices that overcome single junction efficiency limits necessitates the mitigation of losses incurred by the transmission of sub bandgap photons in conventional solar cells [1]. Er - doped up conversion (UC) phosphors such as NaYF₄ show a remarkable ability to sequentially absorb multiple long-wavelength (e.g., 1550 nm) photons to which a Si solar cell is transparent and emit above the Si band edge (with peaks at 980 nm, 810 nm, 660 nm, 550 nm etc.) [2]. But their performance is limited by narrow absorption line widths and small absorption cross sections; the efficiency of UC saturates such that only a negligible net power conversion efficiency gain has been reported for a coupled UC–PV system [3].

Electromagnetic (EM) waves travelling in dispersive media are subject to deviation between their phase velocity V_p and group velocity V_g . Slow light modes are possible in photonic crystals (PCs), in which spatial periodicity of the refractive index induces high dispersion. In a distributed Bragg reflector (DBR) the prototypical 1D photonic crystal regular variation of the optical thickness of multiple alternating layers results in wavelength dependent interference behavior manifesting as discrete bands of allowed and disallowed EM modes.

Using SiO_2 and TiO_2 thin films, one dimensional photonic crystals will be fabricated. Each layer is doped with Er^{3+} and design the Bragg mirror in such a way that the band edge should fall exactly at the position of the Erbium emission. In principle, an Er-doped DBR with a band edge positioned near the 1550nm (${}^4\text{I}_{15/2} \rightarrow {}^4\text{I}_{13/2}$) first excited state transition of Er would demonstrate slow light enhancement effects on the intensity of light emitted as a result of UC in Er.

7.3 References

1. G. Conibeer, "Third generation photovoltaics," *Mater. Today* **10**, 42 (2007).
2. H. Q. Wang, M. Batentschuk, A. Osvet, L. Pinna and C. J. Brabec, "Rare-earth ion doped up-conversion materials for photovoltaic applications," *Adv. Mater.* **23**, 2675 (2011).
3. A. Shalav, B. S. Richards and M. A. Green, "Luminescent layers for enhanced silicon solar cell performance: Up-conversion," *Sol. Energy Mater. Sol. Cells* **91**, 829 (2007).

Valligatla Sreeramulu - Curriculum Vitae

Contact: V. Sreeramulu,
Laser lab,
School of Physics,
University of Hyderabad,
Gachibowli, Hyderabad,
Andhra Pradesh,
INDIA - 500 046
Phone: +91-9492756662
Email: srihcu08@gmail.com

Research Interests

My research interest lies in the field of Photonic crystals. Mainly on one - dimensional photonic crystals fabrication and their characterizations towards the applications of communications, optical limiters and devices. I am also interested in the planar waveguides towards optical communication applications.

Educational Qualifications

Doctor of Philosophy (Ph. D)

School of Physics,

University of Hyderabad, Andhra Pradesh, INDIA.

Thesis title: “One Dimensional Photonic crystals and Planar Waveguides: Fabrication by RF Sputtering and their Characterization”.

Research Adviser: Prof. D. Narayana Rao.

M.Sc Physics (April 2008)

Banaras Hindu University,

Varanasi, India.

Percentage: 73.9%

Specialization: Condensed matter physics

B. Sc., Computer Science (March 2005)

S. V. Arts College, Tirupathi, India.

Percentage: 78.9%

Other subjects: Physics and Mathematics.

Publications

Related to thesis

1. **S. Valligatla**, A. Chiasera, S. Varas, N. Bazzanella, D. Narayana Rao, G.C. Righini and M. Ferrari, “High quality factor 1-D Er^{3+} - activated dielectric microcavity fabricated by rf sputtering,” *Optics Express* **20** (19), 21214 – 21222, (2012).
2. **S. Valligatla**, A. Chiasera, K. S. Alee, S. Varas, D. Narayana Rao, M. Ferrari, G. C. Righini, “Local field enhancement on nonlinear absorption in one dimensional photonic crystals fabricated with ZnO defect fabricated by rf sputtering” [to be communicated to **Optics Express**].
3. A. Chiasera, **S. Valligatla**, S. Varas, N. Bazzanella, D. Narayana Rao, G. C. Righini, M. Ferrari, “High quality factor multilayer structures fabricated by rf sputtering”, Proc. of SPIE Vol. **8431**, 843127-1 (2012).
4. **S. Valligatla**, A. Chiasera, M. B. M. Krishna, S. Varas, D. Narayana Rao, M. Ferrari, G. C. Righini, “Nonlinear enhancement in one dimensional photonic crystals with ZnO defect fabricated by rf sputtering” [Manuscript is under preparation].

-
5. A. Chiasera, **S. Valligatla**, S. Varas, D. Narayana Rao, M. Ferrari, G. C. Righini, "CO₂ laser and positron irradiation effects on pure GeO₂ planar waveguides fabricated by rf sputtering" [Manuscript is under preparation].
 6. **S. Valligatla**, A. Chiasera, S. Varas, D. Narayana Rao, M. Ferrari, G. C. Righini, "Enhanced spontaneous emission at the band edge of one dimensional photonic crystals" [Manuscript is under preparation].

Not included in thesis

1. T. Jadhav, R. Maragani, R. Misra, **V. Sreeramulu**, D. Narayana Rao, S. M. Mobin, "Design and synthesis of donor-acceptor pyrazabole derivatives for multiphoton absorption", *Dalton Transactions* **42**, 4340-4342 (2013).
2. H. Krishna, J. Anupama, **S. Valligatla**, P. Narayan, D. Suwarna, D. N. Rao, P. Amitava, "Synthesis, Electronic and Nonlinear Properties of Metal-Semiconductor Hybrid Tetrapod Heterostructures" [to be communicated].
3. **S. Valligatla**, A. Chiasera, S. Varas, D. Narayana Rao, M. Ferrari, G. C. Righini, "Enhanced spontaneous emission at the band edge of one dimensional photonic crystals" [Manuscript is under preparation].
4. S. Berneschi, M. Brenci, G. C. Righini, M. Bettinelli, A. Speghini, U.s Caldiño, E. Álvarez, A. Chiasera, **S. Valligatla**, M. Ferrari "Soda-zinc-aluminosilicate glasses doped with Tb³⁺, Ce³⁺ and Sm³⁺ for frequency conversion and white light generation" 22nd Congress of the International Commission for Optics: Light for the Development of the World, Proc. of SPIE Vol. **8011** 801159-1 (2011).

Career Achievements

- i. Qualified National Eligibility Test – 2009 for Junior research Fellowship and Lectureship conducted by Council of Scientific and Industrial Research and University Grants Commission (CSIR & UGC), Indian Government.
- ii. Qualified in Joint Entrance Screening Test (JEST is a common qualifying test for admissions to Ph.D. programmes in Physics at premier Indian research institutions) in February 2008 and got All India Rank 381.

-
- iii. Qualified in Graduate Aptitude Test in Engineering (GATE is an all India examination administered and conducted jointly by the Indian Institute of Science and seven Indian Institutes of Technology on behalf of the National Coordination Board - GATE, Department of Higher Education, Ministry of Human Resource Development (MHRD), Government of India.) in February 2009 and got All India Rank 628 in Physics.